NASA CONTRACTOR REPORT

CONCEPTS OF MULTIPLE-IMPACT STUDY OF ENERGY ABSORPTION

NASA CR-273

CONCEPTS OF MULTIPLE-IMPACT STUDY

OF ENERGY ABSORPTION

Distribution of this report is provided in the interest of information exchange. Responsibility for the contents resides in the author or organization that prepared it.

TABLE OF CONTENTS

TABLE OF CONTENTS (Cont'd)

LIST OF FIGURES AND TABLES

LIST OF FIGURES AND TABLES   (Cont'd)

LIST OF FIGURES AND TABLES (Cont'd)

LIST OF FIGURES AND TABLES   (Cont'd)

NOMENCLATURE

a	acceleration; radius of torus element
A	cross-sectional area
b	contact area for elastic cylinder compressed between rigid plates
c	heat capacity
C	fatigue constant (Equation (35))
d	diameter of torus wire element
Δd	diametral compression of cylindrical element
D	flexural rigidity
D'	effective flexural rigidity defined by Equation (75)
D_i'	effective flexural rigidity at end of i-th cantilever element
E	elastic modulus
Ei	exponential integral (Equation (33))
E*	complex modulus
E_1	storage modulus (real part of E*)
E_2	loss modulus (imaginary part of E*)
f	driving force per unit length of tube
f_c	compressive force per unit length of tube
F	force
F_o	initial force
G	elastic shear modulus
G_A	spring constant of the apparatus
G*	complex shear modulus
G_1	storage modulus (real part of G*)

G_2 loss modulus (imaginary part of G^*)

G' elastic shear modulus of specimen and apparatus

$G^{*'}$ complex modulus of specimen and apparatus

G_1' storage modulus of specimen and apparatus

G_2' loss modulus of specimen and apparatus

h   tube wall thickness

K   material constant

ℓ width of boundary of cylindrical element over which uniform load acts

ℓ_i length of i-th cantilever element

L   length of transmitter; total stroke length

M, M_A, M_B bending moments per unit length of tube (Figure 17)

M_i bending moment at end of i-th cantilever element

M_{PL} bending moment at proportional limit

M_w mass of working material

n   rate sensitivity; exponent in plastic stress-strain relation

n_I number of cycles per impact

N   number of cycles to failure

N_I number of impacts

p   hydrostatic pressure

P   total lateral compressive load per unit length of cylindrical element

q   uniform load distribution

r radial coordinate for cross-section of torus element; tube radius

R   average major radius of torus element

NOMENCLATURE (Cont'd)

s	arc length
SEA	specific energy absorption or energy absorbed per unit weight
SEA_c	SEA of cycling mechanism
SEA_t	SEA of load transmitter
SEA_w	SEA of working metal
SEA_o	SEA_w corresponding to failure in one cycle
SEA_{max}	maximum SEA
t	time
T	absolute temperature
T_o	initial absolute temperature
v	velocity
v_o	initial velocity
V	volume
V_w	volume of working material
w_p	area under hysteresis loop or energy absorbed per unit volume per cycle
w_{p_o}	initial value of w_p
W_p	total energy absorbed per cycle
x	stroke coordinate
y	distance from neutral axis
α	exponent of Equation (35); angle defined in Figure 16
α_o	value of α defined by particular circle (See Equation (65) and Figure 16)
α_i	parameter defined by Equation (84)
β	loss factor (E_2/E_1); parameter defined in Figure (65)

β_i parameter defined by Equation (84)

γ shear strain; parameter defined in Equation (65)

δ_i deflection for i-th cantilever element

δ_i' change in slope for i-th cantilever element

$\Delta\gamma_p$ plastic shear strain range

$\Delta\gamma_T$ total shear strain range

γ_{max} shear strain amplitude

γ_{max}' shear strain amplitude of specimen and apparatus

δ parameter defined in Equation (65)

ϵ strain

ϵ_o strain amplitude

ϵ_m maximum strain (Figure 19)

ϵ_f fracture strain

ϵ_p plastic strain

ϵ_{pm} maximum plastic strain (Figure 19)

ϵ_{PL} "plastic" strain at proportional limit in approximate stress-strain relation

$\dot{\epsilon}_p$ plastic strain rate

$\epsilon_{P1}, \epsilon_{P2}$ reference values of plastic strain rate

$\Delta\epsilon_E$ elastic strain range

$\Delta\epsilon_p$ plastic strain range

$\Delta\epsilon_T$ total strain range

η ratio of average stress range to maximum stress range; radial deflection of tube; dashpot constant

η_i contribution to η from i-th cantilever element

θ phase angle; angular coordinate

$\Delta\theta$ change in slope

θ' phase angle for specimen and apparatus

θ_o phase angle

λ nondimensional length, ℓ/a; parameter defined by Equation (85)

ν number of cycles; Poisson's ratio

ρ nondimensional radial coordinate, h/a

ρ_t density of load transmitter material

ρ_w density of working metal

σ stress

$\sigma_{c_{max}}$ maximum compressive stress

σ_o initial stress; stress amplitude

σ_m maximum stress (Figure 19)

σ_{PL} proportional limit stress

σ_1, σ_2 reference values of stress

σ_I, σ_{II} principal stresses defined in Equation (57) and Figure 16

σ_{i_o}' i-th principal deviator stress component amplitude

$\sigma_{1_o}', \sigma_{2_o}', \sigma_{3_o}'$ principal deviator stress component amplitudes

$\sigma_r, \sigma_\theta, \sigma_z$ stress components in cylindrical coordinates

$\sigma_r^v, \sigma_\theta^v$ values of σ_r, σ_θ evaluated along vertical radius (Figure 16)

$\sigma_r^h, \sigma_\theta^h$ values of σ_r, σ_θ evaluated along horizontal radius (Figure 16)

NOMENCLATURE (Dont'd)

$\sigma'_r , \sigma'_\theta , \sigma'_z$ deviator stress components in cylindrical coordinates

$\sigma'_{r_o} , \sigma'_{\theta_o} , \sigma'_{z_o}$ principal deviator stress component amplitudes in cylindrical coordinates

σ_{ult} ultimate strength

σ_y yield strength

$\Delta\sigma_{max}$ maximum stress range

$\Delta\sigma_{max_o}$ initial value of $\Delta\sigma_{max}$

$\overline{\Delta\sigma}$ average stress range

τ shear stress

τ_o shear stress amplitude

τ_{max} shear stress amplitude

φ angular coordinate

ω frequency (radians/sec.)

ω_o initial frequency

I SUMMARY

An attractive new concept of energy absorbing devices incorporating cyclic straining of materials is described. Devices of this type are of particular interest for space applications such as landing impact, and offer multiple-impact capability as well as energy absorption efficiencies greatly exceeding values attainable with other existing devices.

Results of an 18-month research program to investigate this concept are presented. Basic principles are discussed and analytical methods for predicting the characteristics and behavior of cyclic strain energy devices are developed. Flow and fatigue behavior of materials is summarized in relation to performance and design. A cyclic torsion apparatus for studying materials under cyclic straining is described and data for several promising materials is presented. The design, construction, and testing of two promising cyclic strain energy impact devices are described. The test results demonstrate the feasibility and potential of this concept.

II INTRODUCTION

Current interest in high-energy-absorbing mechanisms has been stimulated by the growing need for such systems and the associated problems in effectively dissipating the landing impact energy of descending space vehicles. Considerable research has been conducted on methods and devices for landing impact. Most of these studies, with the exception of those concerned with retrorockets, have dealt with devices which absorb energy by totally or partially destroying themselves upon impact. These devices include (1) fragmenting tubes, (2) crushable materials, (3) deformable structures, and (4) gas bags

1

and gas-filled collapsible shells. At the other end of the spectrum are systems having lower energy-absorption potentials but essentially unlimited life, such as conventional hydraulic-mechanical devices.

An extremely attractive concept for high-energy absorption devices incorporating cyclic straining of materials was disclosed recently by ARA, Inc. (References 1 and 2). It was shown that for multiple impact applications, cyclic strain energy devices offer energy absorption efficiencies greatly exceeding those available from the other high-energy devices mentioned above.

A parameter commonly used for comparing high-energy absorption mechanisms is SEA or specific energy absorption (ft-lb/lb). Balsa wood, for example, has an SEA capability of 24,000 ft-lb/lb compared with typical values of 12,000 ft-lb/lb for crushing of metal honeycomb (Reference 3). One of the most efficient devices described in the literature is the frangible tube device which employs the fragmentation of a thin-walled metal tube over a metal die. This device is reported to have an SEA capability of 31,000 ft-lb/lb, based on the working tube only (Reference 4).

The enormous potential of cyclic strain energy devices is seen by comparing the cyclic strain energy absorption capability of some typical materials with the SEA values noted above. If pure titanium metal, for example, is cycled in a plastic strain range sufficient to produce failure in 100 cycles, the total SEA at failure is approximately 350,000 ft-lb/lb. If the strain range is reduced so that failure occurs in 1000 cycles, the corresponding SEA at failure is approximately 800,000 ft-lb/lb. Similar SEA values are possible with other structural metals. Nonmetals also exhibit enormous cyclic strain energy absorption capacities and have been used extensively in vibration damping

applications for this reason. A certain viscoelastic damping tape is reported to have undergone 1.6 million cycles at a shear strain amplitude of 1.4 with no apparent fatigue failure, which corresponds to an SEA value in excess of 4 million ft-lb/lb (Reference 5).

The energy absorption efficiency of a complete cyclic strain-energy device depends, of course, on the weight-fraction of working material, and other design parameters such as number of strain cycles, cycle rate, temperature rise, stroke length, etc. However, certain performance capabilities and limitations can be established on the basis of material properties, independent of particular design configurations.

The work described herein, with the exception of that described in References 1 and 2, represents an 18-month investigation under NASA Contract NAS 7-226, "Concepts of Multiple-Impact Study of Energy Absorption." The scope of the investigation and a detailed description of the work performed are presented in the following sections.

III   SCOPE OF INVESTIGATION

The major objectives of the investigation were as follows:

(1)   Development of improved methods for the analytical prediction of the characteristics and behavior of cyclic strain energy devices.

(2)   Evaluation of promising materials and confirmation of pertinent energy absorption parameters.

(3)   Design, construction, and testing of appropriate laboratory test devices for demonstration of feasibility and verification of the analytical predictions of energy absorption characteristics.

In Section IV, basic concepts of cyclic strain-energy devices are described and performance capabilities and limitations are discussed. Section V contains a summary of flow and fatigue behavior of materials in relation to cyclic strain energy devices. Metals are characterized in terms of their cyclic plastic stress-strain or hysteresis behavior, and nonmetals are described in terms of dynamic mechanical properties and complex moduli. Two attractive devices are discussed in Section VI and design relations are developed. An experimental program is described in Section VII. The first part of the program is concerned with the design and construction of a cyclic torsion test apparatus and cyclic torison testing of several materials under conditions appropriate to cyclic strain energy devices. The materials tested include 1100-aluminum, 347 stainless steel, molybdenum TZM and nylon 66. Both cyclic stress-strain and fatigue data are presented. The second part of the program involves the construction and testing of the two impact devices discussed in Section VI. Both quasi-static and impact testing are described. Conclusions and recommendations for future work are presented in Section VIII.

IV   BASIC CONCEPTS AND PRINCIPLES OF MULTIPLE-IMPACT CYCLIC STRAIN ENERGY DEVICES

A cyclic strain energy impact device absorbs energy by converting unidirectional motion into cyclic deformation of a working material. The device consists of three

4

basic parts: (1) load transmitter, (2) cycling mechanism, and (3) working elements. However, a single component of the device may serve two of the basic functions.

Two examples of cyclic strain energy devices are the "torus" device* and the "rolling tube" device, illustrated in Figure 1. In both of these devices cyclic deformation of the working elements produces essentially constant resisting forces. In the torus device rolling of the torus element produces cyclic tension and compression of the longitudinal fibers of the element. Similarly, rolling of the compressed tube causes cyclic bending deformation of the tube wall in the circumferential direction. Also, the load-transmitting member and working element serve as the cycling mechanism in both the rolling tube device and the friction torus device shown in the lower right of Figure 1A. More complete discussions of these devices are treated in subsequent sections of the report.

Cyclic strain energy devices such as the torus and rolling tube devices can be operated repeatedly in tension or compression, in contrast to typical "one-shot" devices which can take only one tensile or compressive deformation. Thus, if a crushable material were to be used for energy absorption during multiple landings of a space vehicle, the SEA for the crushable material would be constant, and the total weight required would depend on the SEA and the total energy to be dissipated in all of the landings. By comparison, the SEA for a cyclic-strain energy device depends on the number of impacts since the weight of the device is fixed and each impact adds to the total energy absorption. However, this relation is not quite linear with the number of impacts since, as will be shown later, the amount of working material required depends to some degree on the total energy absorbed.

_____

* A patent is pending on this device wherein all rights have been assigned to ARA, Inc.

Figure 1.   Examples of Cyclic Strain Energy Devices

A.   "Torus" Cyclic Strain Energy Device
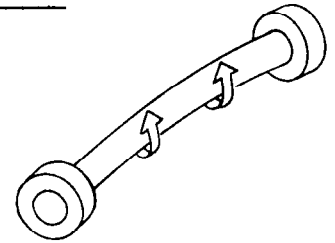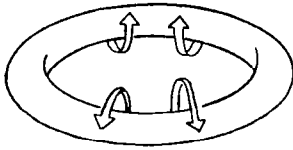
Patent Pending

Basic working element is a torus tube or rod, or a section of a curved tube or rod.   Rolling of element during impact produces cyclic tensile and compressive straining of longitudinal fibers.
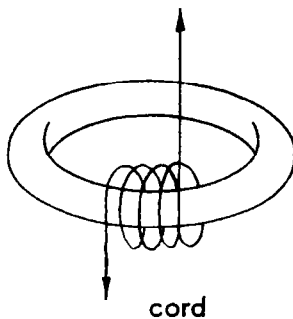
cord
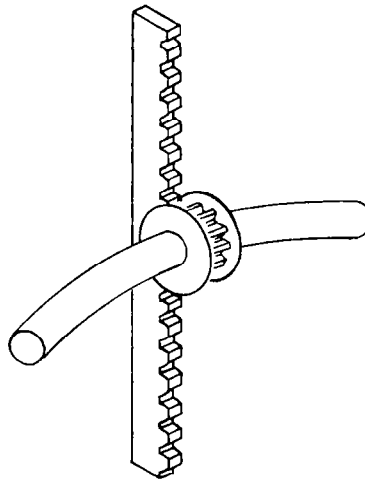
rack and pinion

friction
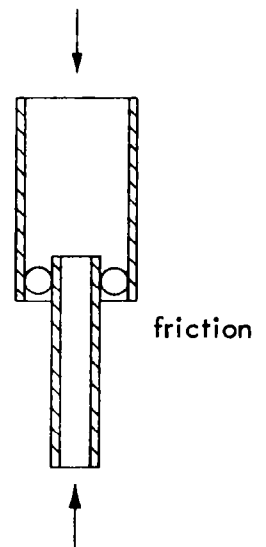
Patent Pending

Rolling of working element during impact can be accomplished by various mechanisms, as indicated above.

Figure 1. Examples of Cyclic Strain Energy Devices (Cont'd)

B. "Rolling Tube" Cyclic Strain Energy Device
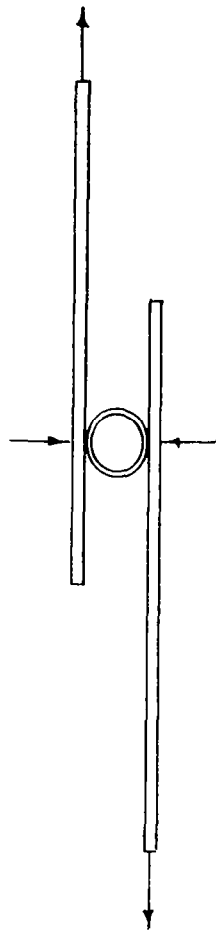
Rolling of the compressed tube produces cyclic bending deformation of the tube wall. Series of plates and tubes can be stacked to provide flexibility in design. Force levels are adjustable by varying lateral compressive force or interference.

The characteristics and performance of cyclic strain energy devices are closely related to the cyclic stress-strain and fatigue behavior of the working material. For example, the load-stroke behavior of an impact device depends directly on the characteristics of the hysteresis loops of the material and variations thereof during impact. Such variations can arise, for example, from changes in stress due to changes in applied strain, rate effects, temperature rise, and strain hardening or softening. Consider the simple example of the friction torus device of Figure 1. If w_p is the area under the hysteresis loop, or energy absorbed per volume of working material per cycle, the total energy absorbed by the material per cycle, ignoring friction, is

$$\int_{V_w} w_p \, dV_w \quad ,$$

where V_w is the total volume of working material. The work done by the resisting force F during stroke dx is related to the strain energy by

$$F \, dx = \left(\frac{d\nu}{dx} \right) dx \int_{V_w} w_p \, dV_w \quad , \tag{1}$$

where $\frac{d\nu}{dx}$ is the number of cycles per unit stroke length. Assume, for simplicity, that $\frac{d\nu}{dx}$ is a constant for the device and that the torus working element is a thin tube so that the material is uniformly strained. Equation (1) then gives

$$F = (const.) \, w_p \quad , \tag{2}$$

i.e., the resisting force depends directly on the size of the hysteresis loop. In general the material will not be strained uniformly and consequently w_p will vary over the volume of working material. Thus, the computation of the integral of Equation (1) can be quite complicated due to the presence of combined stresses as well as the cyclic

8

straining conditions. Also, the device may be designed so that the strain input varies in a particular manner in order to produce prescribed load-stroke behavior and/or to compensate for variations in the hysteresis behavior from other effects.

Although the characteristics and behavior of a cyclic strain energy device during impact are closely related to changes in the hysteresis behavior of the working material, the energy absorption efficiency or SEA depends further on such factors as fatigue behavior and number of impacts required. In general, the higher the strain range through which a material is cycled, the higher the specific energy absorbed per cycle and the lower the fatigue life. However, the total specific energy absorbed at failure is not, in general, a constant for the material but depends on the strain range and number of cycles to failure. For many ductile metals, the total cyclic plastic strain at failure is proportional to the square root of the number of cycles to failure, N (Reference 6), i.e.,

$$\text{total plastic strain} \sim \sqrt{N} \tag{3}$$

Thus, to a first approximation, the SEA for a ductile metal follows a similar relationship,

$$SEA_{ur} = SEA_o \sqrt{N} \tag{4}$$

where SEA_{ur} is the SEA of the working element* and SEA_o is an approximate upper limit for SEA attainable by unidirectional straining of metals.** It is likely that the number of cycles per impact will be fixed by the stroke length, the cycling mechanism,

---

* It is assumed that the working metal is strained uniformly.

** During cyclic plastic straining of metals, the flow stress remains fairly constant due to a pronounced Bauschinger effect. Thus, cyclic plastic strain energy is approximately proportional to cyclic plastic strain. The development of Equations (3) and (4) is presented in Section V.

and other design considerations. Hence, from Equation (4), the SEA for a ductile

metal working element is approximately proportional to the square root of the number

of impacts. However, the working element constitutes only part of the total weight

of the device. Since the remaining weight of the device is approximately independent

of number of impacts and total energy absorbed, the SEA for the total device will

vary between a linear and a square-root dependency on number of impacts, depending

on the weight-fraction of working metal.

Little data is available on large strain fatigue of non-metals and relations

analogous to Equations (3) and (4) have not been established. However, limitations

other than fatigue become significant in cyclic strain applications of non-metals. In

particular, the temperature rise may limit the specific energy absorption capability

of a non-metal during a single impact due to its effect on stress-strain properties and

consequent load-stroke behavior. Further, the fatigue lives of non-metals of interest

are known to depend on test temperature.

It is possible to relate the maximum SEA capability of an impact device to

certain basic material properties of the load transmission member, independent of the

particular design. In a cyclic strain energy device all of the energy absorbed must be

transmitted to the working element through a structural member, and any material

used for this purpose has certain strength-to-weight limitations. Thus, consider a

load transmitter of cross-sectional area A and length L, which produces a resisting

force F. If this member is to retain its structural integrity during impact, the maximum

possible value for F cannot exceed $\sigma_{ult} A$, where σ_{ult} is the maximum tensile or

compressive strength of the material. However, the yield strength σ_y, rather than σ_{ult},

might represent a practical upper limit which would correspond to the resisting force, $\sigma_y A$. If the transmitter element provides this force over its entire length L, the total energy transmitted is $\sigma_y AL$, corresponding to a weight of transmitter $f_t AL$, where f_t is the density of the material. Thus, the maximum SEA capability imposed by the weight and the strength of the load transmitter is given by*

$$SEA_t = \frac{\sigma_y AL}{f_t AL} = \frac{\sigma_y}{f_t} \, , \tag{5}$$

which is simply the strength-to-weight ratio of the load transmitter material. This value is, of course, a theoretical upper limit for the device since there will always be additional weight from the other components. For multiple-impact operation, the maximum total SEA capability for N_I impacts, based on the load transmitter alone, is, from Equation (5),

$$SEA_t(N_I) = \frac{\sigma_y}{f_t} N_I \, . \tag{6}$$

A plot of this relation for several metal alloys, based on data from Reference 7, is shown in Figure 2. It should be noted that Equations (5) and (6) are based on a short column stable up to its yield point. If the column load were limited by buckling, a lower SEA would, of course, result. A lower SEA also results if the stroke length is smaller than the total length of load transmitter. For example, in the friction torus device of Figure 1, the load transmitter is approximately twice the stroke length so that, for this device, an upper limit for SEA is approximately one-half that given by Equation (6). It is seen from Figure 2 that, for multiple impacts, the upper limit of SEA, based

---

*The designation SEA_t is used only for convenience since, of course, the energy transmitter does not absorb energy.

11

Metal Properties (Reference 7)	
Alloy	Specific Strength (1000 in.)
Titanium	1527
Martensitic SS	982
Aluminum	765

SEA$_t$
1,000 ft.-lb/lb

Titanium alloy

Martensitic SS

Aluminum alloy

Number of impacts, N$_I$
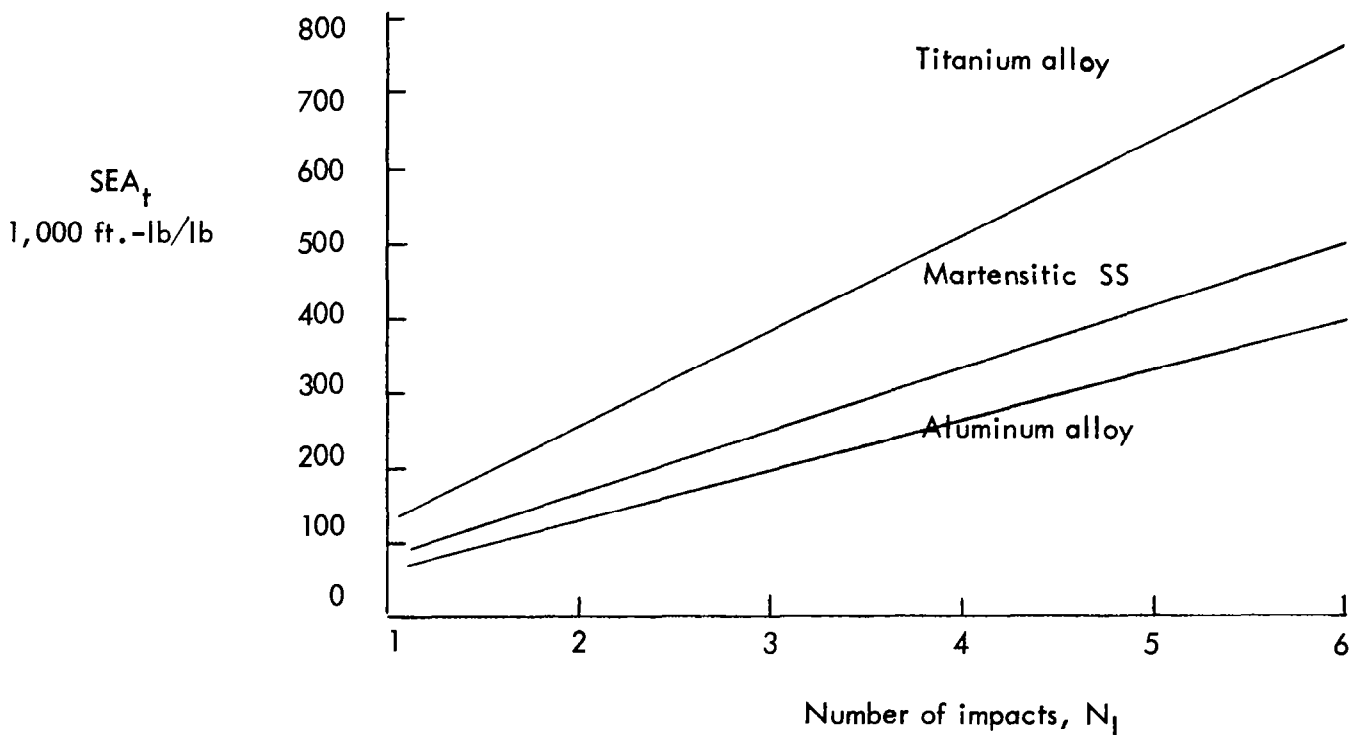
Figure 2.   Upper Limit for SEA based on load transmitter,
for Several Metal Alloys

on the load transmitter, is significantly greater than that attainable by other "one-shot" mechanisms such as crushable materials or deformable structures.

A better estimate of the SEA potential for cyclic strain energy devices can be made by considering the SEA capability including all three components: energy transmitter, energy absorber, and cycling mechanism. Denoting the SEA for each component by an appropriate subscript,* the SEA for the total device can be written

$$SEA = \frac{1}{\frac{1}{SEA_t} + \frac{1}{SEA_w} + \frac{1}{SEA_c}} \quad . \tag{7}$$

Consider now the friction torus device of Figure 1 to consist only of load transmitter and working element (i.e., $1/SEA_c = 0$). From Equations (4), (6), and (7), including a factor of $1/2$ to account for the double length of transmitter, the maximum SEA capability for the device is approximately

$$SEA_{max}(N_I) = \frac{1}{\frac{1}{\frac{1}{2}\frac{\sigma_u}{\rho_t}N_I} + \frac{1}{SEA_o\sqrt{n_I N_I}}} \quad , \tag{8}$$

where n_I is the number of cycles per impact. Values of SEA_{max} are shown in Figure 3, using the data of Figure 2 for the titanium alloy load transmitter, a pure titanium working element, and $n_I = 25$. The values of SEA_w are based on a slightly more accurate relationship than that used in Equation (8). (See Section VA, Figure 13.)

From the foregoing discussion is is apparent that the design objectives for a minimum weight device utilizing metal working elements are: (1) to utilize the load-transmitting material at maximum efficiency, and (2) to cycle the working metal as many times as possible using a minimum-weight cycling mechanism. The objective

---

*As with the energy transmitter, the designation SEA_c for the cycling mechanism is for convenience only and represents the energy absorbed by the device divided by the weight of the cycling mechanism.

Figure 3. Maximum SEA Capability for Friction Torus Device with Titanium Alloy Column and Pure Titanium Working Element ($n_I = 25$ Cycles/Impact)
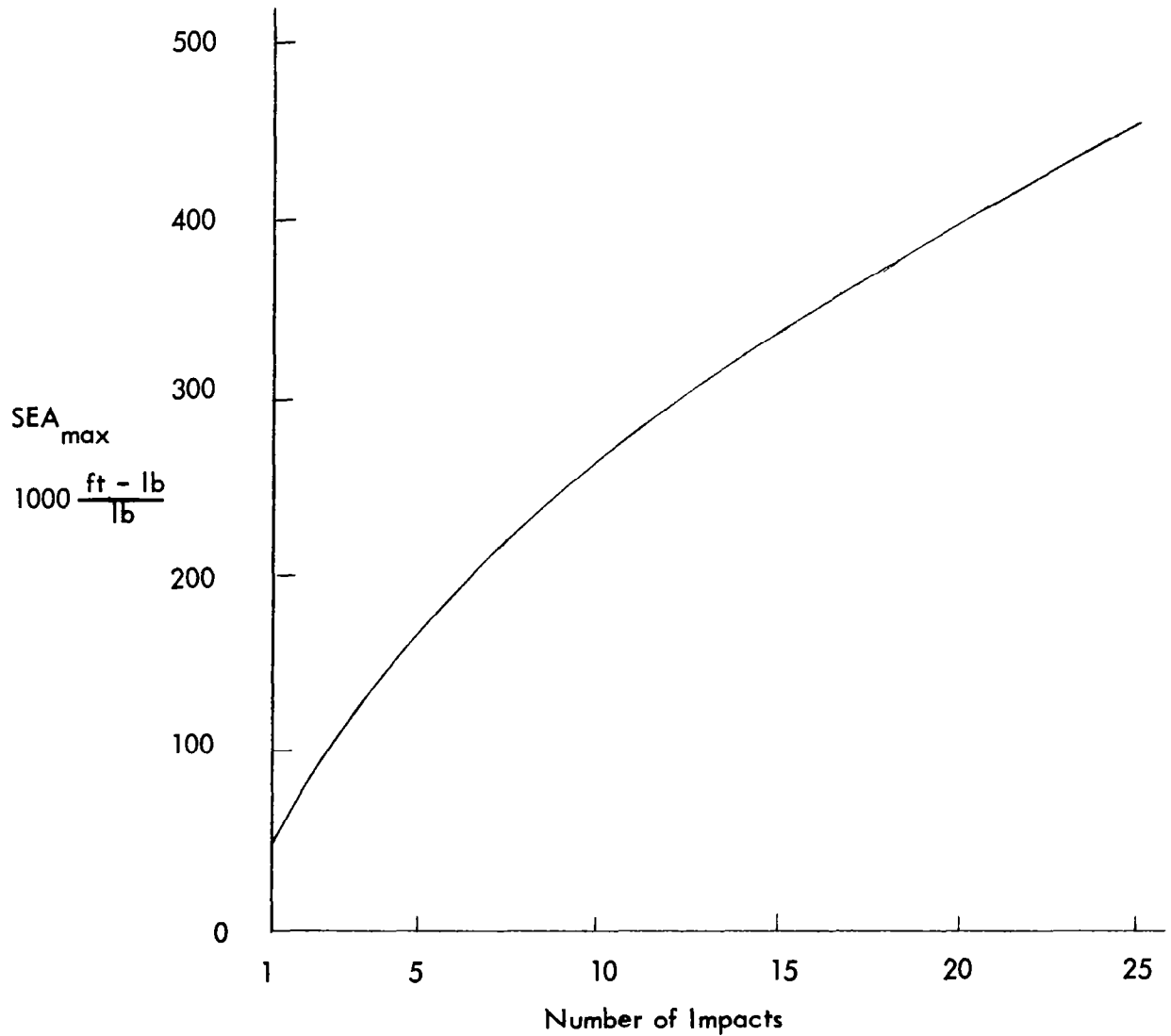
of maximum number of cycles for non-metal working elements cannot be established at the present time since a relationship analogous to Equation (4) has not been established for non-metals. For any cyclic strain energy device the optimum design will, of course, result from the best compromise between the three basic components of the system.

The foregoing discussion has also indicated that cyclic flow and fatigue behavior of materials is central to the behavior and performance of cyclic strain energy devices regardless of the particular design. A discussion of these characteristics is presented in the following section.

V FLOW AND FATIGUE BEHAVIOR OF MATERIALS IN RELATION TO CYCLIC STRAIN ENERGY DEVICES

A. Metals

Flow and fatigue behavior of metals during cyclic plastic straining has been studied rather extensively in recent years, and considerable experimental data has been generated. Although the studies have been principally concerned with evaluating the operational lives of metal structures and machines, many of the results are directly applicable to cyclic strain energy devices.

1. Flow Behavior

In Section IV it was shown that the characteristics and behavior of cyclic strain energy devices utilizing metals can be related directly to the hysteresis behavior during cyclic straining. Some of the pertinent hysteresis parameters are indicated in Figure 4. These are the total strain range, $\Delta \epsilon_T$, the plastic strain range, $\Delta \epsilon_p$, and the maximum stress range, $\Delta \sigma_{max}$. Two other parameters of interest are

15

Figure 4.   Hysteresis Loop for Metals
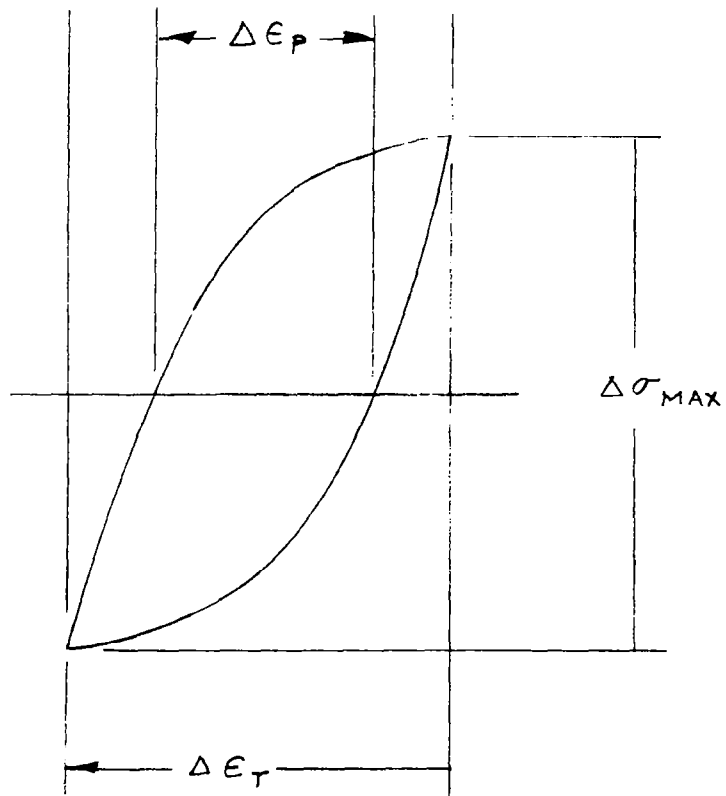
the average stress range, $\overline{\Delta\sigma}$, defined by

$$\overline{\Delta\sigma} \equiv \frac{w_p}{\Delta\epsilon_p} = \frac{1}{\Delta\epsilon_p} \oint \sigma \, d\epsilon_p \quad , \tag{9}$$

and the ratio of average stress range to maximum stress range,

$$\eta \equiv \frac{\overline{\Delta\sigma}}{\Delta\sigma_{max}} \quad . \tag{10}$$

The flow characteristics or stress-strain behavior of ductile metals subjected to cyclic plastic straining have been studied by a number of investigators (References 8-16). Much of the test data has been generated under very low cycling rates where rate and temperature effects are not significant, and few direct measurements have been made of stress-strain behavior during cycling. However, some general behavior trends have been observed which are pertinent to energy-absorbing devices. Some of these are briefly reviewed below.

One of the most significant of these observations is the pronounced Bauschinger effect which is operable in most ductile metals under completely reversed cyclic plastic straining. In the absence of this effect the flow characteristics or strain hardening behavior of metals under cyclic straining conditions might be expected to follow the laws of classical theory of plasticity. According to this theory the state of strain-hardening of a ductile metal depends on the total plastic strain imposed or plastic work done on the metal, and the actual functional relation between stress and strain can be determined from a tensile test. However, in the case of completely reversed cyclic straining of ductile metals, the strain-hardening behavior departs radically from the classical plastic behavior. Rather than hardening with plastic strain according to the tensile curve, the data indicates that strain hardening or softening develops in a relatively

17

small fraction of the life, after which further cycling causes hardening or softening at a rather slow rate. Moreover, the maximum stress to which the material hardens, or the "saturation" stress, depends on the plastic strain range, $\Delta\epsilon_p$. In general, the higher the value of $\Delta\epsilon_p$, the more rapid is the strain-hardening and the higher the "saturation" stress. Quantitative examples of this effect are given in Figures 5 to 8. Figure 5 shows the increase in stress with number of cycles for cyclic straining of 24 ST aluminum alloy at various plastic strain ranges. Because of the large strain ranges, "saturation" occurs very quickly. From the results of Figure 5, a curve of "saturation" stress vs strain range* has been constructed and is shown in Figure 6. Also shown for comparison is the initial true stress-strain curve for the material. "Cyclic" stress-strain curves of this type appear to be a basic property of materials, and are of great importance in the design and analysis of energy-absorbing devices.

In general, cyclic straining causes soft metals to strain-harden and hard metals to strain-soften. Figures 7 and 8 show these effects for hard and soft copper and steel, based on the data of Reference 9. Here, stress amplitude ($\Delta\sigma_{max}/2$) is plotted against total plastic strain ($2N\Delta\epsilon_p$) for different values of total strain range. It appears, from these data, that strain-softening of the hard metals takes place more slowly than strain-hardening of the soft metals. Smith, et al (Reference 16) have studied the cyclic flow and fatigue behavior of a variety of metals and have obtained a fair correlation between the degree of cyclic strain-hardening and softening and the ratio of ultimate strength to yield strength. Hardening always took place when this ratio exceeded 1.4 and softening occurred when the ratio was less than 1.2. Their data also indicate that the most significant changes in stress range usually occur within the first 20 percent of

---

*It might be more meaningful to plot maximum flow stress vs the total strain change in going from zero stress to the maximum.
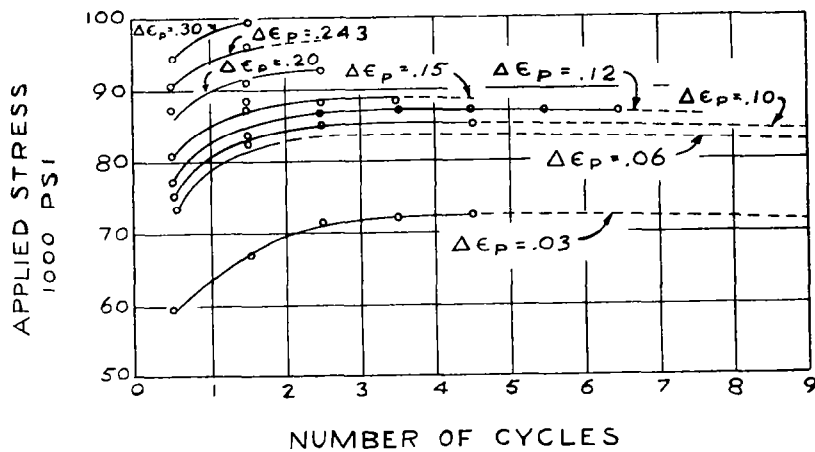
Figure 5. Change in Applied Stress for Cyclic Straining of 24 ST Aluminum Alloy Rod (Data from Liu, et al Reference 8)
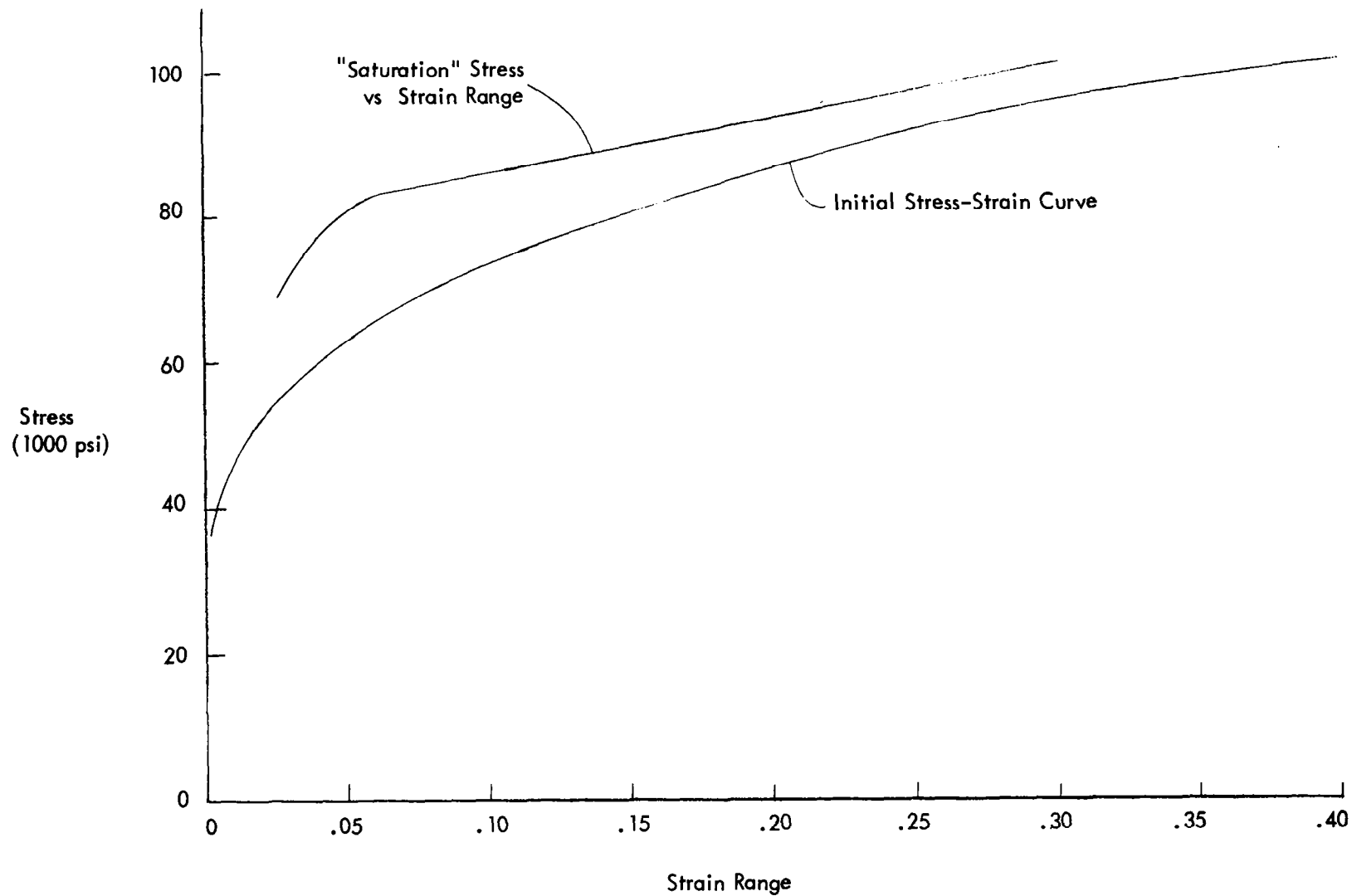
Figure 6. Effect of Strain Range on "Saturation" Stress for 24 ST Aluminum Alloy Rod

(Data from Liu, et al, Reference 8)

a. Soft Copper
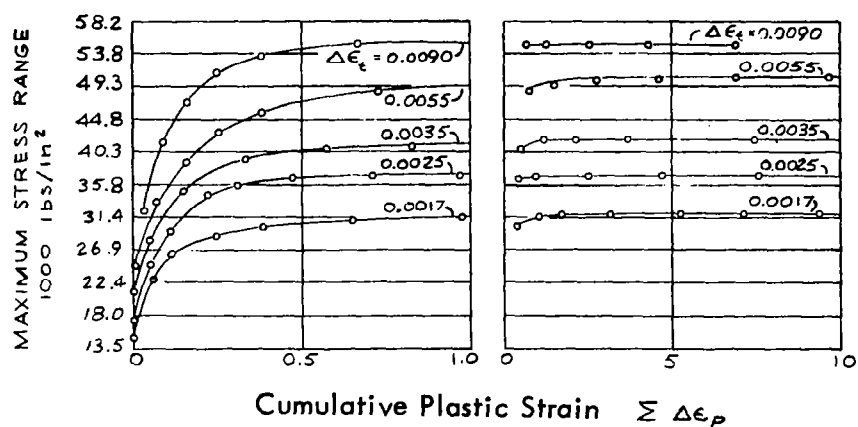
b. Hard Copper
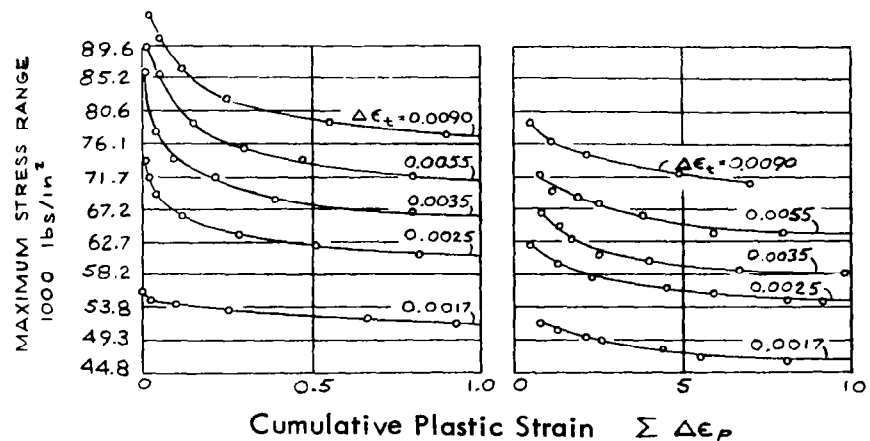
Figure 7. Hardening and Softening of Soft and Hard Copper by Cyclic Plastic Straining (Data from Dugsdale, Reference 9)

a. Soft Steel

Cumulative Plastic Strain $\Sigma \Delta \epsilon_p$

b. Hard Steel
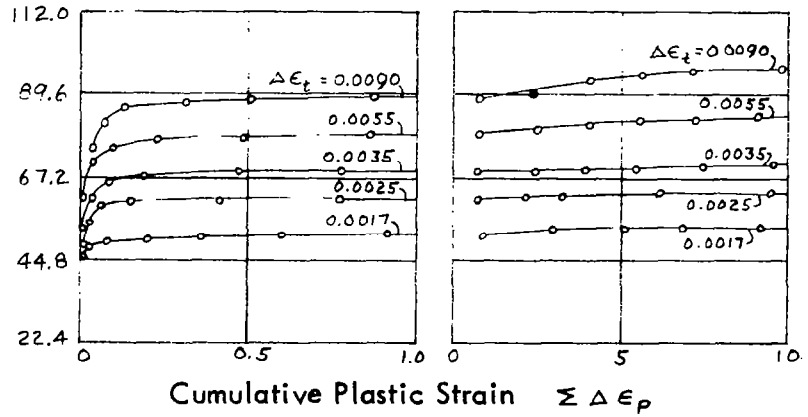
Cumulative Plastic Strain $\Sigma \Delta \epsilon_p$
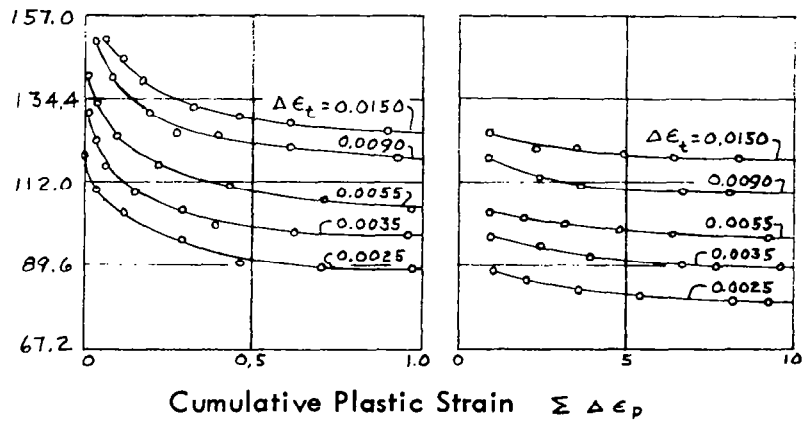
Figure 8.   Hardening and Softening of Soft and Hard Steel by Cyclic Plastic Straining (Data from Dugsdale, Reference 9)

22

specimen life. During the remaining 80 percent or more of the life, the stress range remains relatively constant.

The actual shape of the hysteresis loop, as described, for example, by the parameter η, is also of importance in relation to cyclic strain energy devices. Variations in w_p can occur from variations in η as well as $\Delta\epsilon_p$ and $\Delta\sigma_{max}$. Available data of this type is somewhat limited. However, hysteresis curves for 24ST aluminum alloy (Reference 8), 1100 aluminum alloy and 347 stainless steel (Section VI) indicate that η increases with strain range. This behavior might be expected from consideration of the virgin stress-strain curves for ductile metals.

From the foregoing discussions it is apparent that various changes in the flow characteristics of the working metal during strain cycling can affect the performance and behavior of a cyclic strain energy device. Thus, under different design conditions, three different force-deflection or deceleration-time curves for a device might result, as indicated in Figure 9. Curve A, which might represent the optimum for such a device, could result for the case where the hysteresis loop were established and did not change with cycling during the impact; or, it could result for a case where the hysteresis loop changed but in such a way that the area under the loop remained constant. Curves B and C could result for cases in which the area under the hysteresis loop increased or decreased, respectively, during impact.

From the previous discussion of flow characteristics of metals during cycling, it becomes apparent that an increase in flow stress alone can increase or decrease the area under the hysteresis loop, depending on other parameters of the loop. This is illustrated in Figure 10. Figure 10a represents a case where $\Delta\epsilon_p$ is small compared with

23

FIGURE 9   TYPICAL LOAD-DEFLECTION OR
           DECELERATION - TIME BEHAVIOR
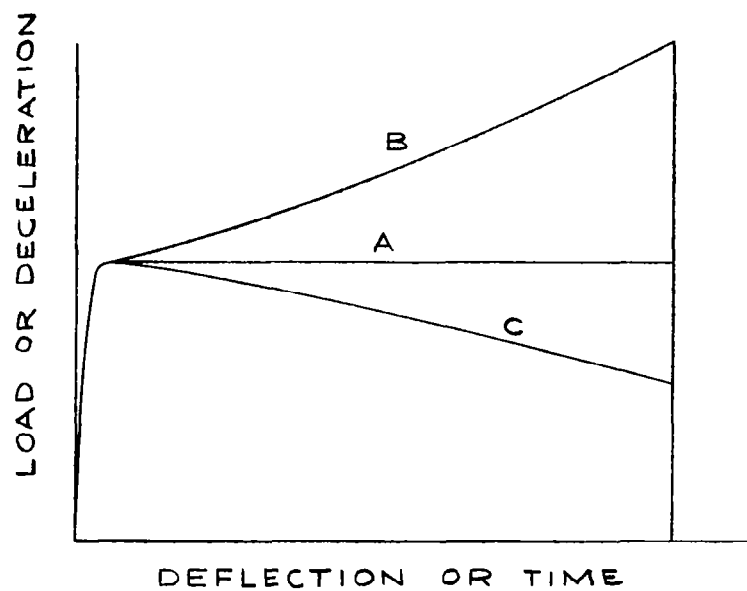
FIGURE 10   EFFECT OF INCREASE IN FLOW STRESS
ON HYSTERESIS LOOP

(a) $\Delta \epsilon_P$ SMALL COMPARED WITH $\Delta \epsilon_T$

$w_P' < w_P$
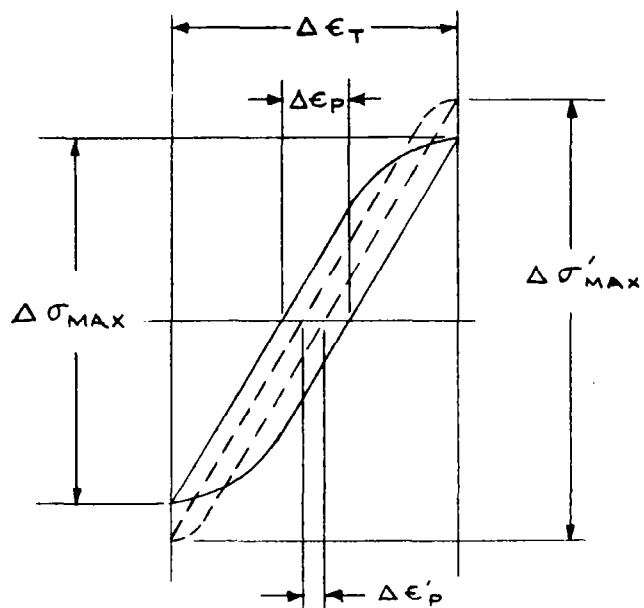
(b) $\Delta \epsilon_P$ ALMOST EQUAL TO $\Delta \epsilon_T$

$w_P' > w_P$
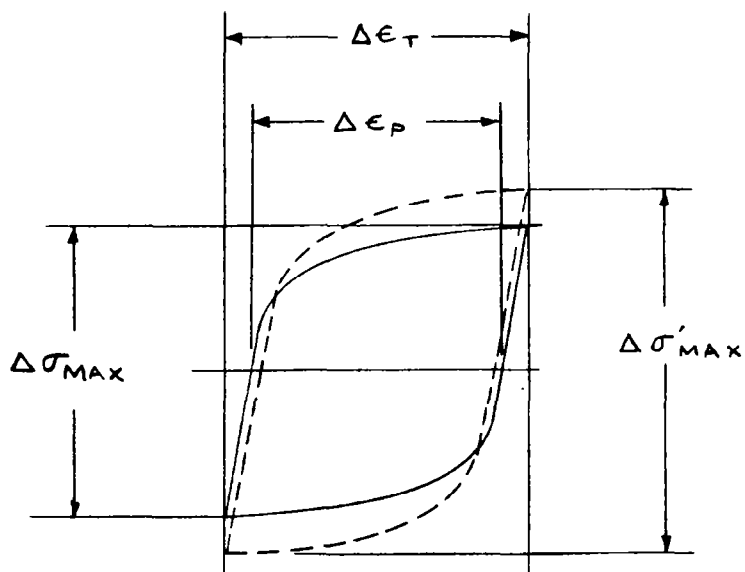
$\Delta\epsilon_T$, i.e., a case where a large number of impacts or a large number of cycles to failure is required. The solid curve represents the hysteresis loop at the start of cycling and the dotted curve represents the loop after an increase in flow stress. It is seen that the increase in stress is more than compensated for by the decrease in $\Delta\epsilon_P$, for a constant value of $\Delta\epsilon_T$, so that the net result is a decrease in ω_P. Figure 10b, by comparison, represents a case where $\Delta\epsilon_P$ is almost equal to $\Delta\epsilon_T$, and would result if only a small number of cycles to failure were required. Here it can be seen that an increase in stress results in an increase in ω_P.

For cases where the elastic strain range, $\Delta\epsilon_E$ is important, such as in Figure 10a, it is convenient to make use of the relations

$$\Delta\epsilon_T = \Delta\epsilon_P + \Delta\epsilon_E \quad , \tag{11}$$

and

$$\Delta\epsilon_E = \frac{\Delta\sigma_{max}}{E} \quad , \tag{12}$$

and to rewrite Equations (9) and (10) in the form,

$$\omega_P = \eta \, \Delta\sigma_{max} \left(\Delta\epsilon_T - \frac{\Delta\sigma_{max}}{E} \right) \quad . \tag{13}$$

From Equation (13) it is possible to estimate the effect of a change in $\Delta\sigma_{max}$ on ω_P. Assuming that η, $\Delta\epsilon_T$, and E remain constant,

$$\frac{d\omega_P}{d\Delta\sigma_{max}} = \eta \left(\Delta\epsilon_T - 2 \frac{\Delta\sigma_{max}}{E} \right) \quad . \tag{14}$$

For example, for the condition where a change in $\Delta\sigma_{max}$ causes no change in ω_P, $\frac{d\omega_P}{d\Delta\sigma_{max}}$ is zero, and Equation (14) gives

$$\Delta\epsilon_T = 2 \, \frac{\Delta\sigma_{max}}{E} \quad . \tag{15}$$

By Equations (11) and (12) it is seen that this corresponds to $\Delta\epsilon_P = \Delta\epsilon_E$. Thus, for $\Delta\epsilon_P < \Delta\epsilon_E$, an increase in $\Delta\sigma_{max}$ during an impact results in a decrease in ω_P, which gives rise to a load-deflection curve of type C in Figure 9. Conversely, a decrease in $\Delta\sigma_{max}$ results in an increase in ω_P and a curve of type B. Similarly, for $\Delta\epsilon_P > \Delta\epsilon_E$, an increase in $\Delta\sigma_{max}$ during impact results in a curve of type B and a decrease in $\Delta\sigma_{max}$ results in a curve of type C.

The "cross-over" value of strain range given by Equation (15) is of interest since, within the limitations of the foregoing assumptions, it corresponds to a hysteresis loop relatively insensitive to changes in $\Delta\sigma_{max}$, and a load-deflection curve of type A in Figure 9. A typical value can be estimated for 24 ST aluminum alloy, using the curves of Figure 6 and a value for E of 10.6×10^6 psi. Taking a value of twice the "saturation" stress for $\Delta\sigma_{max}$, equal to 100,000 psi, the "cross-over" value for $\Delta\epsilon_T$ is about two percent and $\Delta\epsilon_P$ is about one percent. This corresponds to a fatigue life of about 23,000 cycles (Reference 6). Thus for a typical landing impact device using 24 ST aluminum alloy, which produces perhaps 23 cycles per impact, the "cross-over" condition would correspond to a capability of about 1000 impacts.

Two effects which could produce changes in flow stress during an impact are temperature rise and variation in rate of straining. However, if rate-sensitivity effects are of the same order of magnitude for cyclic plastic straining as they are for unidirectional straining, the result of these effects should be small for typical cases of interest. This is demonstrated by the following example.

2.   Rate Effects

Rate sensitivity, n, is defined by

$$n \equiv \left(\frac{\partial \ln \sigma}{\partial \ln \dot{\epsilon}_p} \right)_{\epsilon_p} , \tag{16}$$

27

where σ is the flow stress corresponding to a particular value of ϵ_p and $\dot{\epsilon}_p$ denotes the derivative of ϵ_p with respect to time. This equation is normally used to relate changes in flow stress with changes in uniform strain rate during unidirectional straining. Thus, in the range where Equation (16) is applicable,

$$\sigma \sim \dot{\epsilon}_p^{\;n} \quad , \tag{17}$$

for a given plastic strain, or,

$$n = \frac{\ln(\sigma_2/\sigma_1)}{\ln(\dot{\epsilon}_{P_2}/\dot{\epsilon}_{P_1})} \quad , \tag{18}$$

where the subscripts denote two different strain rates. Rate sensitivity values at room temperature are usually in the neighborhood of 0.01, and those at elevated temperatures are in the neighborhood of 0.1.*

For the present example it is assumed that the strain is applied sinusoidally and that the elastic strain range is negligible so that $\Delta\epsilon_p \simeq \Delta\epsilon_T$. Thus,

$$\epsilon_p = \frac{\Delta\epsilon_p}{2} \sin \omega t \quad , \tag{19}$$

and

$$\dot{\epsilon}_p = \frac{\omega \Delta\epsilon_p}{2} \cos \omega t \quad , \tag{20}$$

where ω is the cyclic frequency and is related to ν by

$$\omega = \frac{1}{2\pi} \frac{d\nu}{dt} \quad . \tag{21}$$

Sinusoidal straining in actual tests gives rise to hysteresis loops of the type previously discussed, as illustrated in Figure 11. Thus, if rate sensitivity effects during cyclic straining were similar to those for unidirectional straining, it would be expected that the maximum stress range at "saturation" would be proportional to $\dot{\epsilon}_p^{\;n}$,

---

*See, for example, Reference 17, pp 171-195.

FIGURE II. RELATION BETWEEN STRESS, STRAIN, AND TIME DURING SINUSOIDAL STRAINING
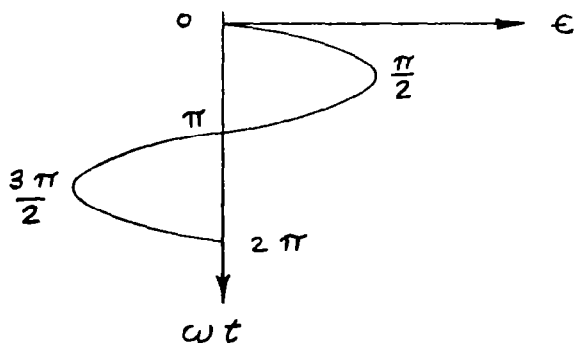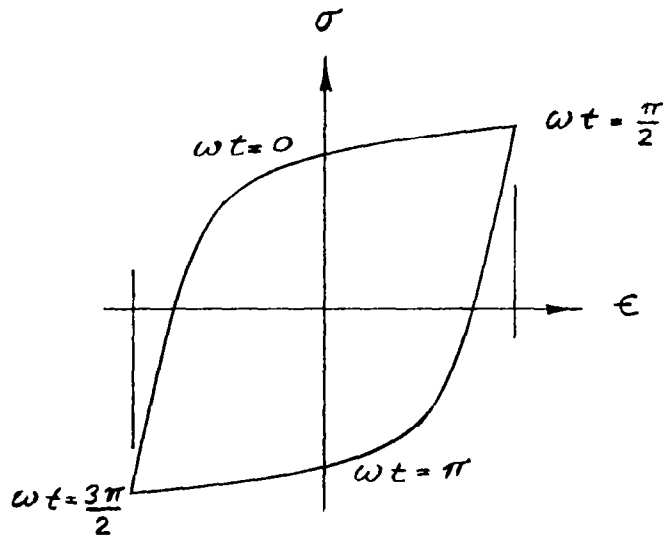
or, by Equations (17) and (20),

$$\Delta\sigma_{max} \sim \omega^n \quad .$$

(22)

Consider the effect of rate sensitivity on an impact device in which the onset velocity v_o corresponds to a cycling frequency ω_o, i.e.,

$$v = \frac{dx}{dt} = \frac{dx}{d\vartheta}\frac{d\vartheta}{dt} = 2\pi\left(\frac{dx}{d\vartheta}\right)\omega \quad ,$$

(23)

or,

$$v = (const.)\,\omega \qquad and \qquad v_o = (const.)\,\omega_o \quad ,$$

(24)

provided $\frac{dx}{d\vartheta}$ is constant.

By Equations (2), (13), (22) and (24),

$$\frac{F}{F_o} = \left(\frac{\omega_p}{\omega_{p_o}}\right)^n = \left(\frac{\Delta\sigma_{max}}{\Delta\sigma_{max_o}}\right)^n = \left(\frac{v}{v_o}\right)^n \quad ,$$

(25)

assuming, as before, that η and $\Delta\epsilon_T$ are constant. Here the subscript o denotes a quantity corresponding to the onset velocity. Thus, as the velocity decreases during impact, rate sensitivity effects give rise to a load-deflection curve of type C in Figure 9. If it is assumed that the effects are small so that the force and deceleration are essentially constant, then*

$$v^2 = v_o^2 + 2ax \quad ,$$

(26)

and

$$\left(\frac{v}{v_o}\right)^2 = 1 - \frac{x}{L} \quad ,$$

(27)

where L is the total stroke length and -a is the deceleration. From Equations (25) and (27), the load-deflection relation can be written

$$\frac{F}{F_o} = \left(1 - \frac{x}{L}\right)^{n/2} \quad .$$

(28)

---

* It is assumed that energy is conserved on initial contact - i.e., negligible heat is generated at contact so that the total kinetic energy is dissipated through cyclic straining.

Assuming, for example, a rate sensitivity of 0.02, the value of $\frac{F}{F_o}$ at x/L = 0.5 would be 0.993. Thus, for typical room temperature rate sensitivity values in the neighborhood of 0.01 this effect would be negligible and the load-deflection curve would be essentially flat. Even for cases where the metal increased in temperature so that the rate sensitivity increased, the effect on the load-deflection behavior should be small, provided, of course, that rate effects for cyclic straining are of the same order of magnitude as for unidirectional straining.

3. Temperature Effects

For cases where the metal temperature increases appreciably, a more significant effect on load-deflection behavior than rate sensitivity will probably be the decrease in flow stress due to the temperature rise. For some ductile metals the change in flow stress during unidirectional straining can be described by a relation which has the form

$$\frac{\sigma}{\sigma_o} = exp\left[K\left(\frac{1}{T} - \frac{1}{T_o}\right)\right] \quad , \tag{29}$$

where K is a constant for the material, T is the absolute temperature, and the subscript 0 refers to some reference temperature. This relation is generally used to describe the effect of temperature on flow stress for a particular strain and strain rate, and the parameter K can be estimated, for example, from tensile strength data. More-over, the extension of such a relation to cases of variable temperature and strain rate histories requires the postulate of a "mechanical-equation-of-state" which ignores tempera-ture and rate history effects. Although there exists evidence that such a concept is general-ly invalid, the error resulting for many load histories is sufficiently small that the con-cept can be used as a first approximation.* Furthermore, the validity of extending this concept to describe saturation flow stress behavior during cyclic plastic straining

* See, for example, Reference 17, Chapter 7

31

has not been verified. However, if it is assumed that the maximum stress range during strain cycling is affected by temperature according to Equation (29), the resulting effect on load-deflection behavior can be estimated.

Assuming, as before, that the elastic strain range is negligible and that $\frac{d\nu}{dx}$, η , and $\Delta\epsilon_T$ are constant, Equations (2), (13) and (29) yield

$$F(x) = F_o \exp\left[-K\left(\frac{1}{T_o} - \frac{1}{T(x)}\right)\right] , \tag{30}$$

where the reference state corresponds to the initial temperature of the metal. The temperature rise is proportional to the plastic work done on the device, provided friction is neglected and the system is adiabatic, so that

$$\frac{dT}{dx} = \frac{F(x)}{M_w c} , \tag{31}$$

where M_w is the mass and c is the heat capacity of the working metal. Combination and integration of Equations (30) and (31) yield the result,

$$T e^{-\frac{K}{T}} - K\left[Ei\left(\frac{-K}{T_o}\right) - Ei\left(\frac{-K}{T}\right)\right] = \left(\frac{F_o}{M_w c} x + T_o\right) e^{-\frac{K}{T_o}} , \tag{32}$$

where Ei is the exponential integral, defined by*

$$Ei(t) \equiv \int_{-\infty}^{t} \frac{e^\tau}{\tau} d\tau , \tag{33}$$

and which can also be expressed in series form by

$$Ei(t) = -\ln t - \gamma + t - \frac{t^2}{2\cdot 2!} + \frac{t^3}{3\cdot 3!} - \frac{t^4}{4\cdot 4!} + \cdots , \tag{34}$$

where $\gamma = 0.5772$. Equation (32) can be solved for different values of T to yield a curve of x vs T. Substitution of these values in Equation (30) then yields the required load-deflection curve.

---

* See, for example, Reference 18, p.96

An example is shown for an impact device utilizing 347 stainless steel as the working metal, which is designed to produce a specific energy absorption in the working metal of 84,000 ft-lb/lb during a single impact. Assuming adiabatic conditions, this produces a $900^{\circ}F$ temperature rise during the impact and a decreasing load-deflection curve. Assuming an initial temperature of $70^{\circ}F$, the value of K for type 347 stainless steel in this range, based on tensile strength data,* is $347^{\circ}F$. With these values, Equations (30) and (32) yield the load-deflection curve shown in Figure 12.

   4.   Fatigue Behavior

In addition to cyclic flow behavior, the performance of cyclic strain-energy devices is closely related to the low-cycle or plastic-strain fatigue behavior of the working material. Specifically, it is necessary to establish a relation between the fatigue life of the material, the hysteresis loop parameters, and other pertinent parameters such as cycle or strain rate and material temperature.

Low-cycle fatigue of metals has been studied rather extensively in recent years and considerable experimental data has been obtained. Manson (Reference 19) and Coffin (Reference 12) independently suggested that low-cycle fatigue of metals follows a relation of the form

$$N^{\alpha} \Delta \epsilon_p = C \, ,$$

(35)

where α and C are constants for the specific material. Tavernelli and Coffin (Reference 6) reviewed the data for a wide variety of metals from a number of investigators and found that Equation (35) with $\alpha = 1/2$ best fits all the data regardless of the metals

---

*Reference 30

33

Figure 12. Load-Deflection Curve for Impact Device Utilizing 347 Stainless Steel Elements. (Impact Produces 900°F. Temperature Rise.)

$\dfrac{F}{F_o}$

Fraction of Stroke
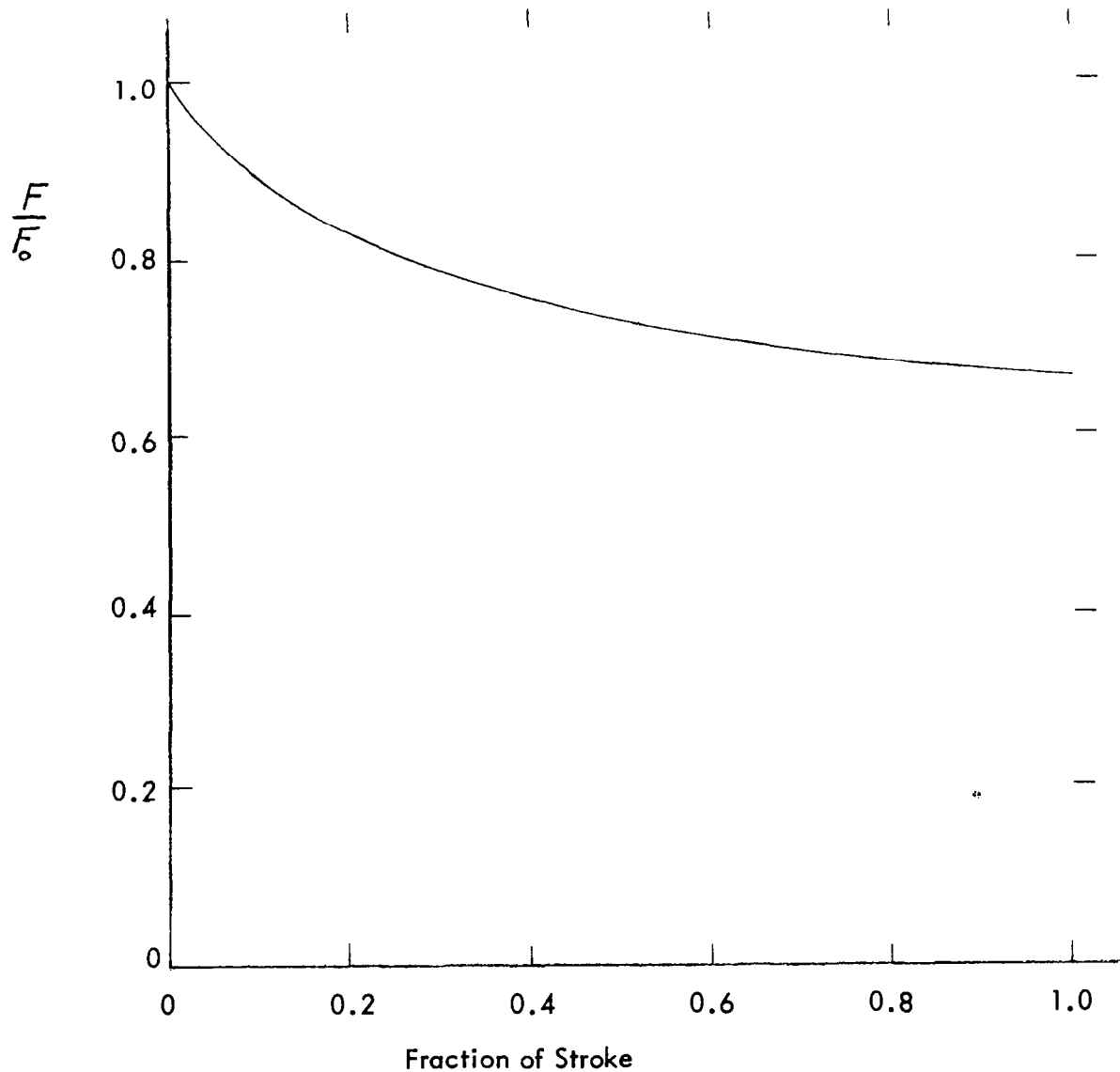
tested, the temperature of testing, and the manner of testing. The resulting equation,

$$N^{\frac{1}{2}} \Delta \epsilon_p = C \, ,$$ (36)

is important in estimating the energy absorption capacity of ductile metals. They also found good agreement when the fracture strain in a tensile test was placed on the curve at $N = 1/4$. Thus, the constant C in Equation (36) and hence the fatigue behavior of the metal can be predicted simply from the fracture strain ϵ_f by

$$C = \left(\frac{1}{4}\right)^{\frac{1}{2}} \epsilon_f = \frac{\epsilon_f}{2} \, .$$ (37)

Nickell and Jacobsen (Reference 20) have conducted an extensive and more recent survey of the literature on low-cycle fatigue. Their study shows that, while plastic or total strain range is an important parameter for predicting low-cycle fatigue failure under mechanically applied loading, neither parameter is useful for predicting cyclic failure under thermally induced loading. This conclusion contradicts the findings of other investigators whose high-temperature fatigue data correlates with Equation (35) but with values of α greater than $1/2$ (Reference 21).

Limited data is available on the effects of cycle frequency although certain trends are apparent. For mechanical cycling at room temperature the effects of cycle frequency for several investigators was found to be negligible (Reference 20). At elevated temperatures cycle frequency becomes an increasingly important parameter; a decrease in cycle frequency results in a considerable decrease in life. (Reference 20). It should be noted that these observations are based on limited data from 1/4 to 10,000 cycles to failure, as well as limited cycle frequencies. Additional investigations are necessary to evaluate more fully the effect of cycle rate on fatigue

life, particularly at the high frequencies of interest for cyclic strain energy devices.

The SEA capability of a ductile metal can be related to the parameters defined in the foregoing discussion. Assuming that w_p is constant over the N cycles to failure, the total SEA capability is, by Equations (9), (19), and (36),

$$SEA_w = \frac{N\, w_p}{\rho_w} = \frac{N\, \eta\, \Delta\sigma_{max}\, \Delta\epsilon_p}{\rho_w} = \frac{\eta\, \Delta\sigma_{max}\, C}{\rho_w}\sqrt{N} \; . \tag{38}$$

Although data for a variety of metals is available on the relation between $\Delta\sigma_{max}$ and $\Delta\epsilon_p$ or N (e.g., References 13 and 16), little corresponding data is available for η . If it is assumed that η and $\Delta\sigma_{max}$ are constant over a limited range of $\Delta\epsilon_p$ or N , Equation (38) becomes the approximate relation of Equation (4), where

$$SEA_o = \frac{\eta\, \Delta\sigma_{max}\, C}{\rho_w} \; . \tag{39}$$

This relation is only a first approximation since, for much of the data available, there is quite a wide variation in $\Delta\sigma_{max}$ with $\Delta\epsilon_p$. To a lesser extent, there is also a variation in $\Delta\sigma_{max}$ with strain cycles for a fixed strain range, although this variation occurs during an initial "stabilizing" period, as explained earlier.

If values of η are assumed in Equation (38), the SEA capabilities for a variety of metals can be computed from flow and fatigue data in the literature. Results of such computations are shown in Figure 13 for several promising structural metals, based on the data of Reference 13 with an assumed value for η of 2/3.

B.   Non-Metals

Flow behavior of non-metals of interest for cyclic strain energy devices can be characterized in terms of viscoelastic or dynamic mechanical properties. These same properties are commonly used to describe the characteristics of viscoelastic
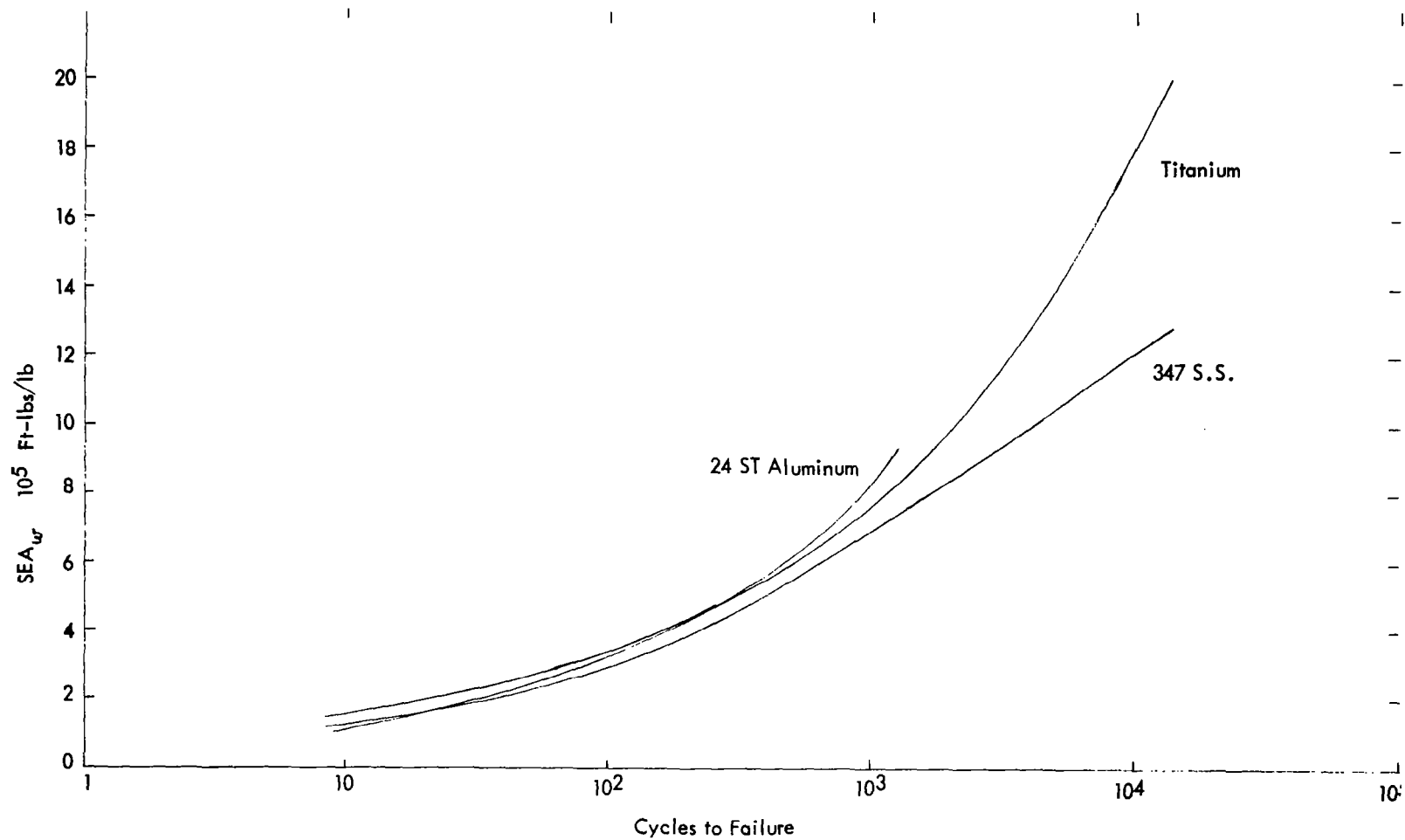
Figure 13.   SEA$_{wr}$ vs   Cycles to Failure for Several Metals

materials used in vibration damping applications. In fact, the quantity W_p used in the foregoing discussions is the specific damping capacity of the material.

If a small sinusoidal strain $\epsilon = \epsilon_o e^{i\omega t}$ is applied to a viscoelastic material, the stress response will also be sinusoidal in the form $\sigma = \sigma_o e^{i(\omega t + \Theta)}$, where Θ is the phase angle between stress and strain. The stress-strain or dynamic mechanical properties for such a material are expressed in terms of a complex modulus E* defined by

$$E^* \equiv \frac{\sigma}{\epsilon} = \frac{\sigma_o}{\epsilon_o} e^{i\Theta} . \tag{40}$$

E* can also be written in terms of its real part, E_1, called the storage modulus, and its imaginary part, E_2, called the loss modulus, i.e.,

$$E^* = E_1 + i E_2 = E_1(1 + i\beta), \tag{41}$$

where

$$\beta \equiv \frac{E_2}{E_1} = \tan \Theta \tag{42}$$

is called the loss factor. The energy absorbed per unit volume per cycle is readily obtained by integrating stress over strain through one cycle. This result can be expressed in the form*

$$W_p = \pi E_2 \epsilon_o^2 , \tag{43}$$

which corresponds to the relation for metals,

$$W_p = \eta \Delta \sigma_{max} \Delta \epsilon_p . \tag{44}$$

The complex modulus E* can be readily obtained from cyclic stress-strain tests by measurements of relative amplitude of stress and strain and phase lag. Considerable data is available for viscoelastic materials at various frequencies and

---

*See, for example, Reference 22, Chapter III.

temperatures (see, for example, References 5, 22-29). Most data of this type has been obtained at very small strains (less than one per cent). Moreover, little fatigue data is available at the larger strains of interest for cyclic strain energy devices. As in the case of metals, both flow and fatigue data are necessary in order to evaluate the characteristics and behavior of these devices.

Most polymeric materials exhibit linear viscoelasticity at very low strains. i.e., a constant relationship exists between the time-dependent stress and strain and, hence, the complex modulus is independent of the magnitude of stress or strain. As the magnitude of stress or strain is increased, a point will be reached at which the original viscoelastic character no longer holds and either a new linear viscoelastic behavior will result or the response will become one of nonlinear viscoelasticity. The point at which the first deviation from linear viscoelasticity occurs is called the limit of linear viscoelastic response (Reference 27). For application to cyclic strain energy devices it would be desirable to know these limits for viscoelastic materials of interest, as well as the behavior characteristics for magnitudes of stress or strain above these limits.

An extensive investigation of the dynamic mechanical properties of soft adhesives under shear deformation was carried out for a wide range of frequencies and strain amplitudes (Reference 5). Frequencies from 0.1 to 120 cps and shear strain amplitudes up to 25 were investigated. Variations in complex modulus and ω_p^r with strain range were shown, and the materials were, in general, non-linear. However, one material(3M tape #466) exhibited values of ω_p^r approximately proportional to the square of strain amplitude over a range of strain amplitudes from about 0.6 to 25

and frequencies from 0.1 to 15 cps. This data indicates a fairly constant loss modulus over this strain range (Equation 43). The fatigue properties of the same material were discussed briefly. In one test the material was reported to have undergone 1.6 million low-frequency cycles at a shear strain amplitude of approximately 1.4 with no apparent failure. This corresponds to an estimated SEA of over 4×10^6 ft-lb/lb.

Some limited cyclic torsion data was obtained under the present program for nylon 66 at shear strain-amplitudes up to approximately 10 per cent. A plot of w_p^{τ} against the square of the strain amplitude indicates severe nonlinearities. These results are discussed in more detail in Section VII. Additional investigations of this type and that of Reference 5 would be desirable in order to evaluate the effects of strain range, frequency, temperature and stress history on specific energy absorption and fatigue. Data of this type is necessary in order to design and to evaluate the performance capabilities of cyclic strain energy devices employing nonmetals.

VI   METHODS OF ANALYSIS

In the present section the foregoing principles are applied to the analyses of the friction torus device and the rolling tube device described earlier. Deformation analyses of the working elements are developed from which design relationships are established.

A.   Friction Torus Device

1.   Approximate Solution Based on Longitudinal Deformation Only

A first approximation can be obtained by treating only the

longitudinal or bending deformation resulting from rolling of the torus element. As will be seen later, the actual deformation is considerably more complex due to the lateral compressive deformation necessary for adequate friction drive. This latter problem is treated in the following section for the case of nonmetallic elements using linear viscoelastic theory.

The basic force relationship is given by Equation (1). For a torus element of diameter d,

$$\frac{dv}{dK} = \frac{1}{2\pi d} \quad , \tag{45}$$

so that Equation (1) becomes

$$F = \frac{1}{2\pi d} \int_{V_w} w_p \, dV_w \quad . \tag{46}$$

Let h be the radial coordinate measured from the element centerline and let R be the average major radius of the torus element. Then, for one torus loop,

$$dV_w = (2\pi R)(2\pi h \, dh) = 4\pi^2 R h \, dh \quad , \tag{47}$$

and the total strain range is given by

$$\Delta \epsilon_T (h) = \frac{2h}{R} \quad . \tag{48}$$

With Equations (47) and (48), Equation (46) can be written,

$$F = \frac{\pi}{2} \frac{R^3}{d} \int_{\Delta \epsilon_T = 0}^{d/R} w_p \, \Delta \epsilon_T \, d\Delta \epsilon_T \quad . \tag{49}$$

The integral can be evaluated from the cyclic torsion data of Section VIIA. However, it is necessary to employ a theory of plastic flow in order to apply the shear data to the present case of tension and compression. Using the octahedral shear criterion,[*]

---

*See, for example, Ref. 17, Chap. 8

41

with the approximation,

$$\Delta \epsilon_T \simeq \frac{\Delta \gamma_T}{\sqrt{3}} \quad , \tag{50}$$

Equation (49) becomes

$$F = \frac{\pi}{6} \frac{R^3}{d} \int_{\Delta \gamma_T = 0}^{\sqrt{3}\, d/R} \omega_P \, \Delta \gamma_T \, d\Delta \gamma_T \quad . \tag{51}$$

This result will be applied to the predictions of performance

of the laboratory test devices utilizing aluminum and nylon working elements, described

in Section VIIB.

2.   Effect of Lateral Compression on Force Required to Roll a

Viscoelastic Cylindrical Rod

The lateral compression required for adequate friction drive

results in a complex mode of deformation superimposed on the longitudinal or bending

deformation of the torus element. In fact, this deformation alone can be utilized with

a straight element to produce a cyclic strain energy device similar to the rolling tube

device.

In order to evaluate this mode of energy absorption, an analytical

method is developed for predicting the force required to roll a viscoelastic cylindrical

rod compressed between two parallel surfaces. The amount of compression is specified

in terms of the interference Δd relative to the diameter d of the unrestrained cylinder,

as shown in Figure 14.

42
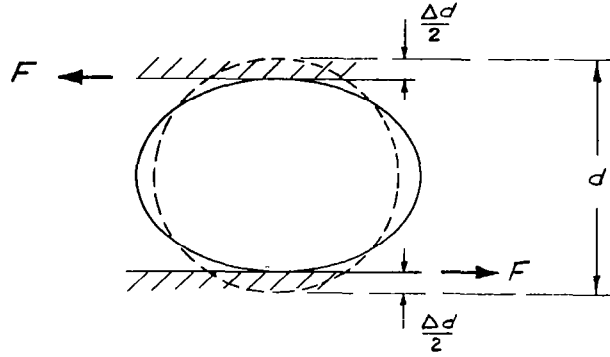
Figure 14. Lateral Compression of Cylinder

The force F required to roll the rod is proportional to the total irreversible strain energy of deformation produced throughout the volume of working material. The force relation has been given previously in Equation (1). Considering that elements on a radial section undergo one complete stress cycle in one-half revolution of the rod, the number of cycles per unit stroke length, $\frac{dv}{dx}$, is equal to $\frac{1}{\pi d}$. The force relation, Equation (1), for this case then becomes

$$F = \frac{1}{\pi d} \int_{V_{w}} w_{p} \, dV_{w} \quad .$$ (52)

The problem remains to determine the integral of Equation (52) corresponding to the spatial distribution of cyclic stresses produced in the viscoelastic rod from lateral compression.

It is shown in Equation (43) that for sinusoidal cyclic straining of a viscoelastic material, the energy absorbed per unit volume per cycle can be expressed in terms of the strain amplitude and loss modulus (the imaginary part of the complex modulus). The energy absorption may also be expressed in terms of stress amplitude, according to

$$w_{p} = \frac{\pi E_{2}}{|E^{*}|^{2}} \sigma_{0}^{2}$$ (53)

43

noting that the magnitude, $|E^*|$ of the complex modulus is equal to the ratio $\frac{\sigma_o}{\epsilon_o}$ of

the stress amplitude to strain amplitude. Similarly, for cyclic shear deformation, the

energy absorption is given by the analogous expression

$$W_P = \frac{\pi\, G_2}{|G^*|^2}\, \zeta_o^2 \quad , \tag{54}$$

where ζ_o is the amplitude of the cyclic shear stress and G^* and G_2 are the complex

shear modulus and loss modulus, respectively.   The extension of Equation (54) to

the general case of combined stress yields the relation,

$$W_P = \frac{\pi\, G_2}{2\,|G^*|^2}\, (\sigma_{1_o}'^{\,2} + \sigma_{2_o}'^{\,2} + \sigma_{3_o}'^{\,2}) \quad , \tag{55}$$

where σ_{1_o}', σ_{2_o}' and σ_{3_o}' are the amplitudes of the principal deviator stress components.

Substituting Equation (55) into Equation (52) and integrating over the cross-sectional

area, the force becomes

$$F = \frac{\pi\, G_2}{2\,|G^*|^2}\, \frac{L}{a} \int_0^a (\sigma_{r_o}'^{\,2} + \sigma_{\theta_o}'^{\,2} + \sigma_{z_o}'^{\,2})\, h\, dh \quad , \tag{56}$$

where $a = d/2$ is the rod radius and L is its length. It should be noted that Equation

(54) is based on complete stress and strain reversals, which is not the case for the

present deformation, so that Equation (56) is only an approximation. However, an

effective stress amplitude based on one-half the stress range should give reasonably

good results.

The stress amplitude can be obtained by noting that, in the

case of the first boundary value problem (stresses specified over the boundary), the

stress distribution in an incompressible linear viscoelastic material is identical with

that in an incompressible elastic material under the same instantaneous surface forces

44

(Reference 33). Some results are available in the literature for the elastic problem and, by making a slight approximation, the required stress distributions can be readily obtained.

Reference 34 gives an expression for the maximum stress produced for a given interference, Δd , in compressing a cylinder between two plates, as shown in Figure 14. The maximum stress occurs at the points of contact, and an expression is given for the total compressive force. The stress distribution throughout the cross-section can be obtained by considering the problem of a cylinder subjected to uniformly distributed loads, as shown in Figure 15, defined such that the maximum
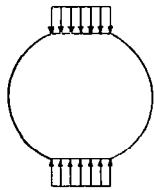
Figure 15.   Cylinder subjected to Uniform Compressive Loads

stress and total compressive force are the same as for the cylinder compressed between two plates. A solution to the problem of Figure 15 can be obtained as follows:

If a uniformly distributed load, q , is applied to the surface of a semi-infinite medium, as shown in Figure 16, it can be shown (Reference 35) that the principal stresses at any point depend only on the angle α subtendend by the end points of the load distribution, and are given by

$$\left. \begin{array}{l} \sigma_I = -\dfrac{q}{\pi} \left(\alpha + \sin \alpha \right) \\[2mm] \sigma_{II} = -\dfrac{q}{\pi} \left(\alpha - \sin \alpha \right) \end{array} \right\} \quad . \tag{57}$$

$\mathscr{Z} =$ Uniform load

Figure 16.   Uniform Load Applied to Semi-Infinite Medium

The directions of the principal stresses lie along and perpendicular to a line which

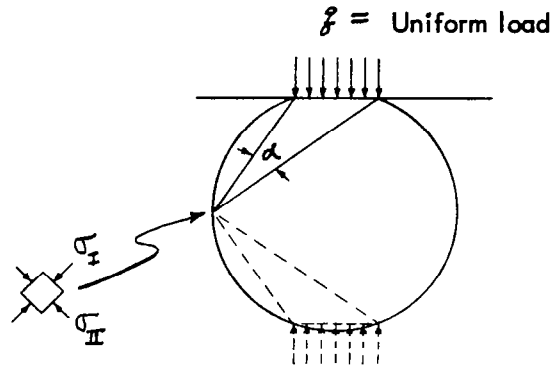bisects the angle α . On any circle which passes through the end points of the load,

the angle α will be constant, e.g., $\alpha = \alpha_o$, and the magnitudes of the principal stresses

will also be constant. By considering an equal and opposite distribution of load, as

shown in Figure 16, it is seen from symmetry that at any point along the circular boundary,

there will exist a constant hydrostatic pressure $\mathscr{P}$ given by

$$ \mathscr{P} = \sigma_{\text{I}} + \sigma_{\text{II}} = -\frac{2\mathscr{Z}\alpha_o}{\pi} \quad . \tag{58} $$

If a uniform hydrostatic tension of magnitude $\frac{2\mathscr{Z}\alpha_o}{\pi}$ is superposed on the stress distributions

resulting from the two opposite loads, the stresses along the circular boundary will vanish

and the stress distribution will correspond to that for a cylinder subjected to the equal

and opposite distributed loads $\mathscr{Z}\left(1 + \frac{2\alpha_o}{\pi}\right)$ and free from external forces on the remainder

of its boundary.

It is seen from symmetry that the stresses along any radial section

will pass through maxima and minima as the radial section rotates through the vertical

46

and horizontal positions. Assuming a sinusoidal variation, the amplitude σ_{i_o}' of the

cyclic stress, from Equation (55), is equal to one-half of the difference between the

two extreme values at any radial position k; i.e.,

$$\sigma_{i_o}'(k) = \frac{1}{2}\left[\sigma_{i_o}'(k)\bigg|_{vertical} - \sigma_{i_o}'(k)\bigg|_{horizontal} \right] . \tag{59}$$

It can be shown that the summation of deviator stress amplitudes appearing in the

integrand of Equation (56) may be written

$$\sigma_{k_o}'^2 + \sigma_{\theta_o}'^2 + \sigma_{z_o}'^2 = \frac{1}{36}\left[5(\sigma_k^v - \sigma_k^h)^2 + 5(\sigma_\theta^v - \sigma_\theta^h)^2 \right. \tag{60}$$

$$\left. + (\sigma_k^h + \sigma_\theta^h)^2 + (\sigma_k^v + \sigma_\theta^v)^2 + 8(\sigma_k^v - \sigma_k^h)(\sigma_\theta^h - \sigma_\theta^v) - 2(\sigma_k^h + \sigma_\theta^h)(\sigma_k^v + \sigma_\theta^v) \right]$$

where $(\sigma_k^v, \sigma_\theta^v)$ and $(\sigma_k^h, \sigma_\theta^h)$ are the principal stresses in the k and θ directions along

the vertical and horizontal radii, respectively. Using Equation (57), and evaluating

the angles α along these radii, the principal stresses are found to be

$$\sigma_k^v = \frac{P}{\pi\ell(1 + \frac{2\alpha_o}{\pi})}\left[\sin^{-1}\beta + \beta + \sin^{-1}\gamma + \gamma - 2\alpha_o \right] , \tag{61}$$

$$\sigma_\theta^v = \frac{P}{\pi\ell(1 + \frac{2\alpha_o}{\pi})}\left[\sin^{-1}\beta - \beta + \sin^{-1}\gamma - \gamma - 2\alpha_o \right] , \tag{62}$$

$$\sigma_k^h = \frac{2P}{\pi\ell(1 + \frac{2\alpha_o}{\pi})}\left[\sin^{-1}\delta - \epsilon - \alpha_o \right] , \tag{63}$$

$$\sigma_\theta^h = \frac{2P}{\pi\ell(1 + \frac{2\alpha_o}{\pi})}\left[\sin^{-1}\delta + \epsilon - \alpha_o \right] , \tag{64}$$

where

$$\alpha_o \equiv \sin^{-1}\frac{4\lambda}{\lambda^2+4} \qquad\qquad \epsilon \equiv \frac{2\lambda(1-\rho^2)}{(1+\rho^2)^2}$$

$$\beta \equiv \frac{2\lambda(1-\rho)}{\lambda^2+(1-\rho)^2} \qquad\qquad \rho \equiv k/a$$

$$\gamma \equiv \frac{2\lambda(1+\rho)}{\lambda^2+(1+\rho)^2} \qquad\qquad \lambda \equiv \ell/2a$$

$$\zeta \equiv \frac{2\lambda}{1+\rho^2}$$

$$(65)$$

and ℓ is the width of the boundary over which the uniform load acts. From Reference 34, the reduction in diameter Δd from compressing an elastic cylinder between two rigid plates is related to the total compressive load P according to

$$\Delta d = 4P\,\frac{(1-\nu^2)}{\pi E}\left(\frac{1}{3}+\ln\frac{2d}{b}\right)\quad, \tag{66}$$

where b is the actual contact area and is given by

$$b = 1.6\sqrt{Pd\,\frac{(1-\nu^2)}{E}}\quad. \tag{67}$$

The maximum stress, for this case, is

$$\sigma_{c_{max}} = 0.798\sqrt{\frac{PE}{d(1-\nu^2)}}\quad, \tag{68}$$

and occurs at the contact surface. Substituting the quantity $\dfrac{P(1-\nu^2)}{E}$ from Equation (67) in Equation (66), the interference Δd for a given diameter d can be expressed in terms of the width, b, of the contact area according to

$$\Delta d = 0.498 \frac{b^2}{d}\left(\frac{1}{3} + \ell_n \frac{2d}{b}\right) \quad . \tag{69}$$

If the maximum stress P/ℓ , in the case of the uniform compressive load, is equated to the maximum stress from Equation (68) for the actual case, the width ℓ is found to be

$$\ell = 1.25\sqrt{\frac{Pd(1-\nu^2)}{E}} \quad . \tag{70}$$

Comparing this value with b from Equation (67), it is found that the width of the uniform load distribution to give the same total load and maximum stress as for the cylinder compressed between plates is related to the contact width for the latter case according to

$$\ell = 0.783\, b \quad . \tag{71}$$

Thus, for a given interference Δd, the value ℓ which appears in the stress amplitude distributions, Equations (61)-(64), can be obtained from Equations (69) and (71). The total load P is obtained from Equation (70) recalling that the stress distribution in an incompressible linear viscoelastic material is identical with that in an incompressible elastic material under the same instantaneous surface forces. Consequently, E in Equation (70) becomes $3|G^*|$ and $\nu = 1/2$. Equation (70) then becomes

$$P = 1.28\, |G^*|\, \frac{\ell^2}{a} \quad . \tag{72}$$

Substituting Equations (60 – 65) in Equation (56), using P from Equation (72) and writing the integral in nondimensional form, the force reduces to an expression of the form

$$F = \frac{1.04\, L\, a\, \lambda^2\, G_2}{(1 + \frac{2\alpha_o}{\pi})^2} \int_0^1 f(\rho)\, \rho\, d\rho \quad . \tag{73}$$

The function $f(\rho)$ is obtained from Equation (60), excluding the coefficient $\dfrac{P}{\pi \ell (1 + \frac{2\alpha_o}{\pi})}$ from the principal stresses, Equations (61 – 64); i.e.,

$$f(\rho) = \frac{\sigma_{k_o}'^2 + \sigma_{\theta_o}'^2 + \sigma_{z_o}'^2}{\dfrac{P^2}{\pi^2 \ell^2 (1 + \frac{2\alpha_o}{\pi})^2}} \quad . \tag{74}$$

The foregoing result will be used in conjunction with the test results obtained with the torus device utilizing nylon elements, as discussed in Section VIIB.

B.   Rolling Tube Device

1.   Theoretical Analysis

The key problem area in predicting the behavior and performance of a rolling tube device is the prediction of the deformation behavior of the tube itself (1) during lateral compression; and (2) during subsequent rolling. The first problem is treated for a metal tube with the aid of an incremental technique developed for analyzing corrugated metal structures in the plastic range (Reference 31). The results of this analysis are then used in conjunction with some simplifying assumptions concerning the cyclic stress–strain behavior of the metal in order to predict the subsequent deformation behavior of the tube during rolling.

Consider a thin tube of radius, ℓ , and wall thickness, h , subjected to two opposing line loads, f_c, as shown in Figure 17a. The problem of interest is to describe the complete load-deformation behavior as the tube is compressed into the plastic range.
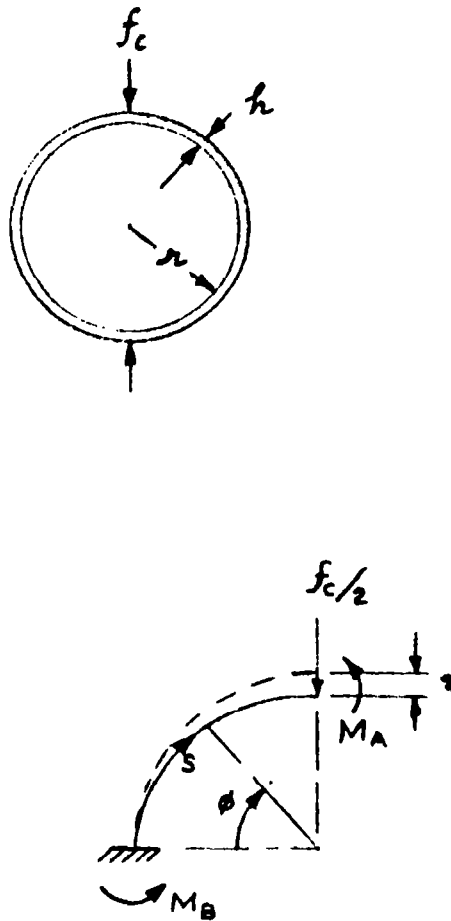
50

Figure 17. Bending Analysis Parameters and Coordinates

The basic model used in the analysis is described by the following assumptions:

1. The tube is compressed uniformly such that the walls are in a state of plane strain bending.

2. Classical small-deflection bending theory is applicable (e.g., cross-sections remain plane).

3. The stress-strain behavior of the material is the same in tension and compression.

From the foregoing assumptions, in conjunction with symmetry considerations, it is necessary to treat only one quarter of the tube, as indicated in Figure 17b. This segment can be treated as a curved cantilever beam, loaded as shown, such that the change in slope is zero at the free end.

The bending equation can be written,

$$\frac{d\,\Delta\theta}{d s} = \frac{M}{D'} \quad ,$$

(75)

where $\frac{d\,\Delta\theta}{d s}$ is the change in curvature, s is the arc length, M is the moment per unit axial length (positive in the clockwise direction), and D' is an effective flexural rigidity defined by Equation (75). In the elastic range,

$$D' = D \equiv \frac{E\,h^3}{12(1-\nu^2)} \quad ,$$

(76)

where E and ν are Young's modulus and Poisson's ratio, respectively.

With the moment distribution given by

$$M = \frac{f_c}{2}\,h\,\cos\varphi - M_A \quad ,$$

(77)

52

(M_A is taken positive as shown) Equation (75) can be written,

$$d\Delta\theta = \frac{f_c h^2}{2} \frac{\cos\varphi}{D'(\varphi)} d\varphi - M_A h \frac{d\varphi}{D'(\varphi)} \quad . \tag{78}$$

It should be noted that, in general, D' is a function of M and, hence, φ.

The conditions that the change in slope be zero at $\varphi = 0$ and

$\varphi = \pi/2$ require that

$$\int_0^{\pi/2} \left[\frac{f_c h^2}{2} \frac{\cos\varphi}{D'(\varphi)} - \frac{M_A h}{D'(\varphi)} \right] d\varphi = 0 \quad ,$$

or,

$$\frac{f_c h}{2} \int_0^{\pi/2} \frac{\cos\varphi \, d\varphi}{D'(\varphi)} = M_A \int_0^{\pi/2} \frac{d\varphi}{D'(\varphi)} \quad . \tag{79}$$

This relation and a knowledge of D' vs M, with Equation (77) can be used to deter-

mine M_A and $M(\varphi)$ for a given value of f_c. It is convenient to introduce the

moment at the proportional limit M_{PL}, defined by

$$M_{PL} \equiv \frac{h^2 \sigma_{PL}}{6} \quad , \tag{80}$$

where σ_{PL} is the proportional limit stress. Equation (79) can then be rewritten in

the form,

$$\int_0^{\pi/2} \frac{\cos\varphi \, d\varphi}{\frac{D'}{D}(\varphi)} = \frac{\frac{M_A}{M_{PL}}}{\frac{f_c h}{2 M_{PL}}} \int_0^{\pi/2} \frac{d\varphi}{\frac{D'}{D}(\varphi)} \quad . \tag{81}$$

The D' vs M relation can be computed by an analytical

procedure such as that developed in Reference 31, or it can be determined experimentally.

With this relation and Equation (80), values of M_A can be guessed and the integrals

of Equation (81) can be evaluated numerically until Equation (81) is satisfied. For these calculations, it is convenient to express D'/D in terms of the nondimensional moment, M/M_{PL}, and use Equation (77) expressed in the nondimensional form,

$$\frac{M}{M_{PL}} = \frac{1}{2} \frac{f_c \, h}{M_{PL}} \cos \varphi - \frac{M_A}{M_{PL}} \quad . \tag{82}$$

When the moment distribution has been determined, the corresponding deformation can be computed by the incremental technique developed in Reference 31. In this procedure the curved cantilever beam is approximated by a series of short straight cantilever beams, each having a linear distribution in M and D'. The rotations and deflections for each of the incremental cantilever beams are accumulated from the base of the curved cantilever beam and the resulting end deflection, η is determined.

Using the notations of Figure 18, the incremental deformation relations can be written

$$\delta_i' = \frac{2}{\lambda} \frac{(M_{i-1}/M_{PL})(\ell_i/h)}{D_{i-1}'/D} \left[\frac{1}{\beta_i} \left(1 + \frac{\alpha_i}{\beta_i} \right) \ell_n (1+\beta_i) - \frac{\alpha_i}{\beta_i} \right] \quad ,$$

$$\frac{\delta_i}{h} = \frac{2}{\lambda} \frac{(M_{i-1}/M_{PL})(\ell_i/h)^2}{D_{i-1}'/D} \left\{ \frac{1}{\beta_i} \left(1 + \frac{\alpha_i}{\beta_i} \right) \left[\frac{1}{\beta_i} (1+\beta_i) \ell_n (1+\beta_i) - 1 \right] - \frac{\alpha_i}{2\beta_i} \right\} \tag{83}$$

where the subscripts on M and D designate quantities evaluated at the end of the i-th incremental cantilever; α_i and β_i are defined by

$$\alpha_i \equiv \frac{M_{i-1} - M_i}{M_{i-1}} \quad , \quad \beta_i \equiv \frac{D_i' - D_{i-1}'}{D_{i-1}'} \quad , \tag{84}$$
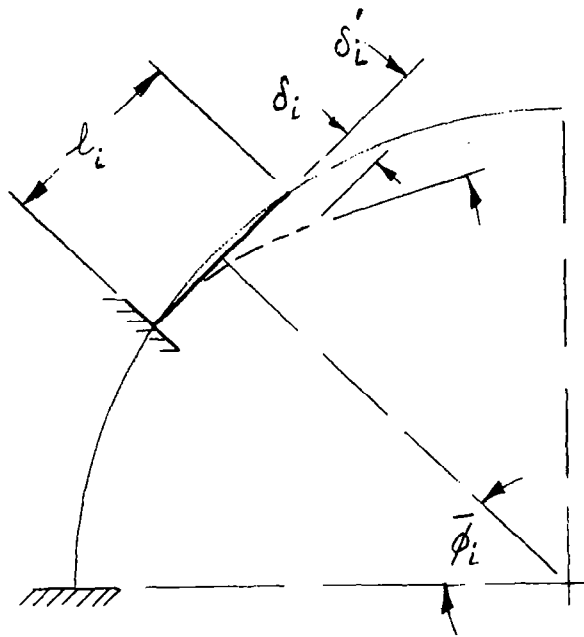
54

Figure 18. Parameters Used in Incremental Deformation Analysis

and

$$\lambda \equiv \frac{1}{(1-\nu^2)} \frac{h}{\hbar} \frac{E}{\sigma_{PL}} \tag{85}$$

With these relations, the incremental vertical deflection for the i-th incremental

cantilever beam can be written

$$\eta_i - \eta_{i-1} = \left(\delta_i + \ell_i \sum_{k=0}^{i-1} \delta_k' \right) \sin \overline{\phi_i} , \tag{86}$$

where

$$\eta_0 = \delta_0' = 0 .$$

It is important to determine the maximum bending strain that

occurs for a given loading condition, since this strain is closely related to the energy

absorption capability of the tube during rolling. With the basic assumption of clas-

sical bending theory that cross-sections remain plane, the maximum bending strain, ϵ_m,

is given by

$$\epsilon_m = \frac{h}{2} \frac{d \Delta \phi}{d s} = \frac{h}{2} \frac{M}{D'} , \tag{87}$$

or, making use of the previous definitions,

$$\epsilon_m = (1-\nu^2) \frac{\sigma_{PL}}{E} \frac{M/M_{PL}}{D'/D} . \tag{88}$$

Additional expressions are required to relate the cyclic strain

energy to the maximum bending strains so that the driving force can be determined in

terms of the lateral compressive force and diametral interference. Consider the hysteresis

loop for a typical fiber to be related to the various circumferential positions of the tube

as shown in Figure 19. The total strain range $\Delta \epsilon_T$ is the sum of the absolute magnitudes

of the bending strains for the fiber at points A and B. For simplicity, the stress-strain
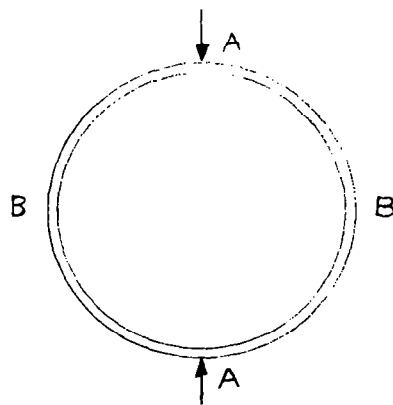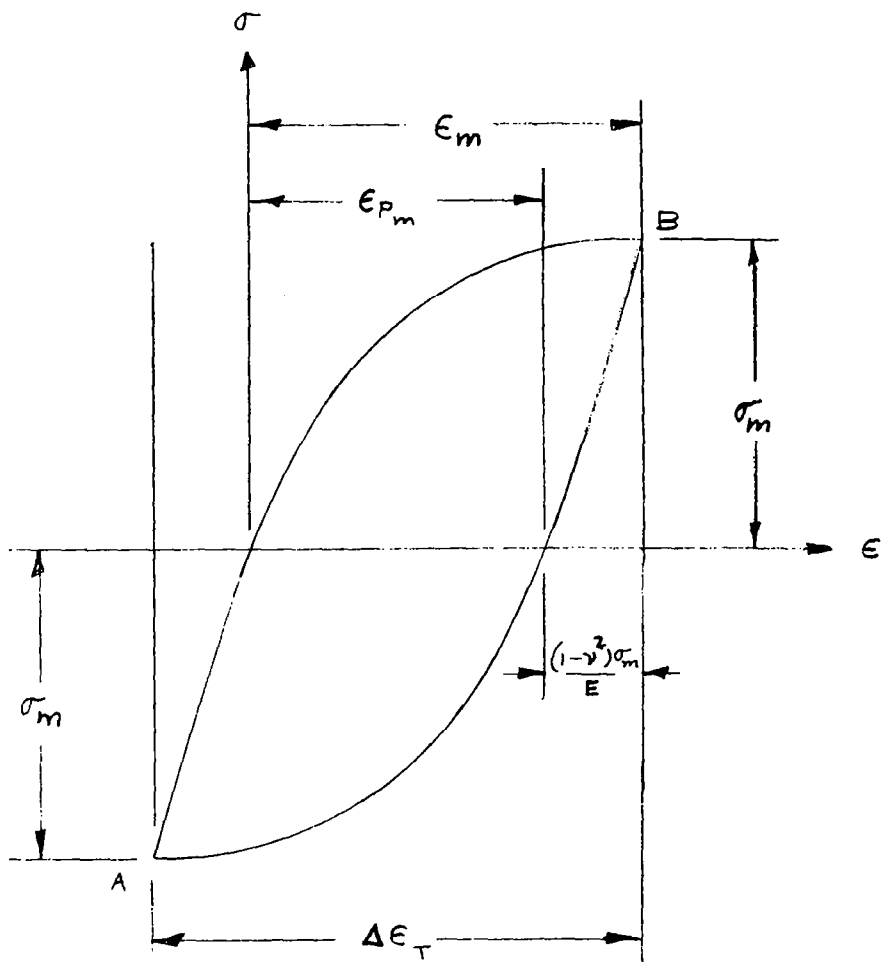
Figure 19. Relation of Hysteresis Loop to Loading Geometry

curve is assumed to be that of the virgin material and identical in tension and com-
pression.* Thus, the size of the hysteresis loop depends only on the total strain range.
Similar loops will be established for different longitudinal fibers located at various dis-
tances from the neutral axis (mid-surface) of the tube wall. The strain energy per unit
length of tube for one material cycle (i.e., one-half revolution of the tube), W_p, is
the integral of the loops for each fiber, w_p, over the volume V of tube material:

$$W_p = \int w_p \, dV \ .$$

(89)

For identical stress-strain behavior in tension and compression,

$$w_p = 2 \int_0^{\epsilon_{pm}} \sigma \, d\epsilon_p \ ,$$

(90)

where ϵ_{pm} is the maximum plastic strain for the particular fiber (See Figure 19). For
many ductile metals in plane strain bending, the stress-strain relation can be approxi-
mated in the form**

$$\epsilon = (1-\nu^2) \frac{\sigma}{E} + \epsilon_{PL} \left(\frac{\sigma}{\sigma_{PL}} \right)^n \ ,$$

(91)

where ϵ_{PL} is the "plastic" strain at the proportional limit, σ_{PL} is the proportional
limit stress, and n is a material constant. The first term on the right is the elastic strain
and the second term is the plastic component. Substitution of Equation (91) in Equation
(90) and integration yields

$$w_p = \frac{2n}{n+1} \sigma_{PL} \, \epsilon_{PL} \left(\frac{\sigma_m}{\sigma_{PL}} \right)^{n+1} \ .$$

(92)

---

* This corresponds to zero strain hardening and, hence, a very pronounced Bauschinger
  effect (See, for example, Reference 17, Ch. 12).

** See Reference 17, Ch. 9.

58

With Equation (92) and $dV = 4\pi h\, dy$ Equation (89) may be written,

$$W_p = \frac{8\pi h}{n+1} h\, \sigma_{PL}\, \epsilon_{PL} \int_0^{h/2} \left(\frac{\sigma_m}{\sigma_{PL}}\right)^{n+1} dy \; , \tag{93}$$

where y is the distance from the neutral axis. The total strain range $\Delta\epsilon_T$ varies linearly with y, according to the relation

$$\Delta\epsilon_T = \frac{y}{h/2}\, \Delta\epsilon_{Tm} \; , \tag{94}$$

where $\Delta\epsilon_{Tm}$ is the total strain range for the outermost fibers. Also, from Equation (91) and Figure 19,

$$\Delta\epsilon_T = \epsilon_m + (1-\nu^2)\frac{\sigma_m}{E} = 2(1-\nu^2)\frac{\sigma_m}{E} + \epsilon_{PL}\left(\frac{\sigma_m}{\sigma_{PL}}\right)^n \; . \tag{95}$$

For a given value of $\Delta\epsilon_{Tm}$ as determined from the previous curved beam analysis, the corresponding stress σ_{mm}, which also corresponds to the value $y = h/2$, can be determined from Equation (95). By selecting several values of σ_m between zero and σ_{mm}, the corresponding values of $\Delta\epsilon_T$ and y can be determined and W_p can then be determined from Equation (93) by numerical integration.

For a simple device, as illustrated in Figure 4b, the driving force per unit length of tube, f, is determined by equating the work in one revolution of the tube* $4\pi h f$ to the cyclic strain energy $2W_p$ to give,

$$f = \frac{W_p}{2\pi h} \; . \tag{96}$$

2. Design Relations for a Stainless Steel Tube

A numerical example of the foregoing method was carried out for

_____

* The stroke of the device for one revolution of the tube is twice the circumference.

a 302 stainless steel tube. The material constants were selected as follows:

$$E = 28 \times 10^{6} \text{ psi} \qquad \epsilon_{PL} = 20 \times 10^{-6}$$

$$\nu = 0.3 \qquad n = 5.5$$

$$\sigma_{PL} = 22,400 \text{ psi}$$

For the plastic curved beam analysis an experimental moment-curvature relation for 0.012 inch stainless steel sheet (Reference 32) was used. This curve is shown in Figure 20, plotted in non-dimensional form.

In order to solve for the moment distributions corresponding to various loading conditions, Equations (81) and (82) were solved numerically using the results of Figure 20. From the moments at points A and B (Figure 19) the maximum bending strains were computed from Equation (88). The corresponding tube deflections were determined by the incremental technique using Equations (83) – (86). With the maximum bending strains and, hence, total strain ranges, the plastic strain energy per unit length of tube per cycle, W_p was computed from Equations (93) – (95), and the driving force relation was computed from Equation (96). Two cases of loading were computed from which it was possible to plot a set of design curves. These results are shown in Figure 21 in terms of load and deflection parameters plotted against plastic strain range $\Delta \epsilon_p$. From these curves, it is possible to determine the lateral compressive force f_c, the driving force f, and the radial deflection η vs $\Delta \epsilon_p$ for particular values of tube radius and thickness.

The two cases on which the design curves are based correspond to maximum plastic strain ranges of 0.25% and 0.68%. The distributions of cyclic strain energy (area under the hysteresis loop) over the tube wall for these two cases are shown in
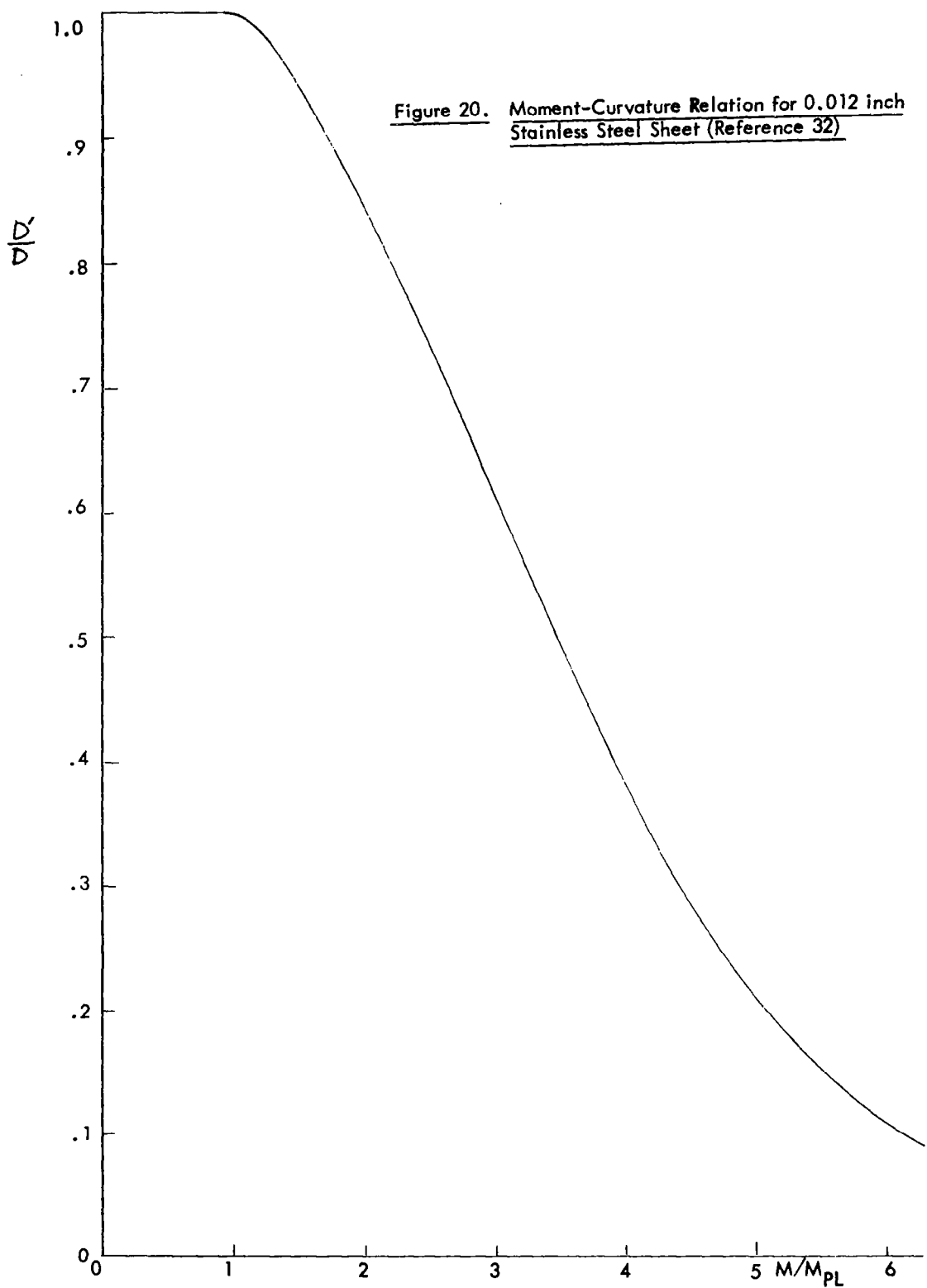
Figure 20. Moment-Curvature Relation for 0.012 inch Stainless Steel Sheet (Reference 32)

61

Figure 21. Design Curves for Rolling Tube Device

Material: 302 Stainless Steel
$E = 28 \times 10^6$ psi $\gamma = 0.3$ $n = 5.5$
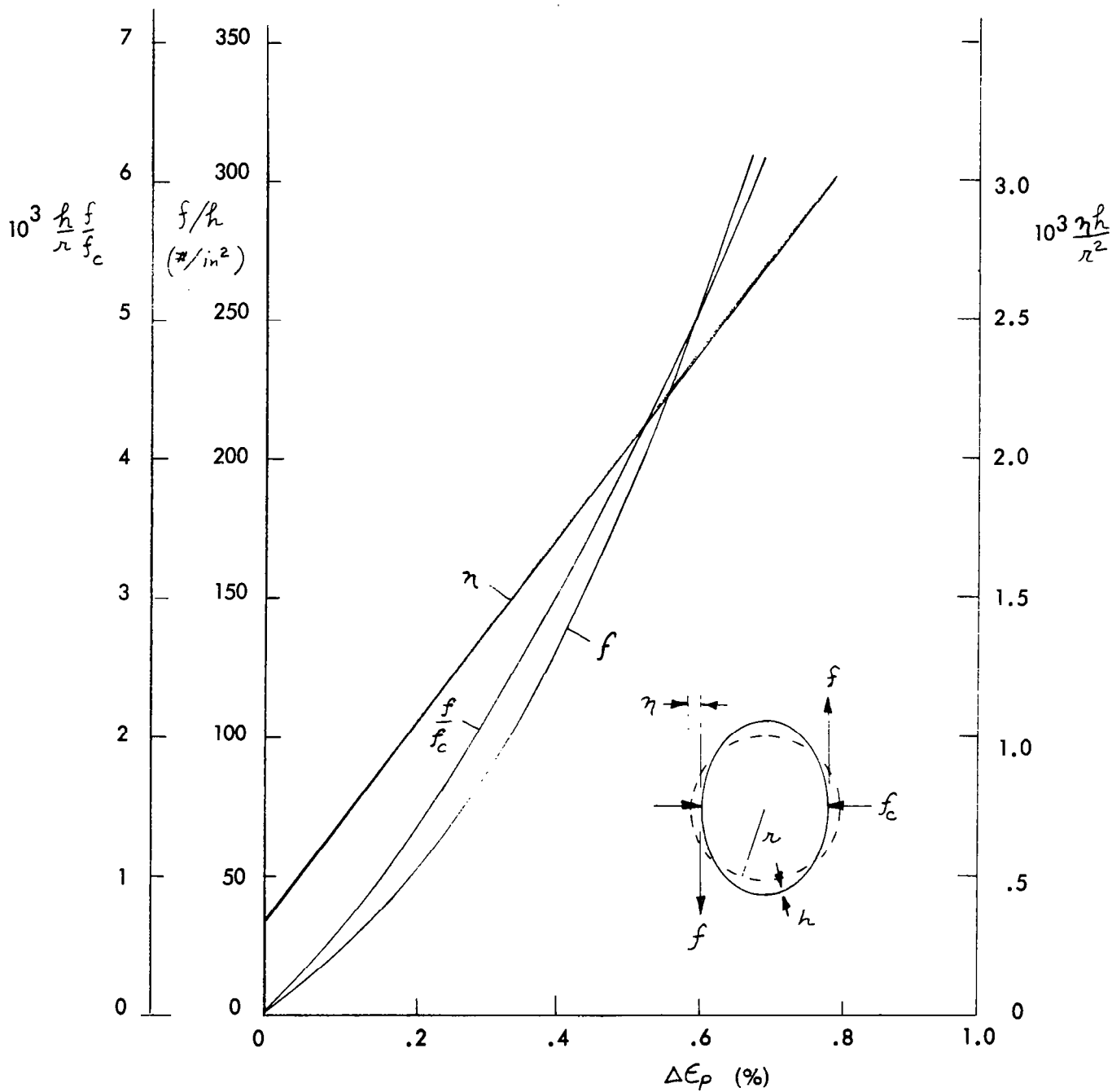$\epsilon_{PL} = 20 \times 10^6$ $\sigma_{PL} = 22,400$ psi

Figure 22. The area under these curves is a measure of the total cyclic strain energy and is proportional to the driving force f. It is interesting to note the extent to which the strain energy is concentrated in the outer fibers, particularly for the lower value of strain range.

VII   EXPERIMENTAL PROGRAM

An experimental investigation was conducted in three parts. The first part was concerned with the design and construction of a cyclic torsion test apparatus and testing of promising materials under conditions appropriate to cyclic strain energy devices. A major objective of this phase has been to determine flow and fatigue behavior of promising materials under conditions of rapid cyclic straining. Materials tested include 1100 aluminum, 347 stainless steel, molybdenum TZM, and nylon 66.

The second part of the program involved the design, construction, and testing of a torus impact device with friction drive. Aluminum and nylon working elements were utilized and both quasi-static and impact tests were performed. Correlations with theoretical predictions are shown.

The third part of the program involved the design, construction and testing of a rolling tube cyclic strain energy device utilizing stainless steel working elements. Quasi-static tests were performed and correlations with theoretical predictions are shown.

A.   Cyclic Torsion Tests

Two test apparatus designs were utilized. The first design, Test Apparatus 1, was intended to provide an angular twist up to 30 degrees at frequencies up to 100 cps.

Figure 22.   Distribution of ω_p Over Tube Wall

$\Delta\epsilon_p = .68\%$

$\Delta\epsilon_p = .25\%$

ω_p

$\left(\frac{in-lb}{in^3}\right)$

$\left(\frac{y}{h/2}\right)$
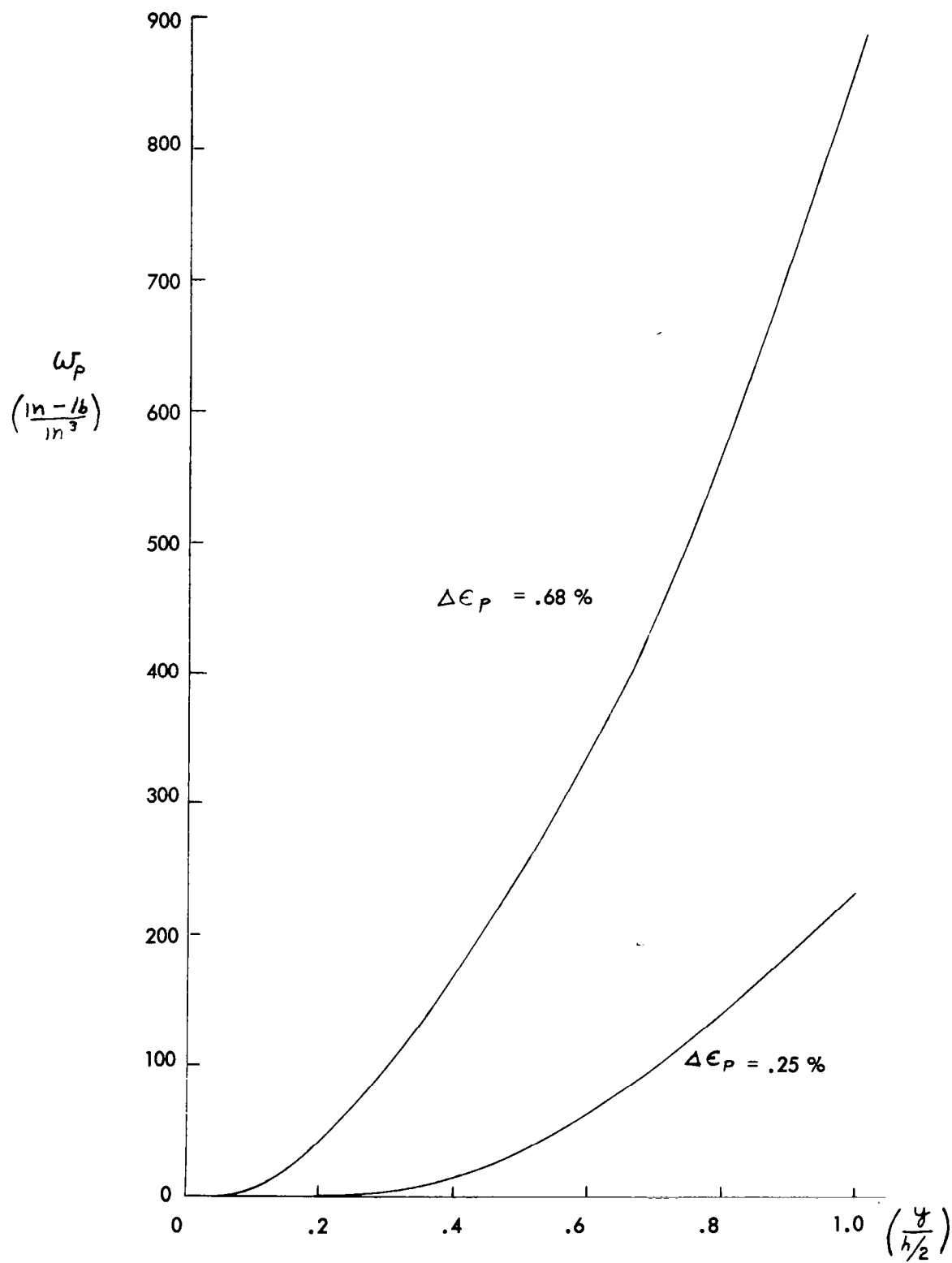
However, the useful frequency range was limited to about 33 cps due to resonances in the system. This apparatus was modified (Test Apparatus II) to reduce the resonance effects and improve read-out techniques. Descriptions of the apparatus, data reduction procedures, and test results are presented in the following sections.

1.   Test Apparatus I

The first apparatus used in this study is described schematically in Figure 23. Photos of the assembly (Figure 24) ready for use illustrate the mechanical-electrical layout of the mechanism. It is designed to apply cyclic torsion strains of known amplitude and frequency to rod-shaped test specimens. Measurements are made of the angle of twist to which the test specimen is subjected, the torque load transmitted by the specimen, and the number of cycles. The cyclic frequency is pre-set to the desired value and maintained constant during the test.

Certain parameters are build into the device and are not directly measured. The total strain range is set by the adjustment of a cam mechanism (8)* which drives a gear. This determines the total angular displacement applied to the moving end of the specimen (10). The cyclic rate is varied with respect to the motor drive rate by means of a pulley combination (6) between the clutch shaft and the cam shaft. The actual number of cycles from initial start to shutdown is predetermined by a pre-set subtraction counter (7); and this counter also measures the total complete cycles for each run.** A clutch control unit (2) connects the drive cam to the motor and the engagement is adjusted to control the acceleration forces.

---

*   Numbers refer to the designated component in Figure 23.
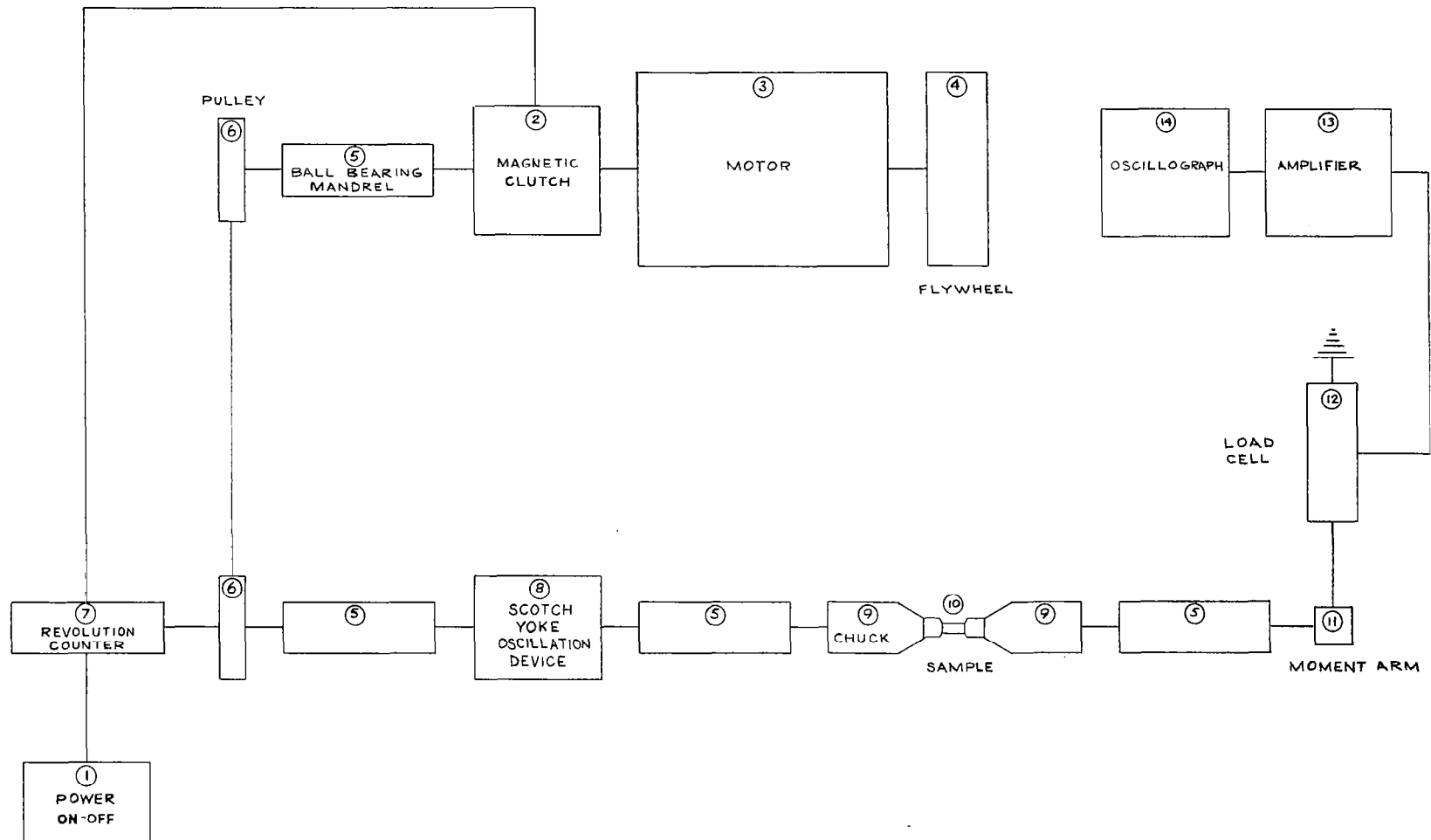** A certain overrun results from inertia in the system.

PULLEY

⑥

⑤
BALL BEARING
MANDREL

②
MAGNETIC
CLUTCH

③
MOTOR

④

FLYWHEEL

⑭
OSCILLOGRAPH

⑬
AMPLIFIER

⑫
LOAD
CELL

⑥

⑦
REVOLUTION
COUNTER

⑥

⑤

⑧
SCOTCH
YOKE
OSCILLATION
DEVICE

⑤

⑨
CHUCK

⑩

⑨

SAMPLE

⑤

⑪
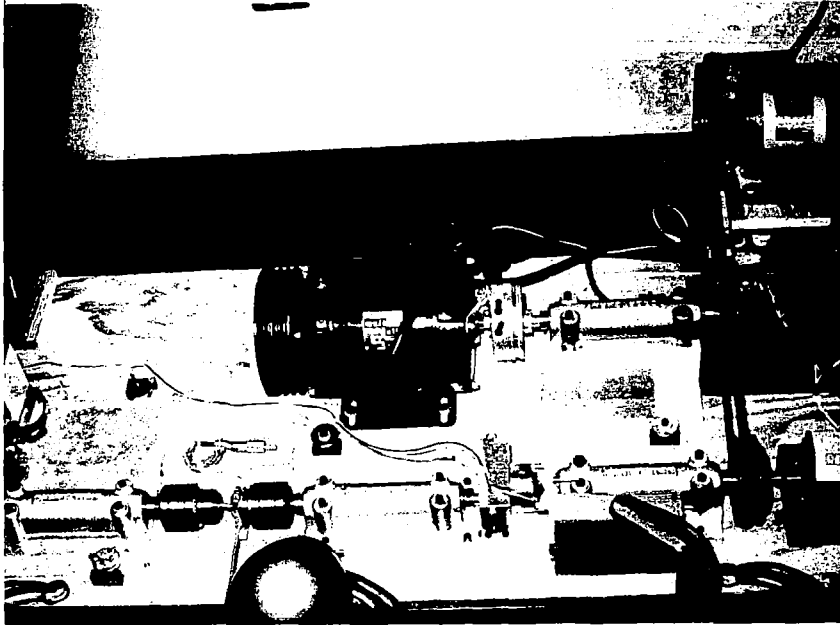MOMENT ARM

①
POWER
ON-OFF

FIGURE 23   SCHEMATIC, CYCLIC TORSION
TEST APPARATUS
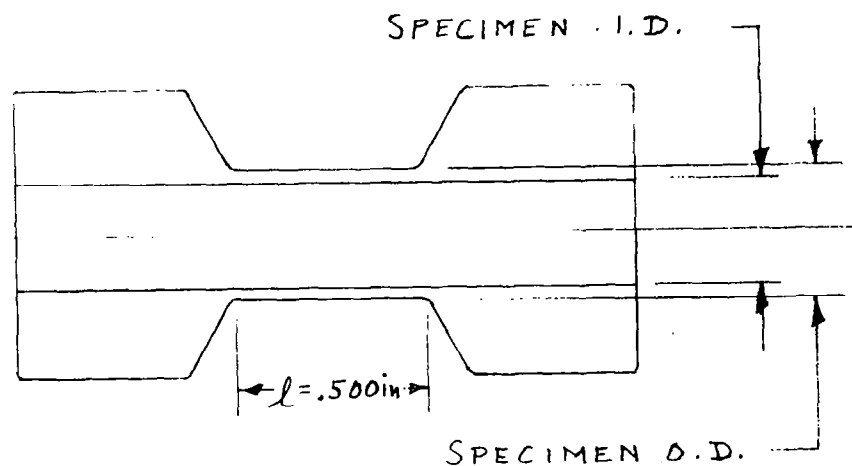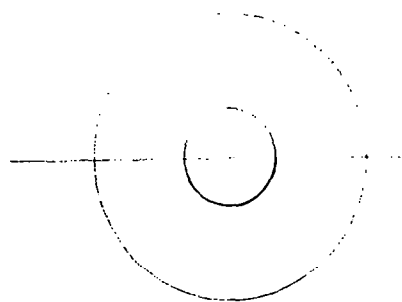
Figure 24

Cyclic Torsion Apparatus I – General Assembly
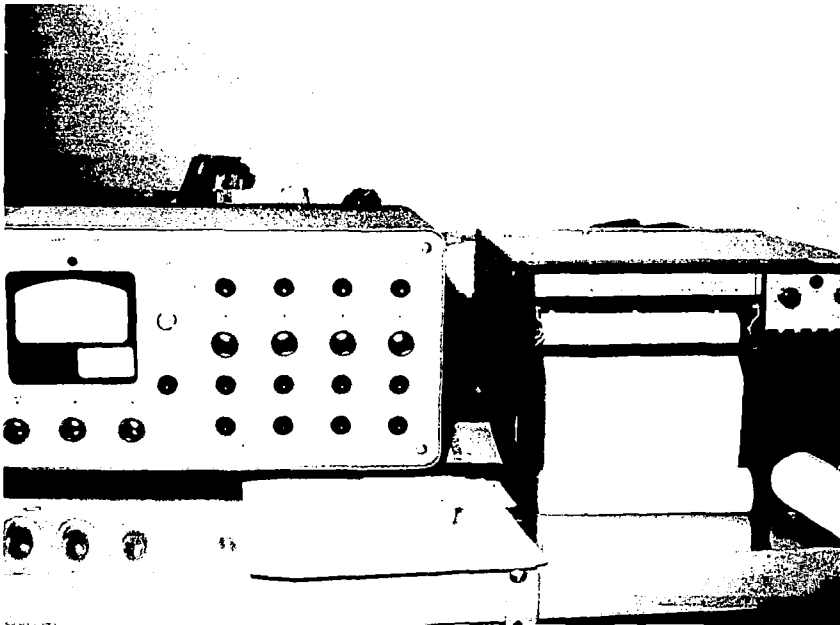
Amplifier and Oscillograph

An oscillograph recorder (14) and amplifier control unit (13) are used to record the torque history and the total number of cycles per run. The oscillograph record has a precision time-pulse record as part of each run. This record provides a time base for reduction of the recorded data. The stress history of each cycle is generated by a strain gage load cell (12) which measures the torque history of each cycle, the total cycles, and the cyclic rate for each run. A pulse generator installed on the cam shaft provides a record of the points of maximum angular twist. The device consists of a galvanometer connected to a current source and is activated by a switch with rotation of the cam shaft.

The apparatus was designed to provide an angular twist up to 30 degrees at frequencies up to 100 cps. The corresponding strain range depends on the specimen dimensions. Typical metal and nylon test specimens, shown in Figure 25, were capable of 12 and 24 percent maximum strain range, respectively.

A calibration of the system was performed to provide reference data for the actual specimen tests. The tranducer output versus plus-and-minus torque was calibrated by means of level beam and dead weights (Figure 26). In addition to the output calibration, a deflection-versus-torque calibration of the system was performed in order to determine the elastic deformation of the system and the resulting strain amplitude applied to the specimen.

SPECIMEN ·I.D.

SPECIMEN O.D.

$\ell = .500 \text{in}$

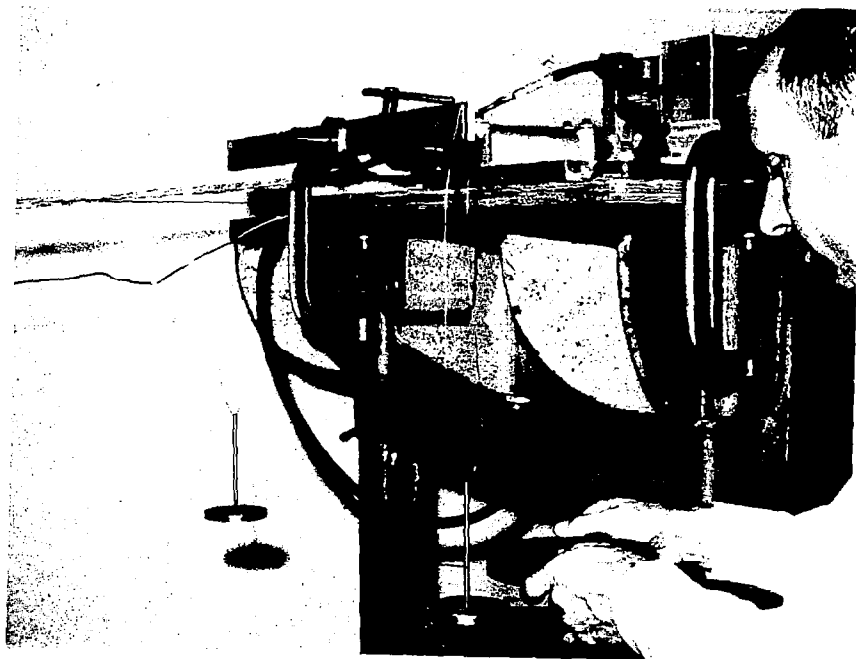| DIMENSION	METALS	NYLON
I.D.	.1875 in	.375 in
O.D.	.2275 in	.500 in

Figure 25. Test Specimens

Figure 26.　Dead Weight Calibration of Apparatus I

2. Test Apparatus II

Some limited data was obtained with the previous apparatus at the lower frequency ranges. However, pronounced resonance in the system occurred due to extensive mass and compliance of the drive shafts, the load cell, and connecting members. Consequently, the apparatus was redesigned to increase the resonant frequencies and to improve recording techniques.

At the load-cell end the moving masses were largely eliminated and the stiffness was significantly increased by redesign of the attachments and the load transducer. Mechanical backlash was eliminated from the transducer attachment.

At the drive end the shafts were stiffened, the drive line was shortened, attachment masses were reduced, and an electrical strain indicator circuit was added which measures directly the angular displacement of the specimen. This modification was made to permit simultaneous recording of torque and angular deflection, from which the stress-strain curves could be computed more simply.

Pictures of the modified apparatus are shown in Figures 27 and 28. Figure 27 is a general layout of the assembly. Figure 28 is a close-up of the attachment arrangement which shows the strain indicator and transducer.

3. Test Procedure - Apparatus I

A pre-selected angular twist was set for each test by means of a pointer tracked by a telescope attached to a height gage (Figure 29). Each specimen was installed at zero torque and then one cycle of strain was hand-cranked while measuring the strain amplitude and maximum torque output. The sample was then cycled approximately 20 times for records and visual observation. Cycling was continued to failure and the total number of cycles was recorded. Oscillograph records were made
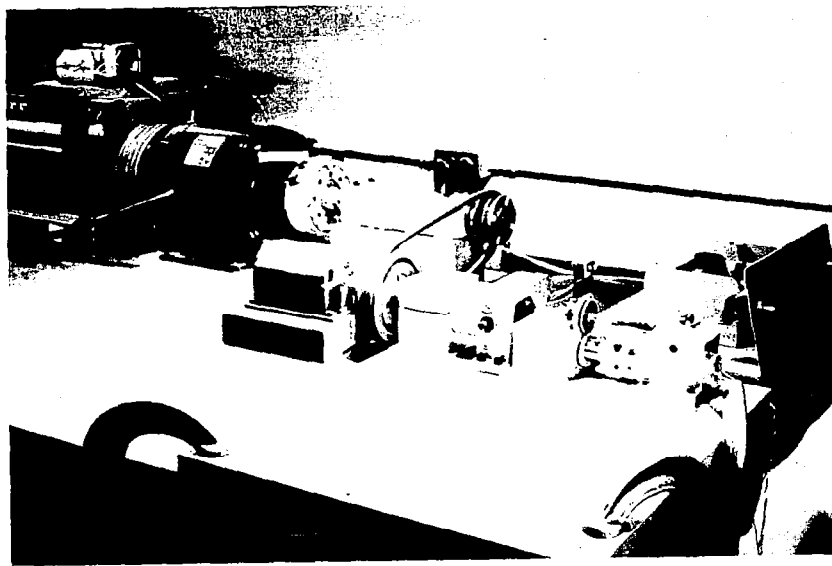
71

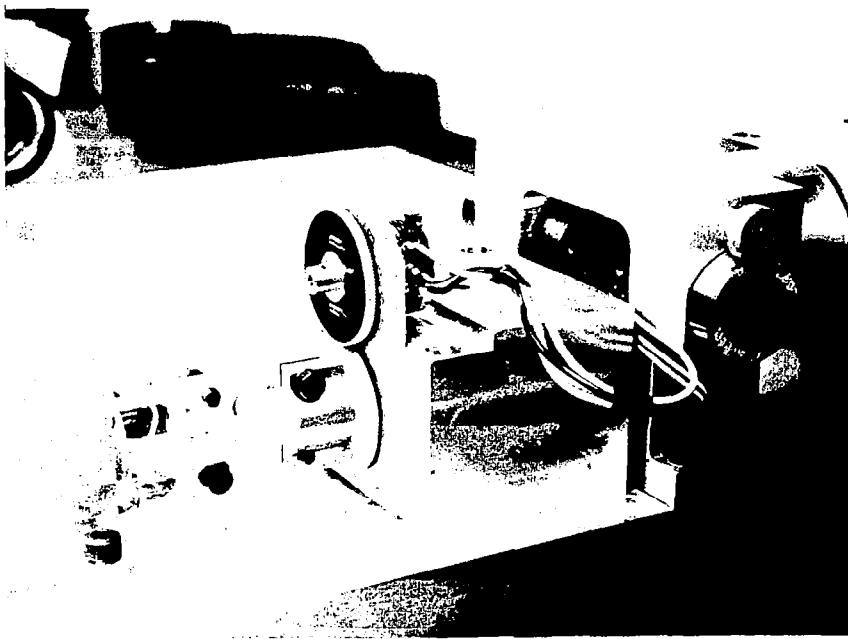Figure 27. Cyclic Torsion Apparatus II – General Layout
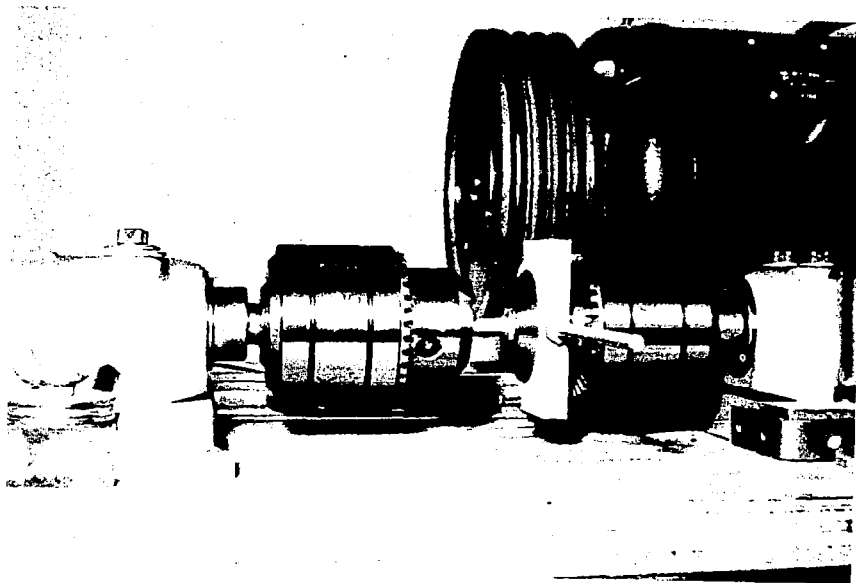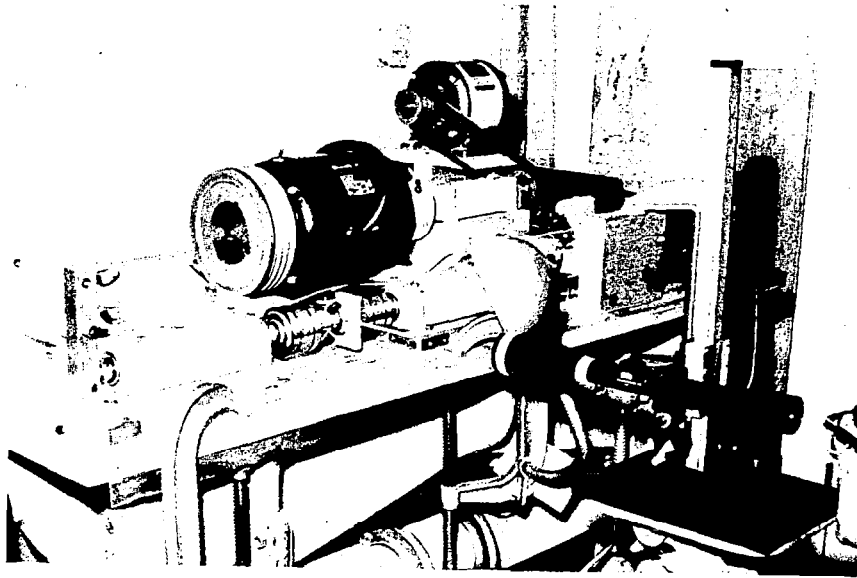
Figure 28. Cyclic Torsion Apparatus II - CloseUp.

Figure 29. Apparatus I – Measuring Telescope and Deflection Pointer

74

of the initial 20 cycles and periodically during the run to failure. A time pulse built

into the oscillograph record provides an accurate time base to measure cyclic rate.

4. Test Procedure – Apparatus II

The basic test procedure was similar to that previously described. With

the modified apparatus, strain amplitude was set directly from the displacement of the

rack. Exploratory runs were made with 347 stainless steel, 1100 aluminum, and Nylon 66,

but no regular test pattern was followed. All of the runs were at 100 cps where a sig-

nificant temperature rise resulted. Consequently, the number of cycles in a run was

limited so as to limit the maximum temperature rise. Temperature was measured with the

aid of a thermocouple thermometer held in contact with the test specimen.

5. Data Reduction Procedure – Apparatus I

a. Metals

The basic procedure for constructing a stress-strain curve

consists of eliminating the time variable from the load-time record and the approximate

sinusoidal strain input. A typical load-time record is shown in Figure 30. The period

and relative phase of the strain curve are established with the aid of the time pulses on

the oscillograph records, described above. Corrections must be applied to the sinusoidal

input at the cam in order to account for the elastic deflections in the system. This is

accomplished with the aid of the static torque-deflection calibration curves. For each

value of torque read off the load-time record, the corresponding deflection of the system

is subtracted from the sinusoidal input to give the true deflection of the specimen.

The detailed procedure is explained more readily with

the aid of Figure 31. Points of maximum stress and strain, A and A', are located on the
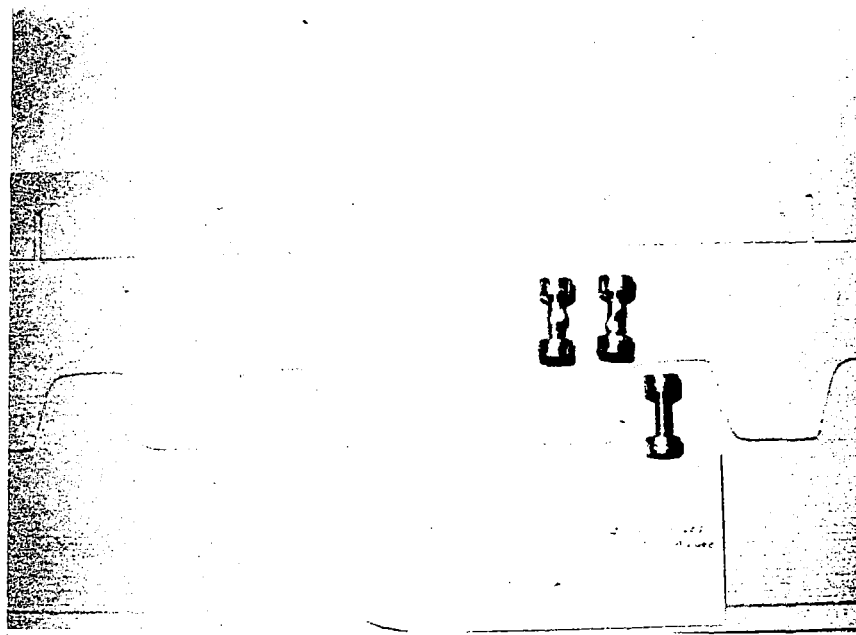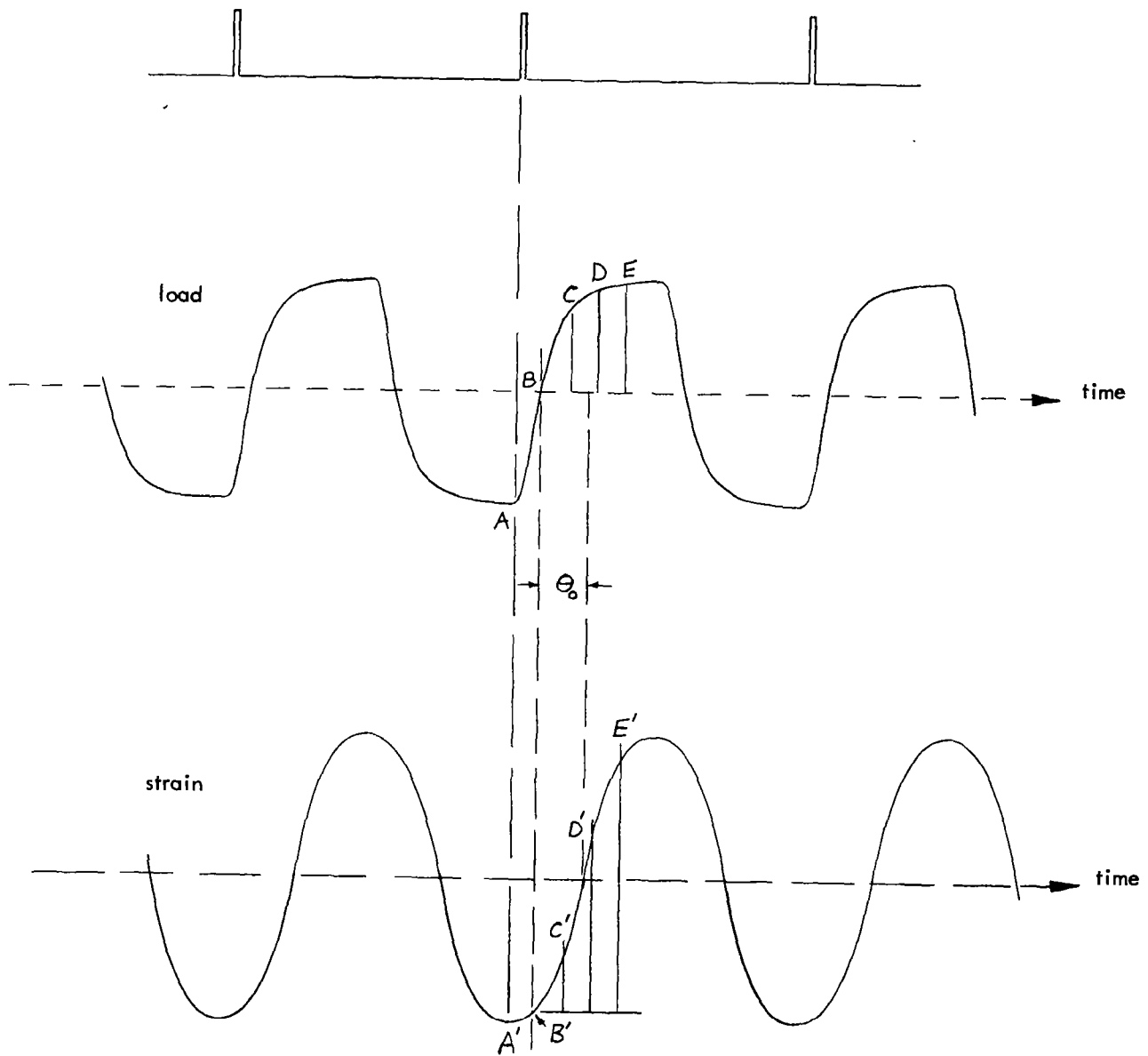
Figure 30. Typical Oscillograph Record and Aluminum Specimens

Figure 31. Load-Time and Strain-Time Curves

77

load-time and strain-time curves, respectively. Points B and B' indicate the point of zero load and, hence, the start of the stress-strain curve. Subsequent increments of time represented by points C-C', D-D', and E-E', are selected. The torques are read off the load cell calibration curve, and the corresponding strains are determined from the sinusoidal strain curve, as indicated in the figure, with the amplitude determined from the cam input. Corrections for deformations in the system are read from the calibration curves using the appropriate torque values and are subtracted from the sinusoidal strains to give the actual strains. From the dimensions of the thin-walled test specimen, torque is converted to stress and the stress-strain curve is thereby determined.

For the preliminary runs, values of the phase angle θ_o between the load time and strain time curves (Figure 31) were established with the aid of the pulses on the load record designating points of maximum twist. The stress-strain curves computed on this basis, however, gave rise to incorrect initial slopes or elastic shear moduli. It was subsequently found that small changes in the phase relation produced large changes in the curve shapes. Consequently, the phase angle θ_o was determined in such a manner that the initial slope was equal to the elastic shear modulus. This procedure is as follows: Denoting the angular coordinate measured from points B or B' by θ (Figure 31), the shear strain relation $\gamma(\theta)$ is given by

$$\gamma(\theta) = \frac{\Delta \gamma_T}{2} \sin(\theta - \theta_o) - \frac{\tau(\theta)}{G_A} \quad , \tag{97}$$

where τ is the shear stress, $\Delta \gamma_T$ is the total strain range set at the cam, and G_A is the spring constant for the apparatus. With this relation the initial slope of the stress-strain curve can be expressed by

$$\left(\frac{d\tau}{d\gamma}\right)_{\theta=0} = G = \left(\frac{d\tau}{d\theta}\right)_{\theta=0}\left(\frac{d\theta}{d\gamma}\right)_{\theta=0} = \frac{\left(\frac{d\tau}{d\theta}\right)_{\theta=0}}{\frac{\Delta\gamma_T}{2}\cos\theta_0 - \frac{1}{G_A}\left(\frac{d\tau}{d\theta}\right)_{\theta=0}}, (98)$$

where $\left(\frac{d\tau}{d\theta}\right)_{\theta=0}$ is computed from the initial slope of the load-time record. Solving for θ_0 from Equation (98),

$$\theta_0 = \cos^{-1}\left[\frac{\left(\frac{1}{G} + \frac{1}{G_A}\right)}{\frac{\Delta\gamma_T}{2}}\left(\frac{d\tau}{d\theta}\right)_{\theta=0}\right]. \qquad (99)$$

Thus, θ_0 can be determined from the shear modulus, G, and the initial slope of the load-time record for known values of $\Delta\gamma_T$ and G_A.

It is expected that errors in the time pulse were due to a difficulty in setting the limit switch accurately as well as to peculiar elastic distortions in the system at points of maximum twist, particularly for the higher loads and frequencies. These latter effects were evident in the unloading portion of the computed preliminary stress-strain curves. Consequently, the curves were recomputed only up to maximum stress and the unloading portions were constructed from the shear moduli of the materials.

b.   Nonmetals

If the load-time output is sinusoidal, the stress-strain behavior can be determined in terms of the viscoelastic properties described in Section VB. It is necessary, however, to correct for the elastic deformations of the apparatus, as with the metals.

The complex shear modulus for the system (specimen and apparatus), $G^{*\prime} = G_1' + iG_2'$, is computed from the relative amplitude $|G^{*\prime}|$ and phase lag θ' between strain input and stress output. The system is regarded as a Maxwell model

(Hookean spring in series with a Newtonian dashpot) in which the spring consists of the apparatus (G_A) in series eith the elastic element (G) of the specimen (Figure 32). The element parameters are related to the dynamic properties of the system by the following equations:

$$G' = G_2' \left(\frac{\tan^2 \Theta' + 1}{\tan \Theta'} \right) \qquad , \tag{100}$$

$$\eta = \frac{G'}{\omega \tan \Theta'} \qquad , \tag{101}$$

and

$$\frac{1}{G'} = \frac{1}{G_A} + \frac{1}{G} \qquad . \tag{102}$$

Thus, from a knowledge of G_2', Θ', and G_A, the quantities G and η are computed with the aid of Equations (100) – (102). The complex shear modulus for the test specimen, $G^* = G_1 + iG_2$, is computed from the same relations,

$$\tan \theta = \frac{G}{\omega \eta} \qquad , \tag{103}$$
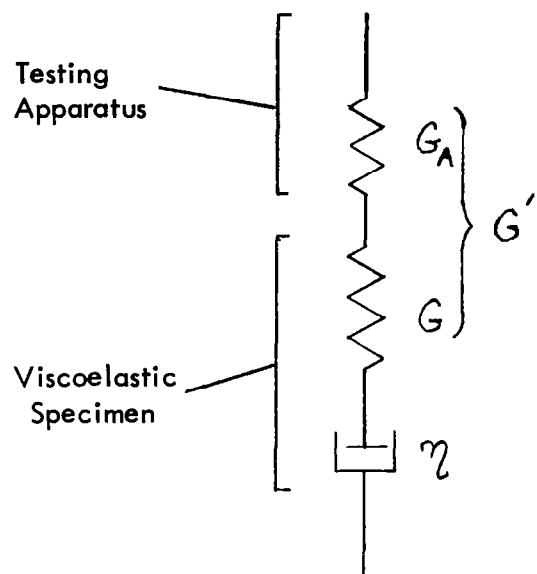
$$G_2 = \frac{G \tan \theta}{\tan^2 \theta + 1} \qquad , \tag{104}$$

$$G_1 = \frac{G_2}{\tan \theta} \qquad , \tag{105}$$

and

$$|G^*| = \sqrt{G_1^2 + G_2^2} \qquad . \tag{106}$$

The true maximum strain amplitude in the test specimen, γ_{max}, and the specific energy absorption per cycle are then computed from:

Testing Apparatus

Viscoelastic Specimen

G_A

G'

G

η

$$\left(\frac{1}{G'} = \frac{1}{G_A} + \frac{1}{G} \right)$$

Figure 32. Viscoelastic Model for Reducing Cyclic Torsion Data

$$\gamma_{max} = \frac{\tilde{\tau}_{max}}{|G^*|} \quad , \qquad\qquad (107)$$

and

$$W_p = \pi \, G_2 \, \gamma_{max}^2 \quad . \qquad\qquad (108)$$

It should be noted that the viscoelastic parameters determined by the foregoing procedure need not be linear, nor independent of frequency. The viscoelastic model can be considered as a simple Maxwell model whose parameters vary, in general, with frequency ans strain range.

6. Test Results

a. Metals

Results of the cyclic torsion tests with Apparatus I are shown in Figures 33 to 41. Figures 33 to 38 show stress-strain curves for the three metals tested at 1.5 and 17 cps. The curves represent typical hysteresis loops shortly after the material has "stabilized." Only one-half of each hysteresis loop was computed due to the similarity in the test data for the other half. These figures indicate the effects of strain range and frequency on maximum stress range. The aluminum and the 1.5-cps molybdenum data indicate a consistent and uniform increase in the hysteresis loops with increasing strain range. This was not the case with the stainless steel and the 17-cps molybdenum data, apparently because of a significant temperature rise and softening with cycling. Consequently, the relative size and shape of these hysteresis loops depends largely on which cycles are selected for comparison. Figure 39 shows the decrease in
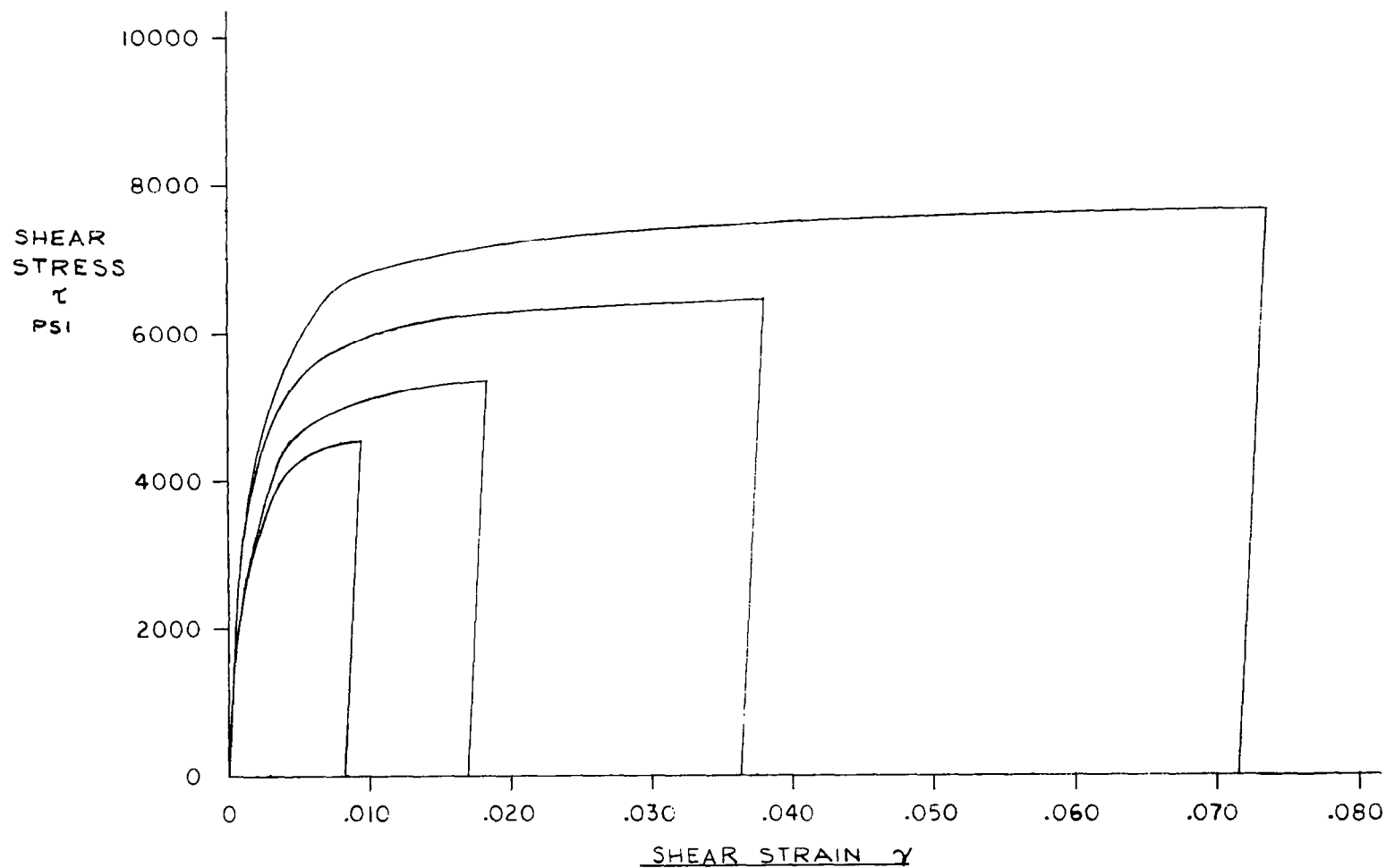
FIGURE 33

STRESS-STRAIN CURVES FOR 1100-0 ALUMINUM FROM CYCLIC TORSION TESTS AT 1.5 CPS

83

SHEAR
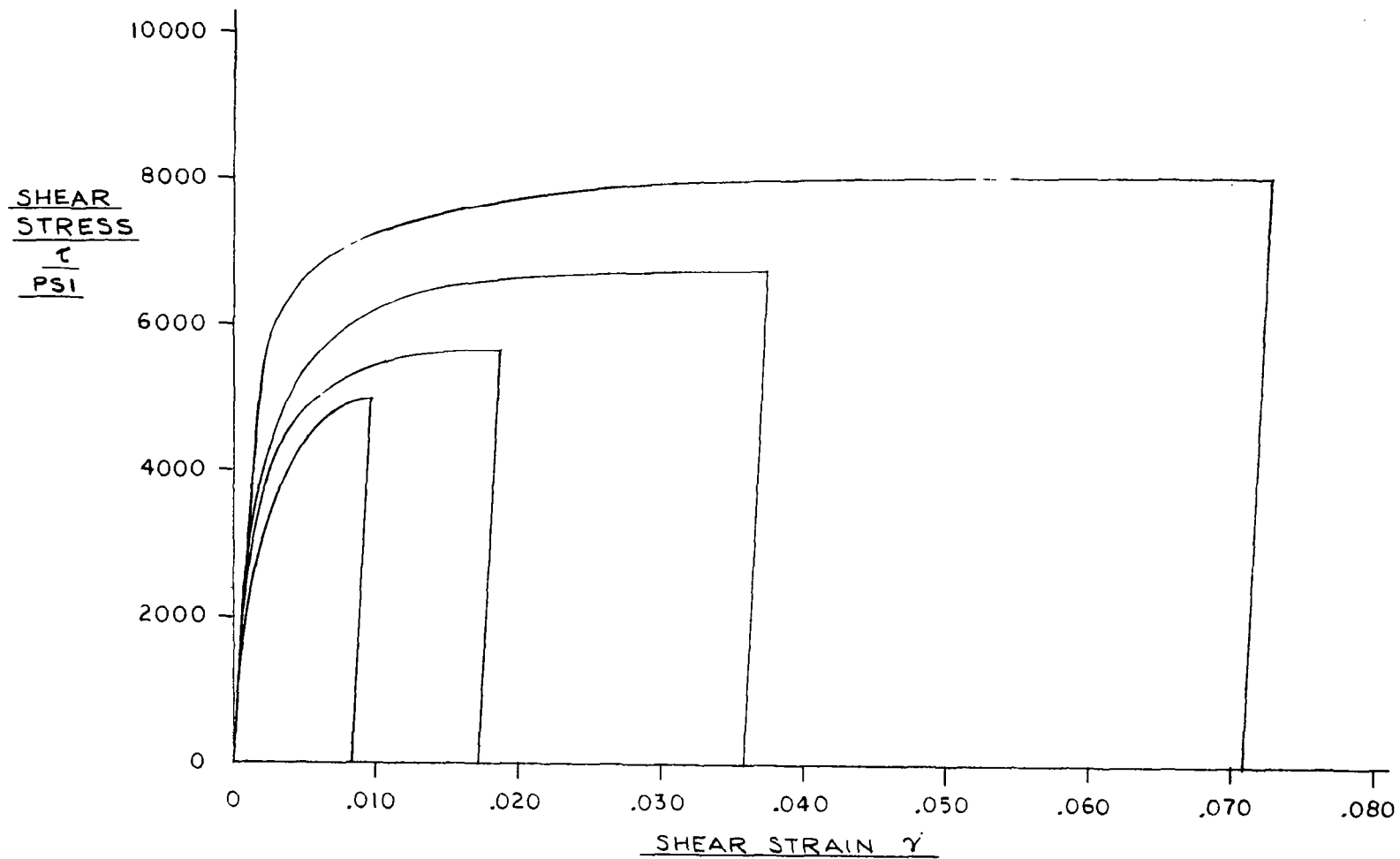STRESS
τ
PSI

SHEAR STRAIN γ

FIGURE 34

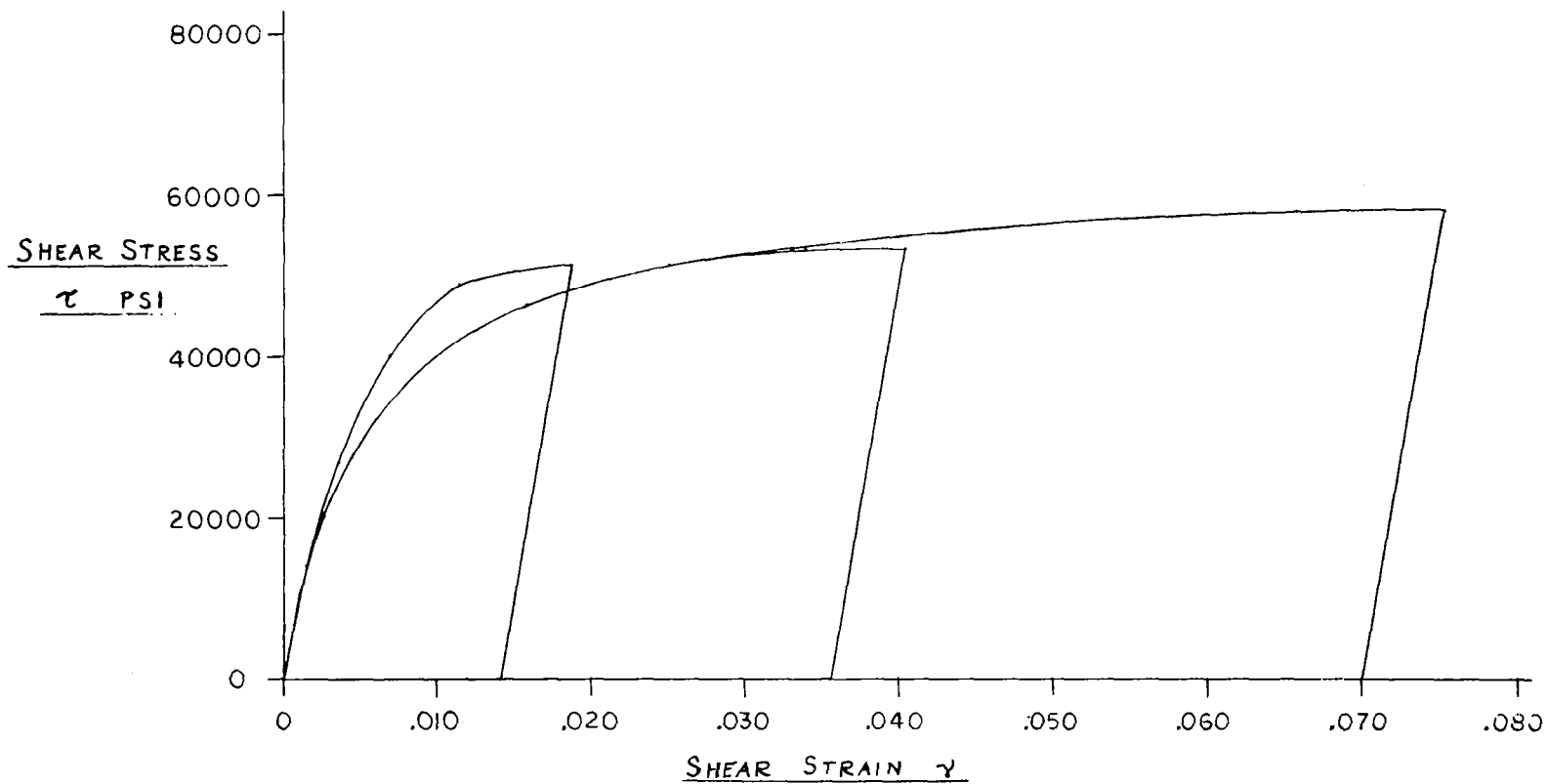STRESS-STRAIN CURVES FOR 1100-0 ALUMINUM FROM CYCLIC TORSION TESTS AT 17 CPS

FIGURE 35

STRESS-STRAIN CURVES FOR TYPE 347 STAINLESS STEEL FROM CYCLIC TORSION TESTS AT 1.5 CPS
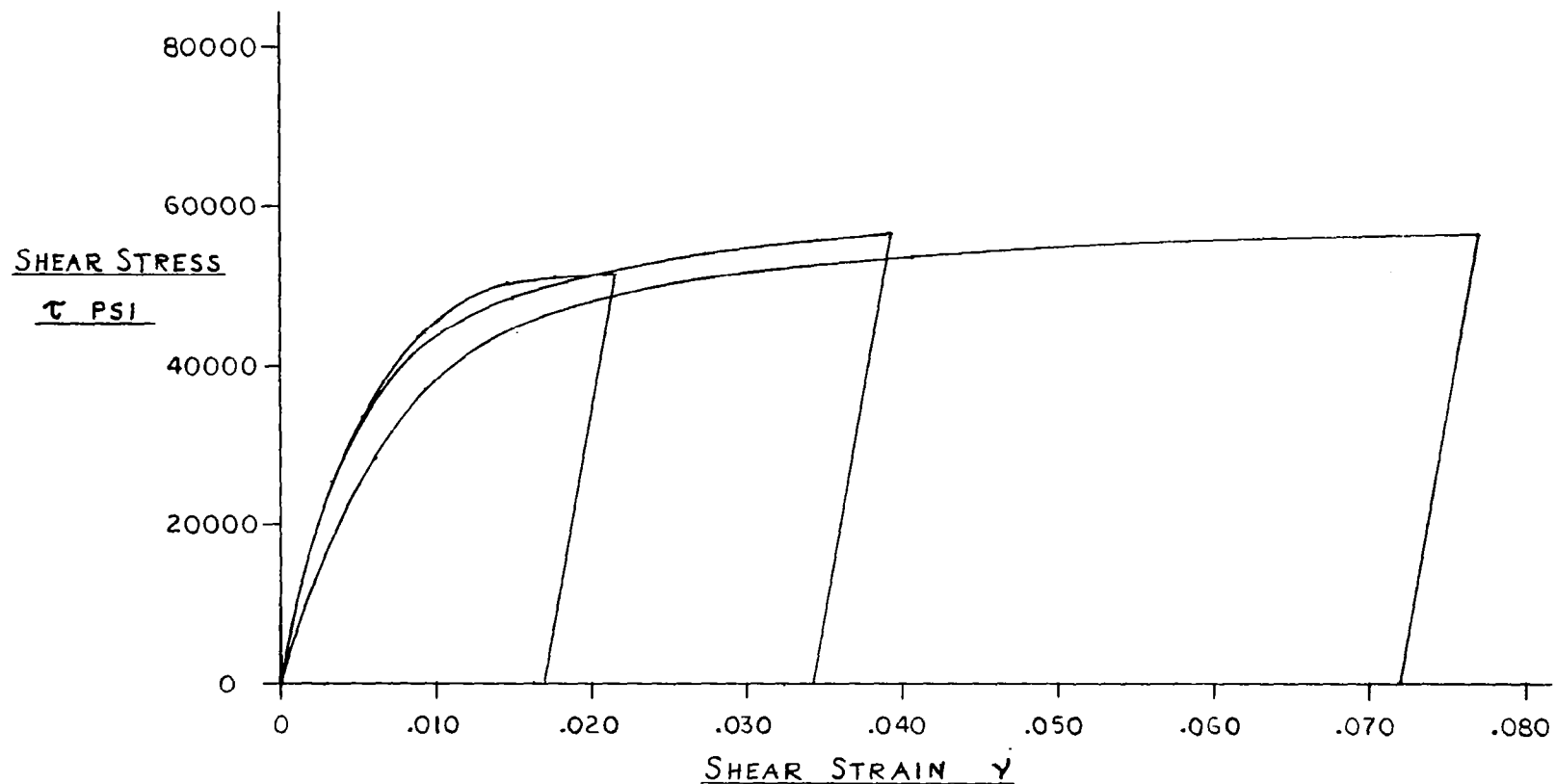
FIGURE 36

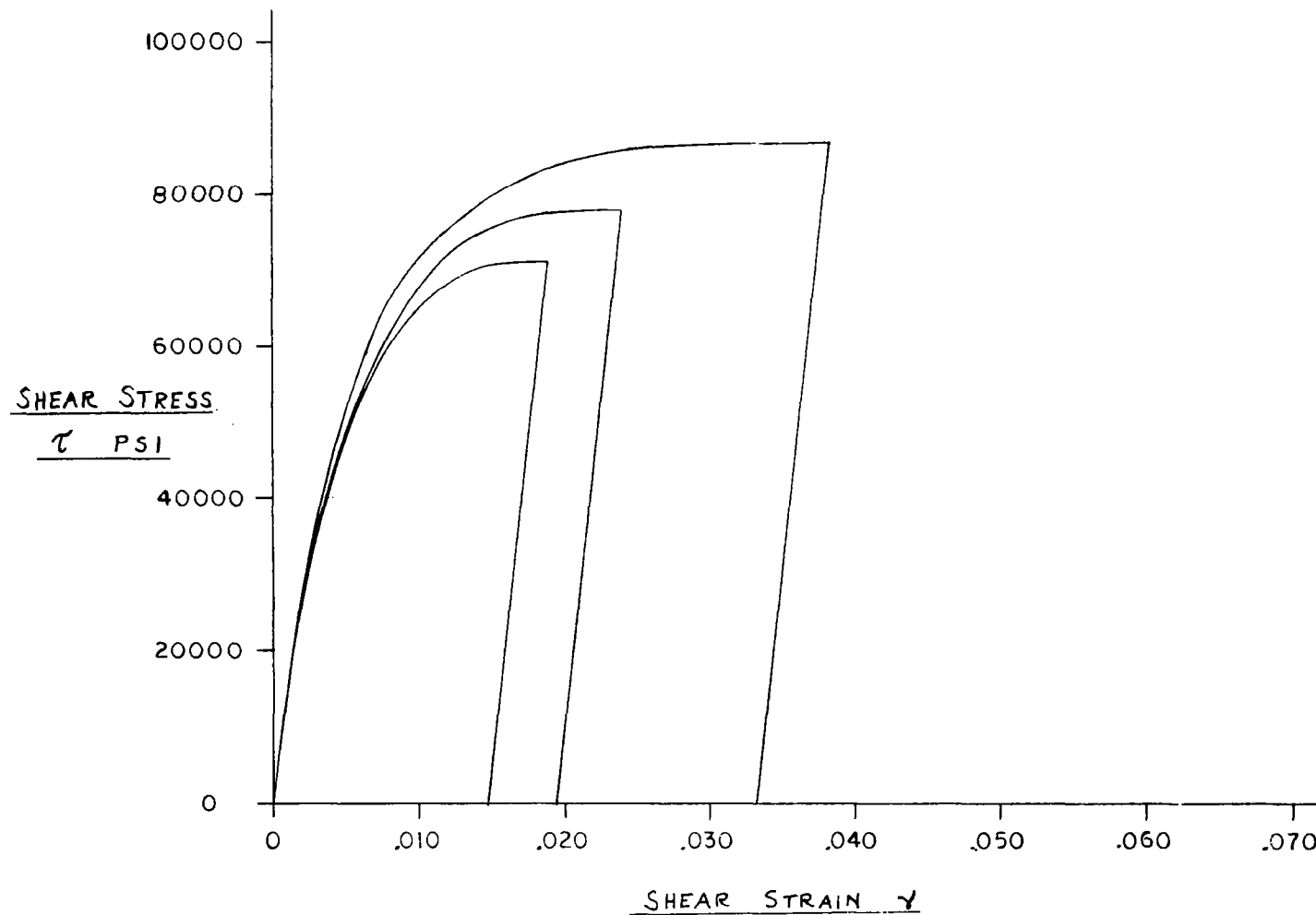STRESS-STRAIN CURVES FOR TYPE 347 STAINLESS STEEL FROM CYCLIC TORSION TESTS AT 17 CPS

SHEAR STRESS
τ PSI

SHEAR STRAIN γ

FIGURE 37

STRESS-STRAIN CURVES FOR MOLYBDENUM TZM FROM CYCLIC TORSION TESTS AT 1.5 CPS
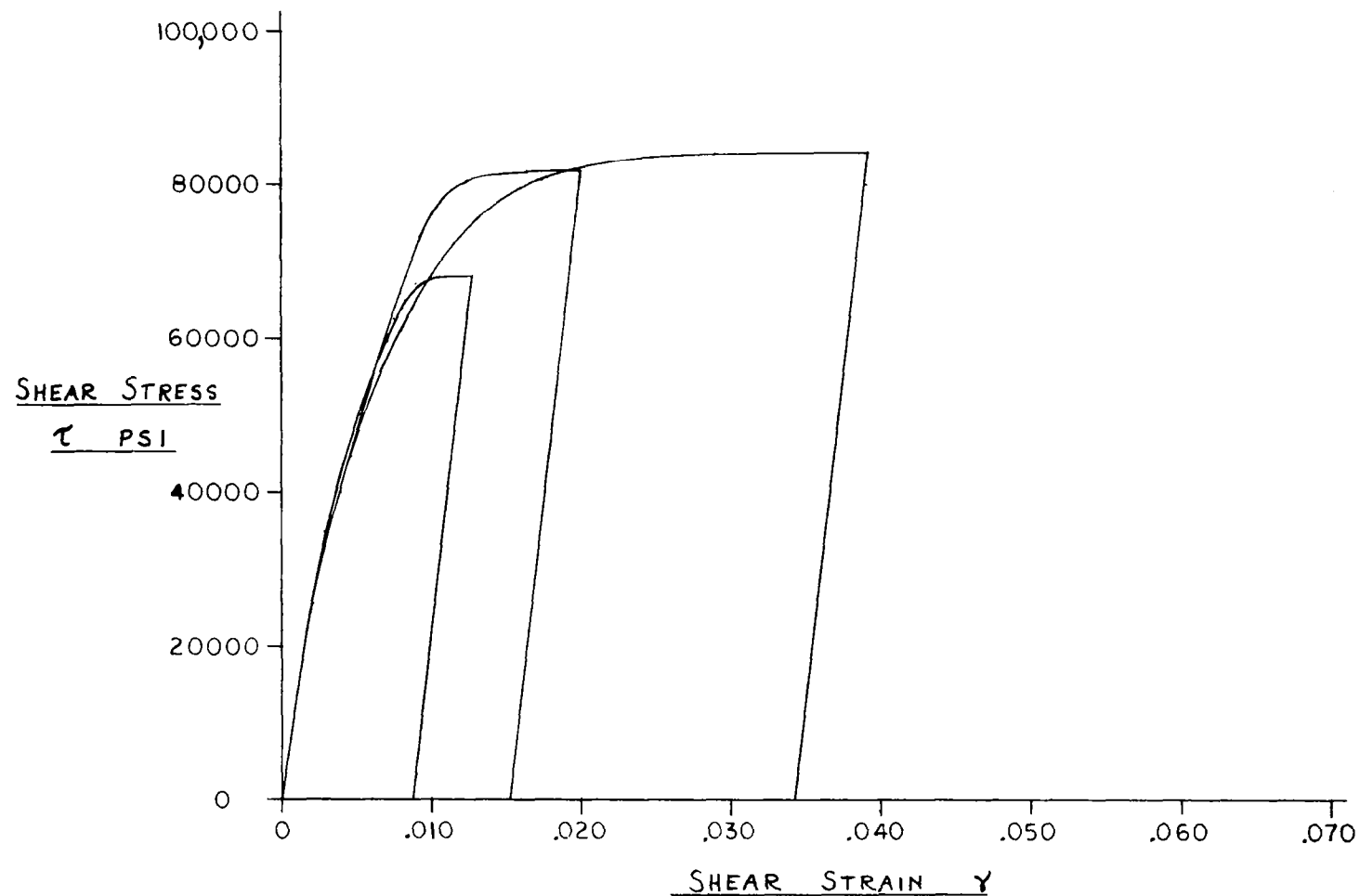
87

FIGURE 38

STRESS-STRAIN CURVES FOR MOLYBDENUM TZM FROM CYCLIC TORSION TESTS AT 17 CPS
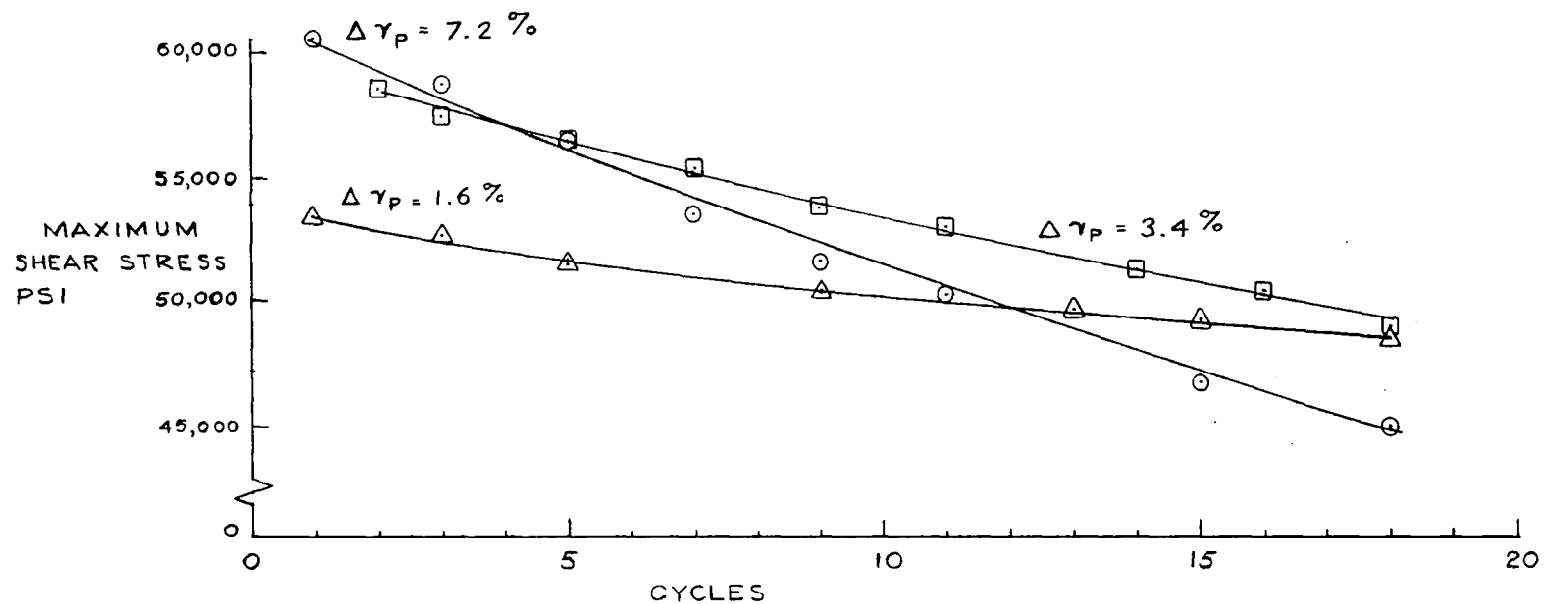
FIGURE 39   MAXIMUM SHEAR STRESS VS NUMBER OF CYCLES
FOR 347 STAINLESS STEEL AT 17 CPS.

maximum stress with number of cycles for the 17-cps stainless steel data. The rate of decrease in stress, as would be expected, increases with increasing strain range and, hence, increasing heat generation. Similar results are shown later for stainless steel and nylon data obtained at 100 cps with Apparatus II.

The aluminum and the 1.5-cps molybdenum data are replotted in Figures 40 and 41 to show more clearly the strain range and rate effects. In these curves stress is plotted against total strain, measured from the point of zero stress, so the results can be compared with the virgin stress-strain curves. These "cyclic" stress-strain curves are basic properties of the metal, as discussed in Section V A.

Some limited testing of 347 stainless steel and 1100 aluminum was carried out at 100 cps with Apparatus II. The number of cycles per burst was limited to control the temperature rise. These results are presented in Figures 42 to 44, which show maximum flow stress vs number of cycles. Figures 42 and 43 show results for hard and annealed aluminum, respectively, at 1.5 % strain range, and Figure 44 shows annealed stainless steel at 1.3 % strain range. The runs with the aluminum were limited to about 600 cycles which produced a maximum of about 22°F temperature rise. By comparison, runs of 200 cycles with the stainless steel produced a maximum temperature rise of about 110°F.

A marked difference is apparent in the cyclic flow behavior between the hard and soft aluminum. The softening of the hard material is consistent with similar behavior for other metals at lower frequencies (Sec. V A). However, it is surprising that the hard material softened below the stabilized value of the annealed material.

The stabilized value of flow stress for the annealed aluminum is

8,000

17 CPS

1.5 CPS

100 CPS

6,000

MAXIMUM
SHEAR
STRESS

4,000

PSI

2,000

0

.01   .02   .03   .04   .05   .06   .07   .08
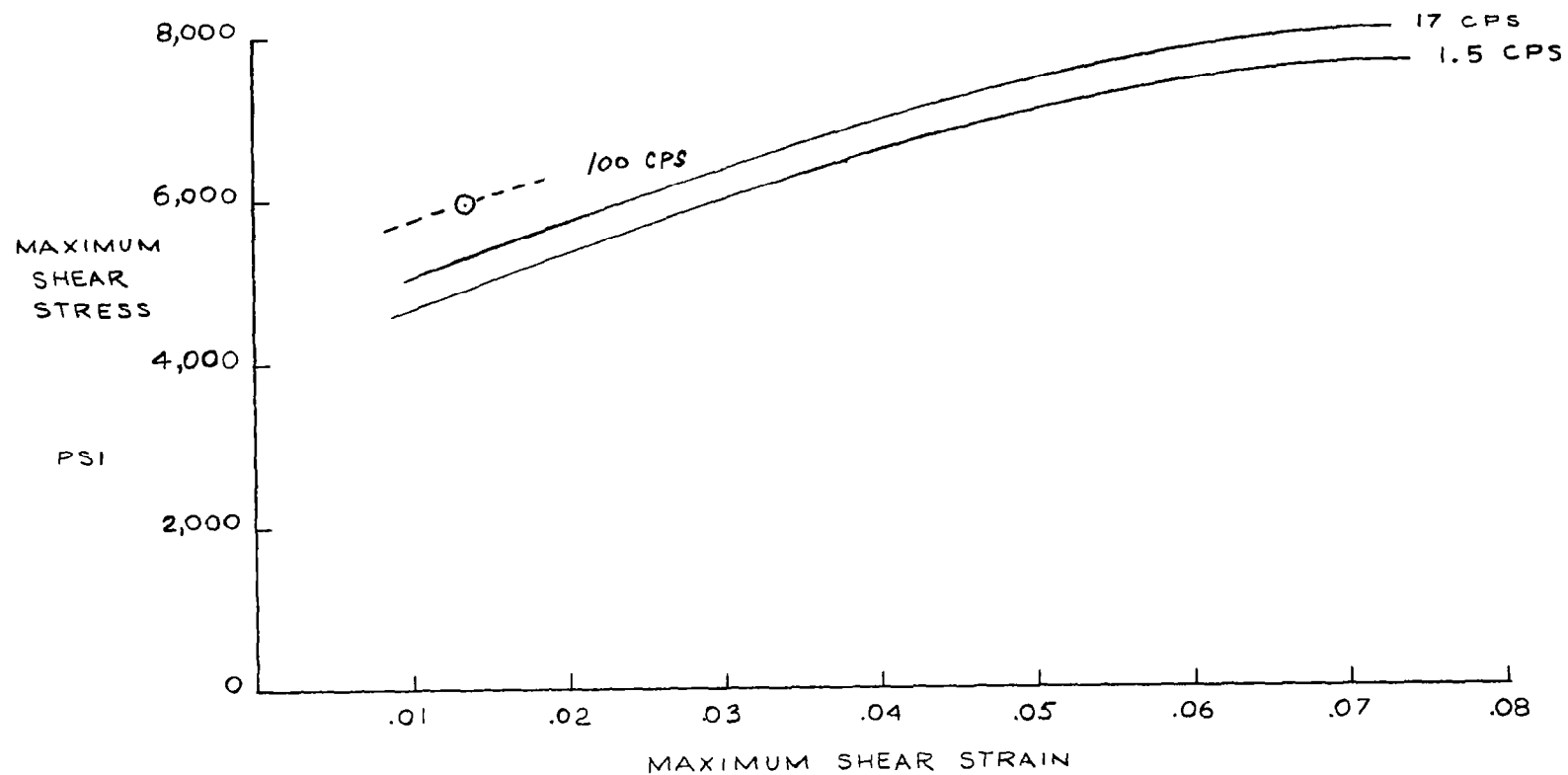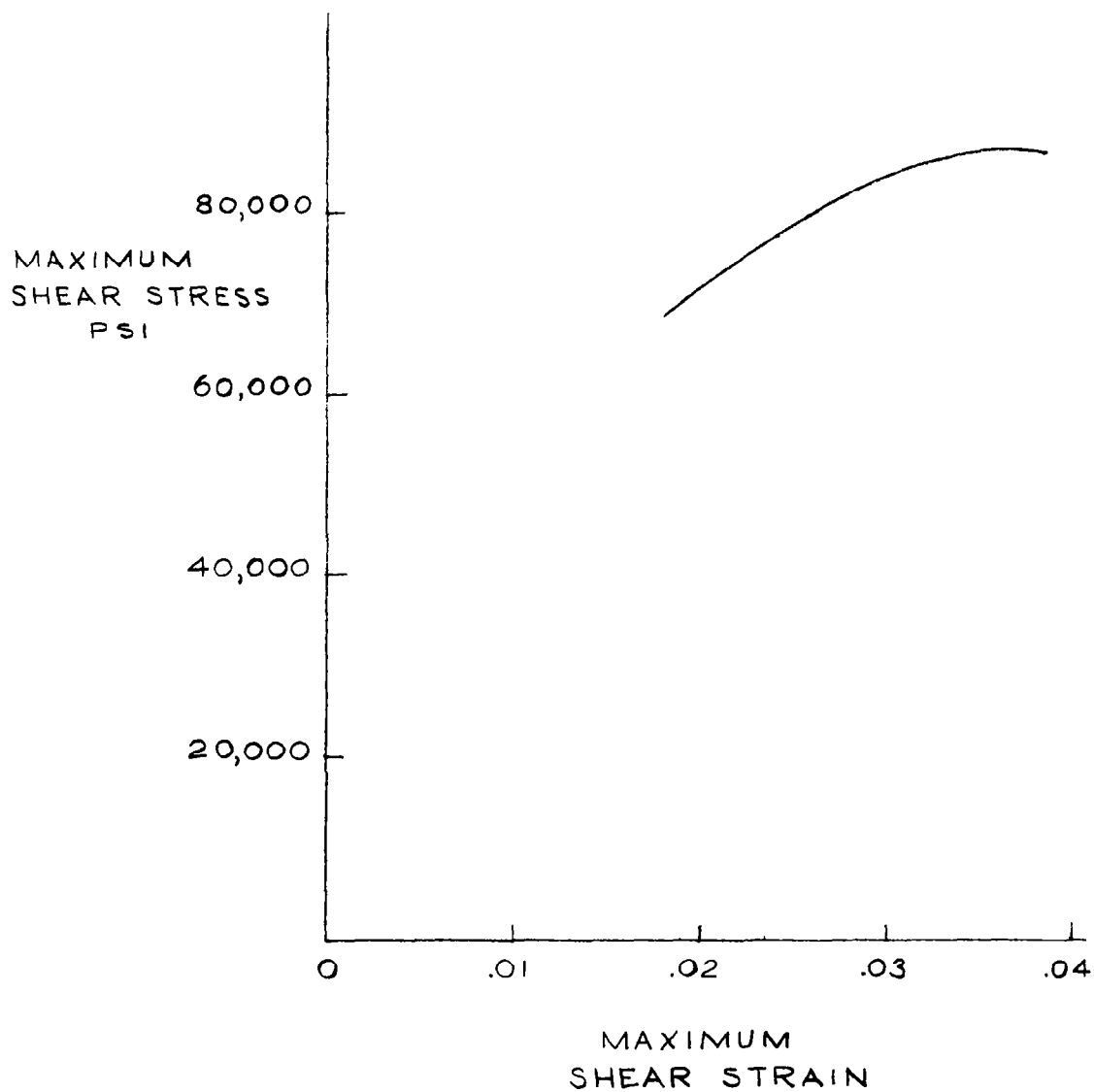
MAXIMUM SHEAR STRAIN

FIGURE 40.   CYCLIC STRESS-STRAIN CURVES FOR 1100-O ALUMINUM

FIGURE 41. CYCLIC STRESS - STRAIN CURVE FOR MOLYBDENUM TZM AT 1.5 CPS
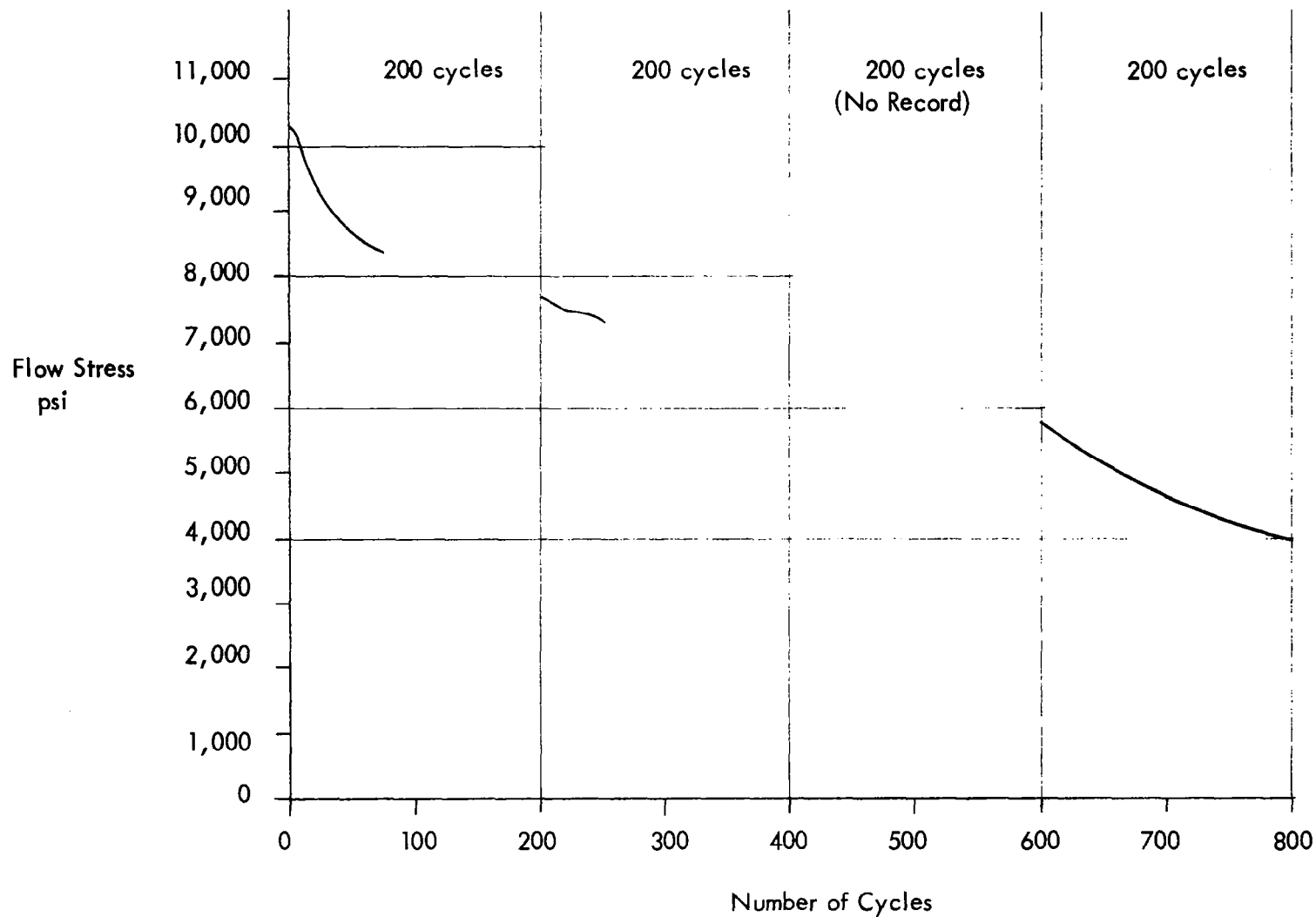
Figure 42.   Flow Stress vs Number of Cycles for Hard 1100 Aluminum at
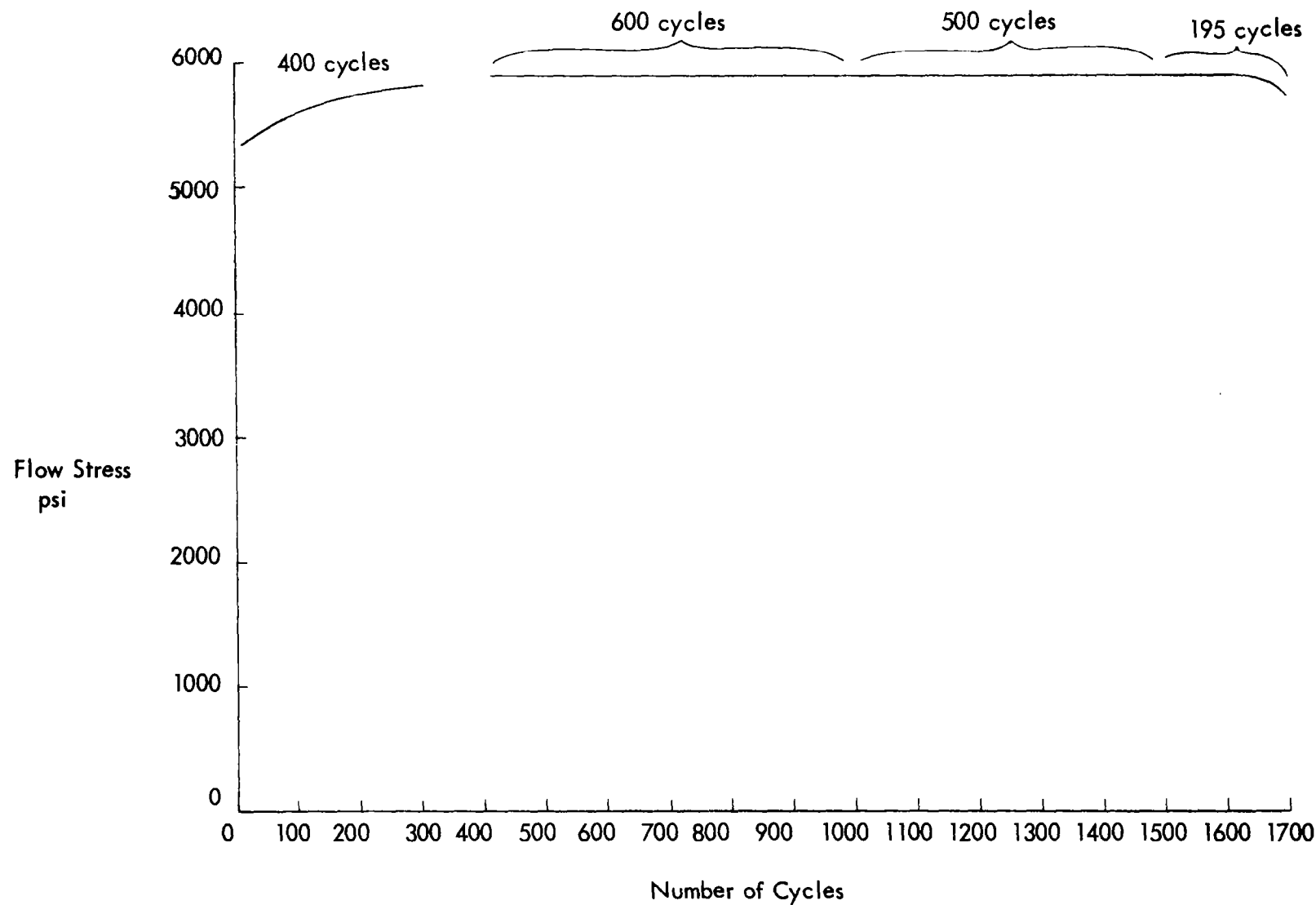1.5% Strain Range and 100 cps

Figure 43. Flow Stress vs Number at Cycles for Annealed 1100-0 Aluminum
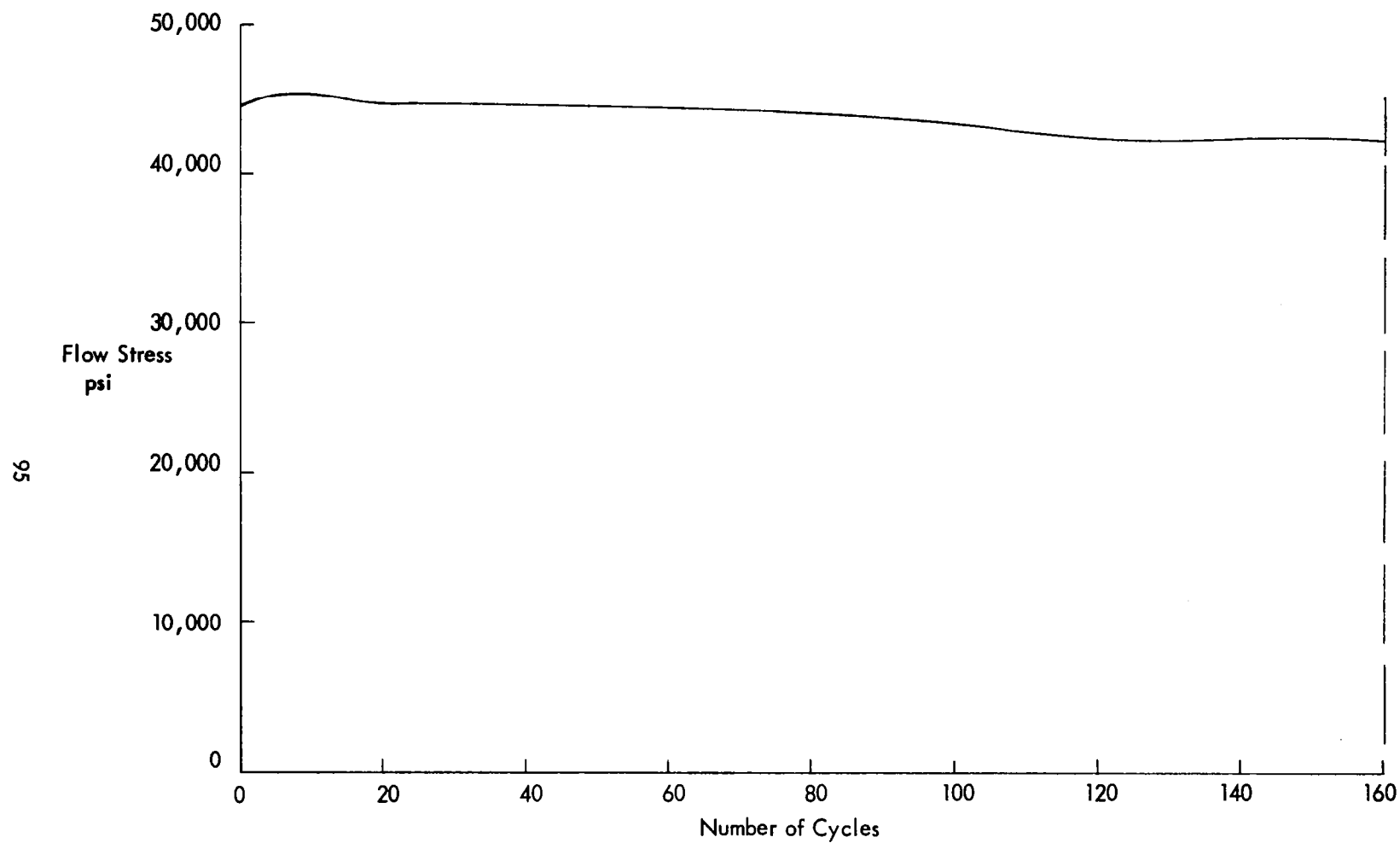at 1.5% Strain Range and 100 cps

Figure 44.   Flow Stress vs Number of Cycles for Annealed 347 Stainless Steel
at 1.3% Strain Range and 100 cps

plotted in Figure 40 along with the 1.5 and 17 cps data. Average rate sensitivities for aluminum, computed from this data, range from 0.02 to 0.03 between 1.5 and 17 cps to 0.06 between 17 cps and 100 cps. These values are consistent with those for unidirectional straining at room temperature.*

Fatigue data for the three metals is shown in Figures 45 to 47, plotted as plastic shear strain range vs number of cycles to failure. Reference lines with a slope of - 1/2 are also shown, which indicate good agreement with Equation (36). To evaluate the constant C, it is necessary to apply a plastic flow criterion in order to convert $\Delta\gamma_p$ to $\Delta\epsilon_p$. The maximum shear criterion** gives $\Delta\gamma_p = \frac{3}{2}\Delta\epsilon_p$. On this basis the computed values for C are 0.42, 0.41, and 0.28 for the aluminum, stainless steel, and molybdenum, respectively. These values, although somewhat on the low side, compare favorably with typical values reported in the literature.***

Several other observations are of interest. For the aluminum, in which there was little temperature rise, the fatigue data indicates negligible differences between results for the various test frequencies. The stainless steel, however, shows a definite decrease in life at the higher frequency for the few data points available. Unfortunately, because the higher frequence apparently resulted in a greater temperature rise, it is difficult to ascertain whether the lower fatigue life is due to rate or temperature effects. Except for the highest strain range, there is also little difference between the 1.5 and 17 cps molybdenum data, although too few points are available to be conclusive. The low fatigue life for the large strain range at 17 cps is possibly due to a very large temperature rise in this case.

*See for example, Reference 17, Chapter 6
** See, for example, Reference 17, Chapter 8
*** See, for example, Reference 6

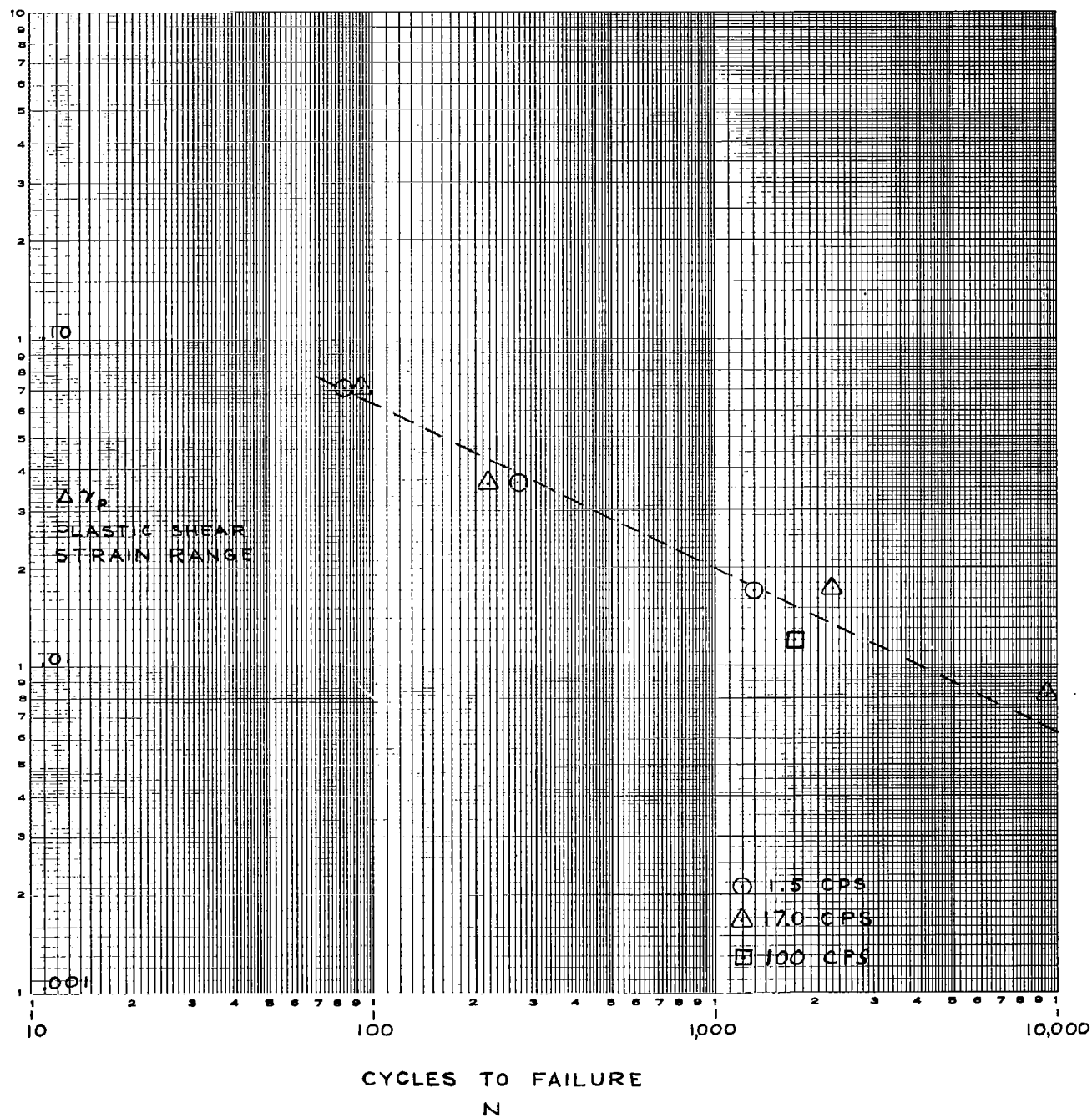FIGURE 45. CYCLIC TORSION FATIGUE CURVE
FOR 1100-O ALUMINUM ALLOY.

CYCLES TO FAILURE
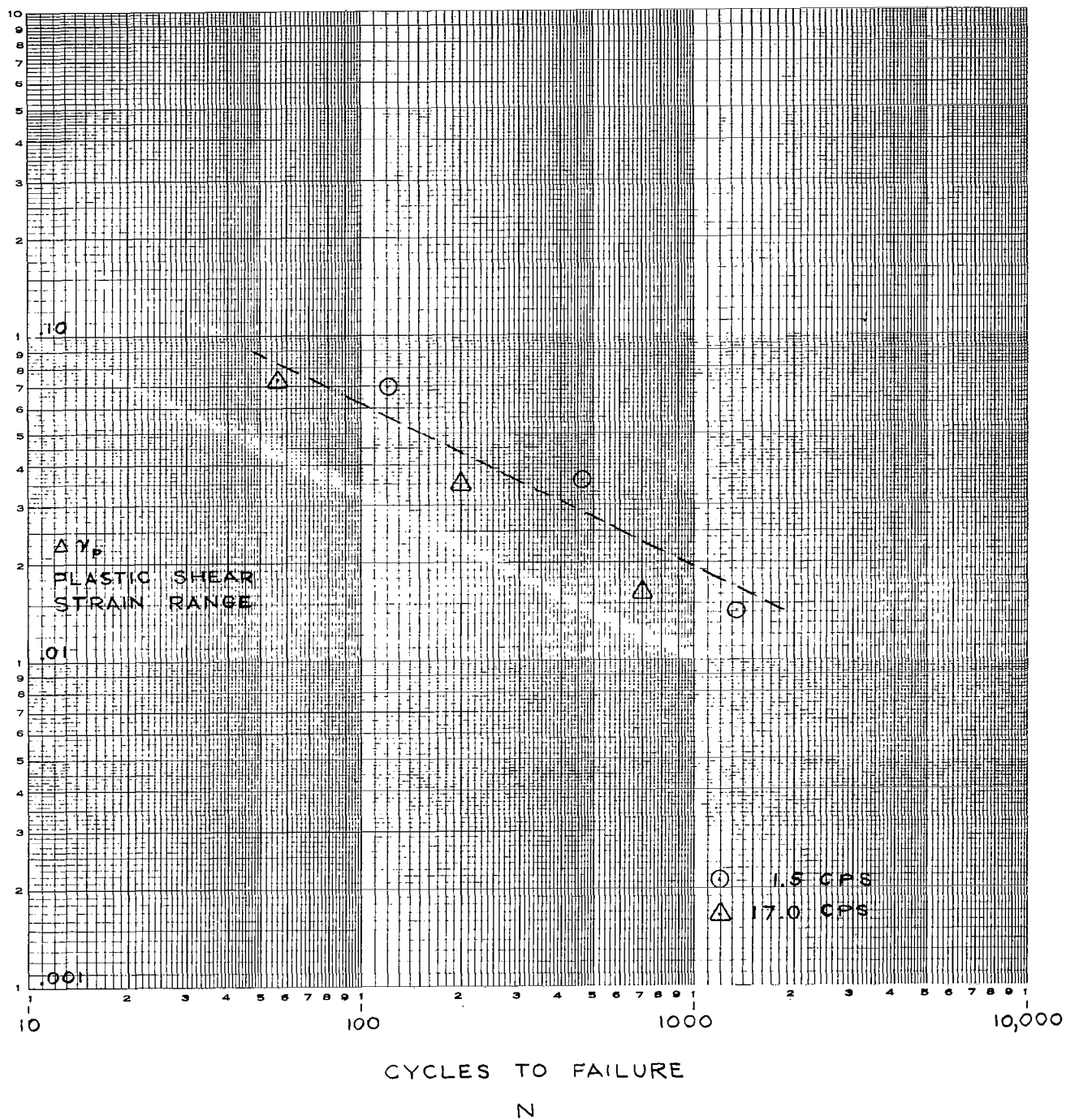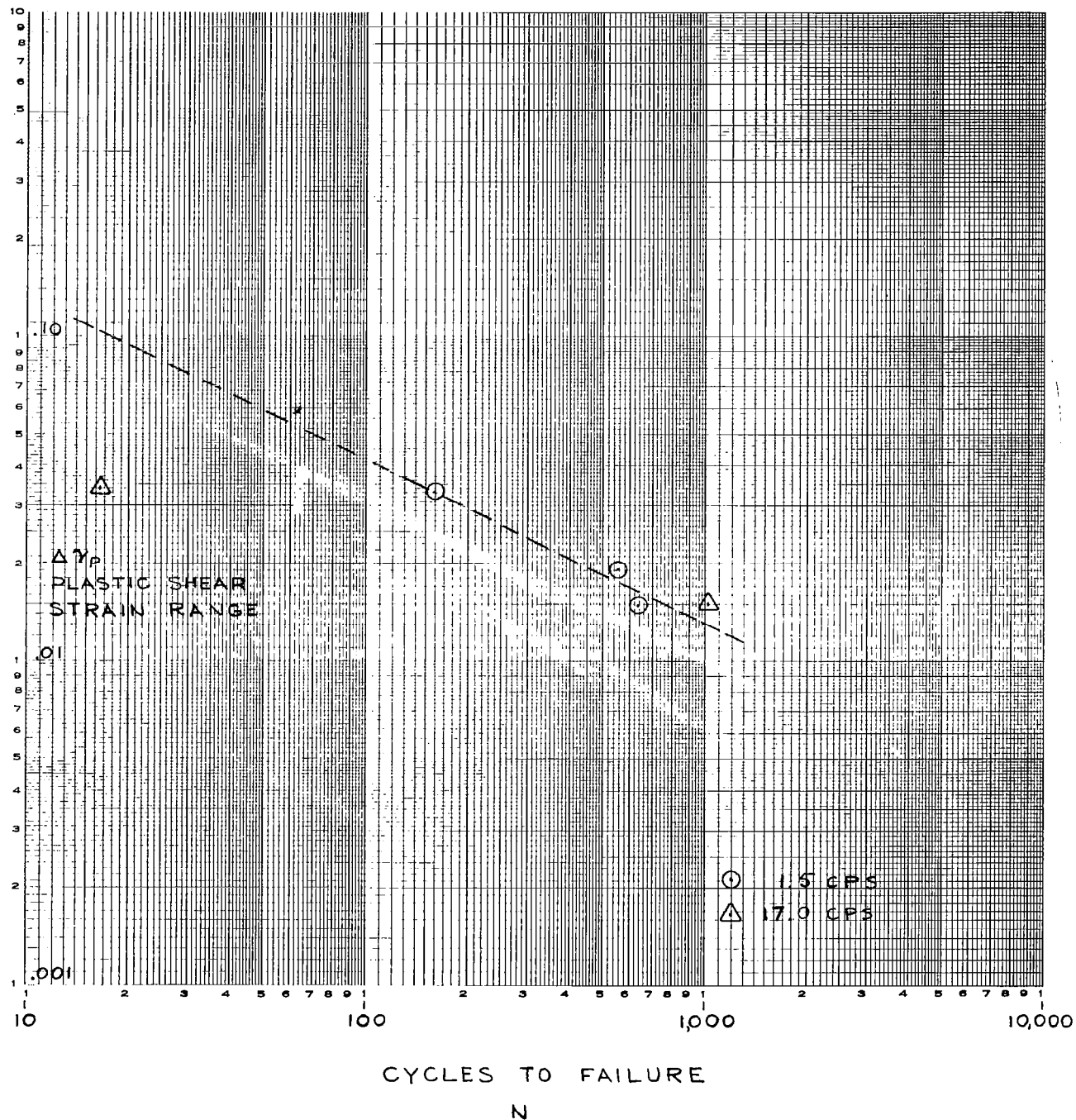N

FIGURE 46. CYCLIC TORSION FATIGUE CURVE
FOR 347 STAINLESS STEEL

CYCLES TO FAILURE
N

FIGURE 47. CYCLIC TORSION FATIGUE CURVE FOR MOLYBDENUM TZM ALLOY

CYCLES TO FAILURE

N

99

Despite the apparent ductility of molybdenum from tensile data, its fatigue life is somewhat below those of the aluminum and the stainless steel. Moreover, the molybdenum specimens exhibited a markedly brittle failure compared with the other metals.

The somewhat lower fatigue lives of all three metals, compared with typical data in the literature, is likely due to a considerable distortion of the thin-walled specimens, and subsequent strain concentrations toward the latter part of their lives. Figure 30 shows this distortion for some of the aluminum specimens.

b.   Nylon

Selection of the nonmetallic material to be studied was based upon the ability to obtain high strain levels and moderate to high stress levels, availability in various forms and sizes to satisfy testing requirements, material uniformity, and availability of information on mechanical properties. Accordingly, nylon 66, the polymer of hexamethylene diamine and adipic acid, available from several major sources, was selected. Its mechanical properties, including many of its small-amplitude dynamic characteristics, have been extensively investigated.

The results of the cyclic torsion tests with Apparatus I are presented in Table 1. Specimens were tested at three levels of frequency from 1.5 cps up to 33.5 cps and at three levels of strain amplitude up to 10%. Pertinent parameters were measured in order to obtain dynamic properties and to permit calculations of energy absorption and true strain amplitude. The data was reduced following the previously described procedure. Table 2 presents the results of this analytical treatment.

The energy absorption per cycle is presented in Figure 48

100

TABLE 1

Cyclic Torsion Tests of Nylon 66

Specimen No.	Input Strain Amplitude γ'_{max}(in./in.)	Frequency (cps)	Max Torque (in.lb)	Phase Lag (deg.)
401	0.04584	1.5	65.14	15.9
402	0.04584	17.0	69.69	17.6
403	0.04584	33.5	78.50	-*
404	0.0680	1.5	84.35	20.1
405	0.0680	17.0	91.00	-
406	0.0680	33.5	92.50	-
410	0.11465	1.5	97.20	-
410-B	0.11465	1.5	153.64	38.8
411	0.11465	17.0	106.00	-
412	0.11465	33.5	108.20	-

* Pulse generator did not operate

TABLE 2

Analysis of Nylon 66 Data

	Specimen No.			
Measured Parameters:	401	402	404	410-B
Input Strain Amplitude, γ'_{max}	0.04584	0.04584	0.0680	0.11465
Stress Amplitude, ζ_{max} (psi)	4,570	4,890	5,900	10,780
Frequency, (cycles/sec.)	1.5	17	1.5	1.6
Phase Lag, δ' (degrees)	15.9	17.6	20.1	38.8
Computed Parameters:				
$|G^{*'}|$ (psi)	99,700	106,700	86,800	94,000
G' (psi)	103,500	112,000	92,600	120,300
η (psi-sec)	38,500	3,300	26,900	15,900
G (psi)	126,800	143,000	112,800	156,500
$\tan \delta$	0.349	0.405	0.446	1.043
G_2 (psi)	39,400	49,800	41,700	78,200
G_1 (psi)	112,700	123,000	93,300	75,000
$|G^*|$ (psi)	119,300	132,700	102,200	108,300
True Strain Amplitudes	0.0383	0.0369	0.0578	0.0994
Specific Energy Absorption (in.-lb/in.^{3}, cycle)	182	209	437	2,425

FIG. 48

ENERGY ABSORPTION FOR NYLON 66

FREQUENCY
◇ 17 CPS
⊙ 1½ CPS

y-axis: $W_P \left(IN-LB/IN^3, CYCLE \right)$

x-axis: $\gamma^2_{max.}$ - 103 -
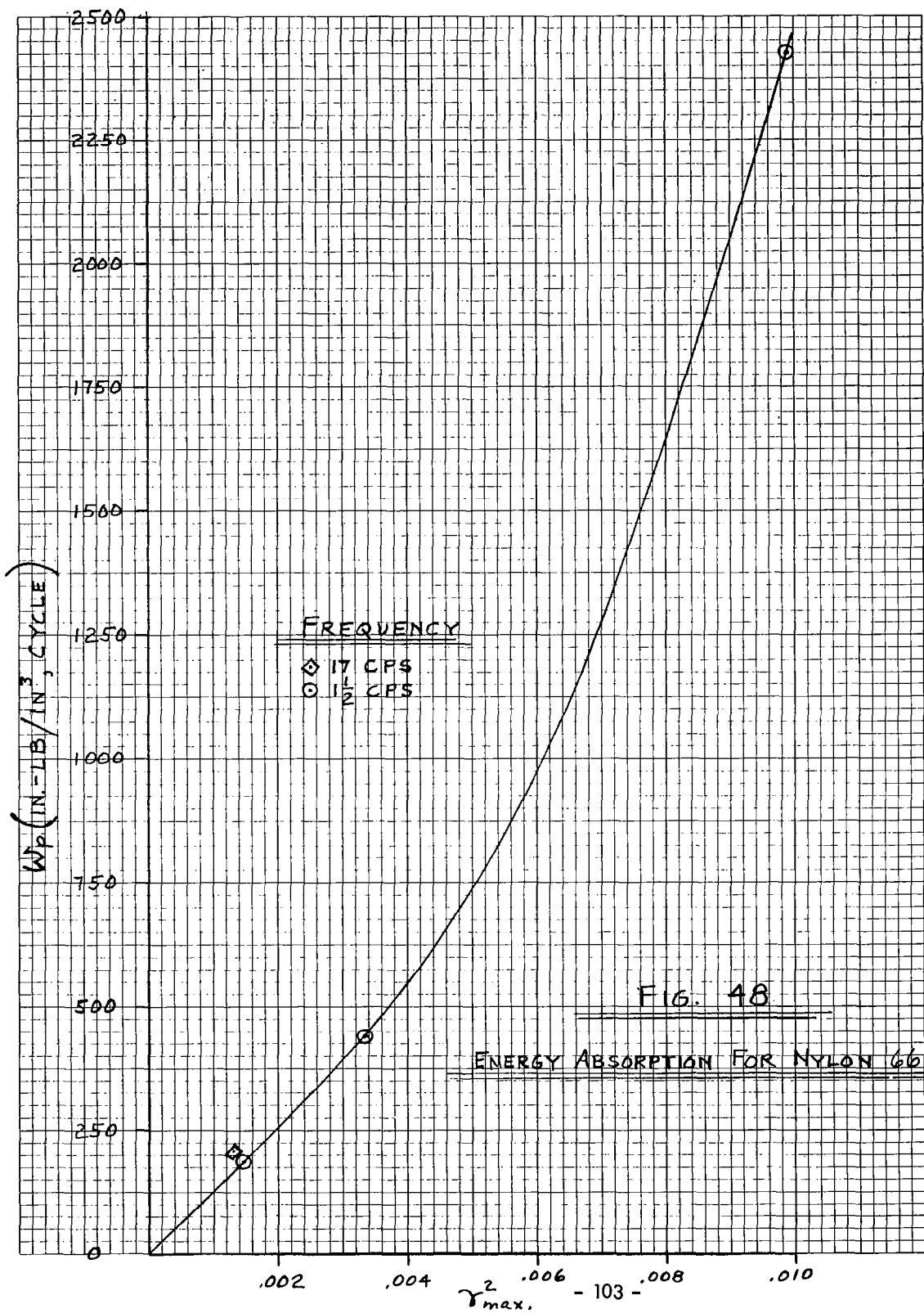
as a function of the square of strain amplitude. A linear relationship with the square of strain amplitude appears to hold at the lower strain levels, as might be expected from Equation (108). However, the energy absorption increases much more rapidly with increasing strain amplitude at the high strain levels, indicating appreciable nonlinearities in the viscoelastic parameters.

Some limited testing of nylon 66 was carried out at 100 cps with Apparatus II. Due to an appreciable temperature rise, most of the runs were limited to relatively short bursts. In some cases equilibrium temperatures were reached by utilizing a blower to cool the specimen. Typical data of stress vs number of cycles is shown in Figures 49 to 51 for 8, 10, and 15 percent strain ranges, respectively. The results of several tests carried to failure are shown in Table 3 and Figure 52.

Unfortunately, phase lag between stress and strain could not be determined at 100 cps. It was found, by cycling steel torsion bars well within the elastic range, that a phase lag resulted on the oscillograph records. The torsion bars were designed to approximate the stiffness of the nylon specimens. It is believed that the error was due to an electrical signal resulting during amplification of the load cell output prior to input to the galvanometer. Since phase lag could not be determined, it was not possible to determine the complex moduli at 100 cps with the present apparatus.

Although the temperature measurements were rather crude, the recorded temperature rises were far below those values predicted on the basis of the previously determined loss moduli and specific energy absorption values. Thus, an appreciable frequency effect on phase lag and loss modulus seems to be indicated. However, the results of tests with the friction torus device utilizing nylon elements, presented
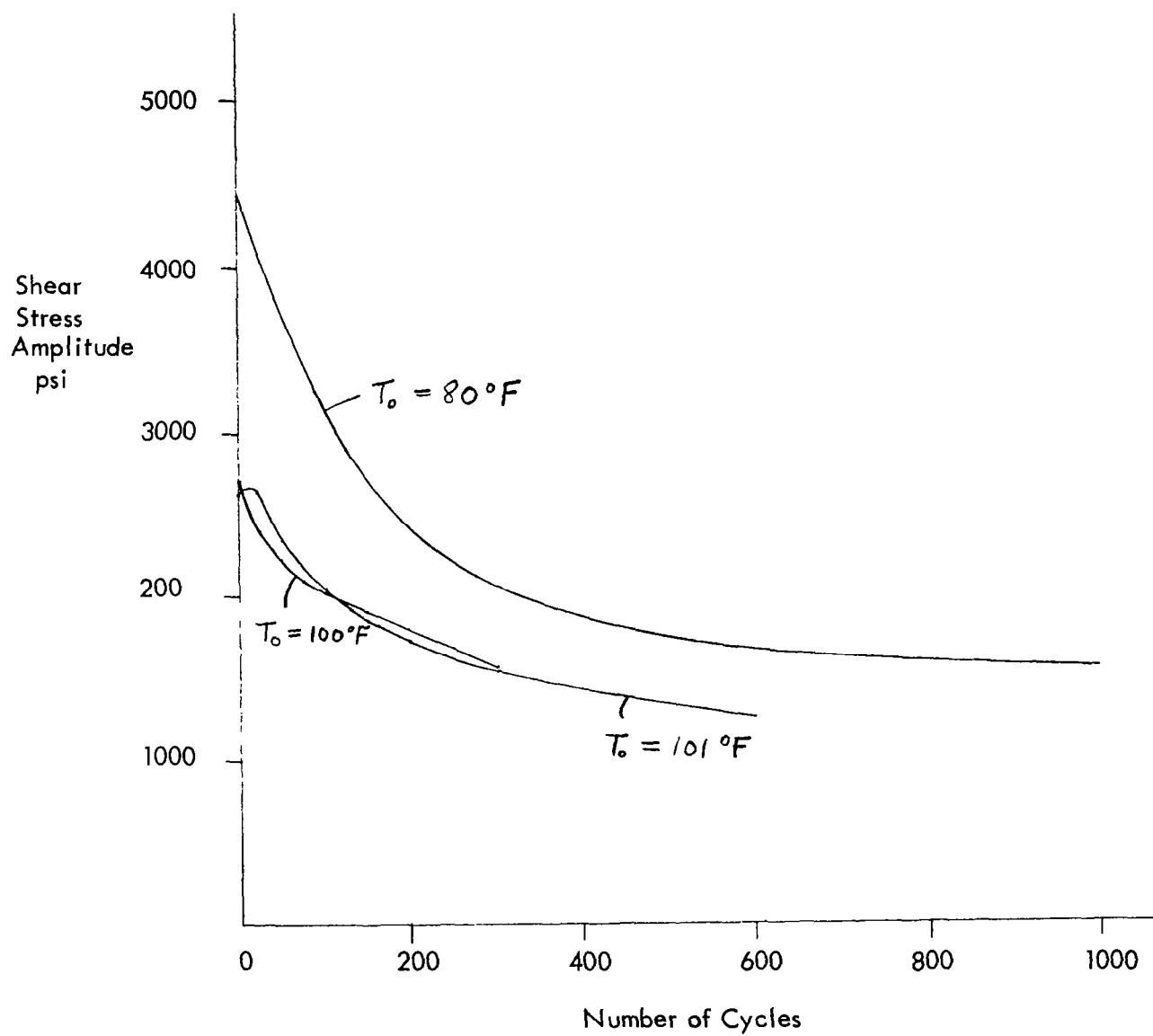
Figure 49.   Stress Amplitude vs Number of Cycles for Nylon 66
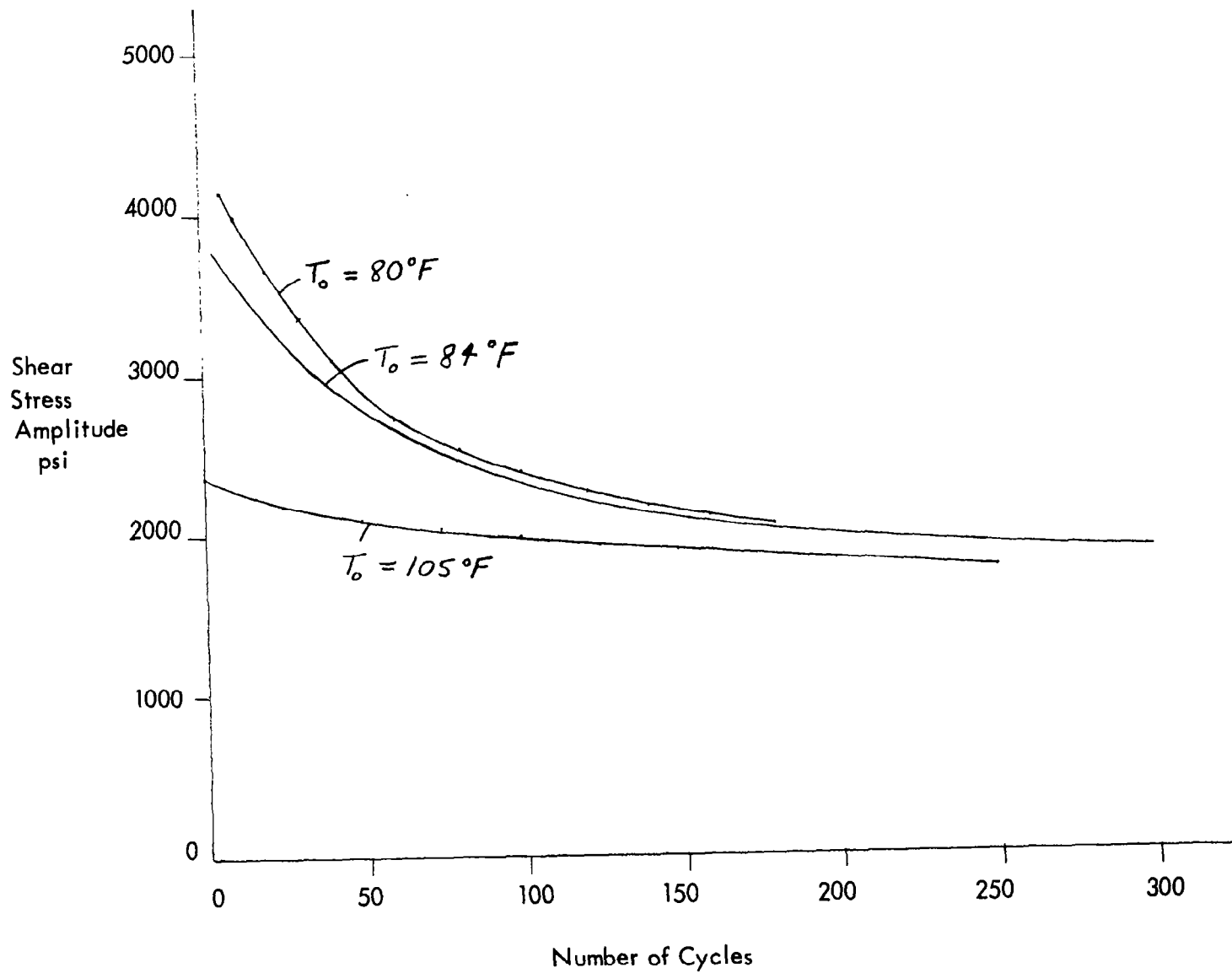at 8% Strain Range and 100 cps

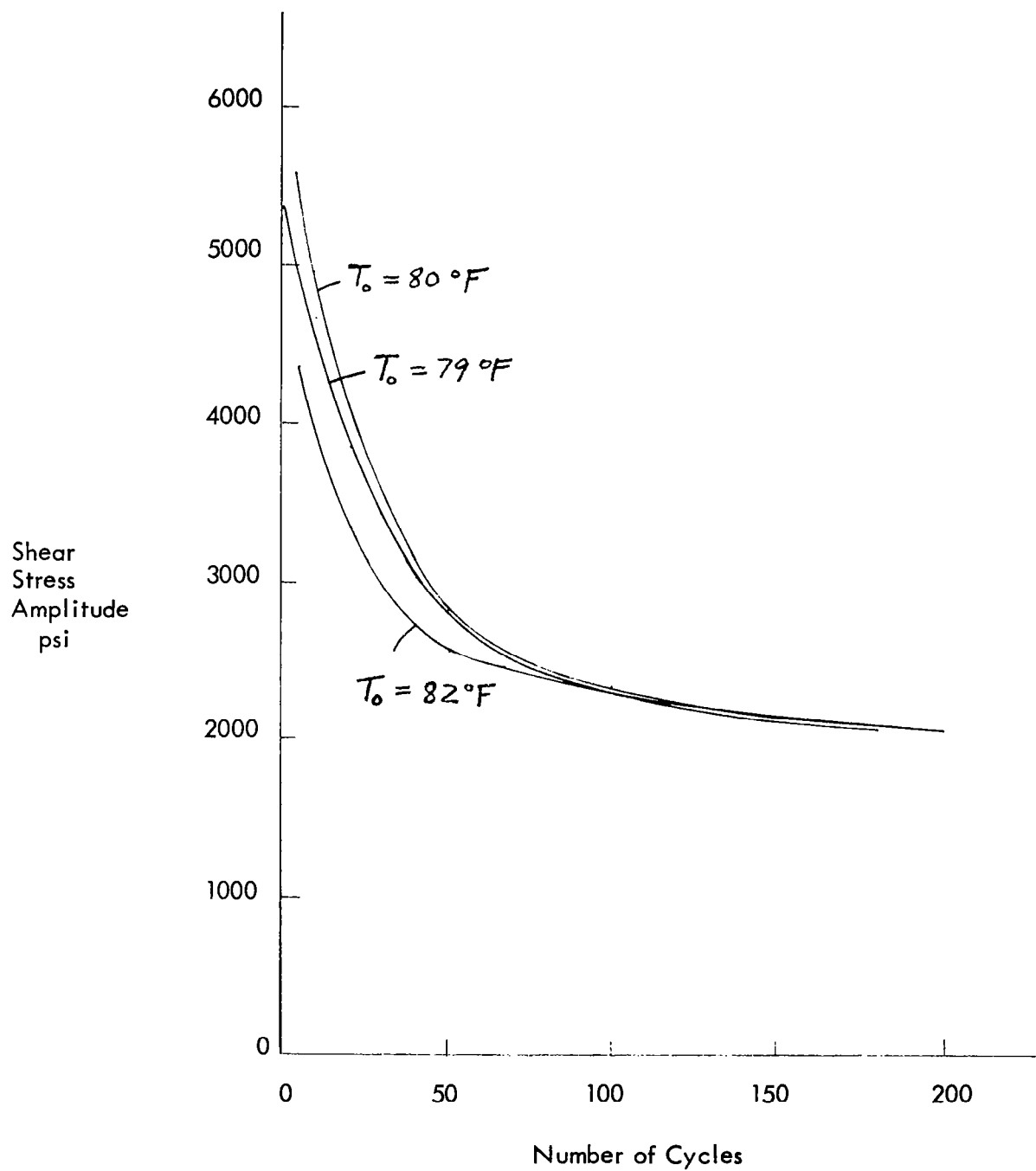Figure 50. Stress Amplitude vs Number of Cycles for Nylon 66 at 10% Strain Range and 100 cps

Figure 51.   Stress Amplitude vs Number of Cycles for Nylon 66
at 15% Strain Range and 100 cps

Table 3. **Summary of Fatigue Tests for Nylon 66**

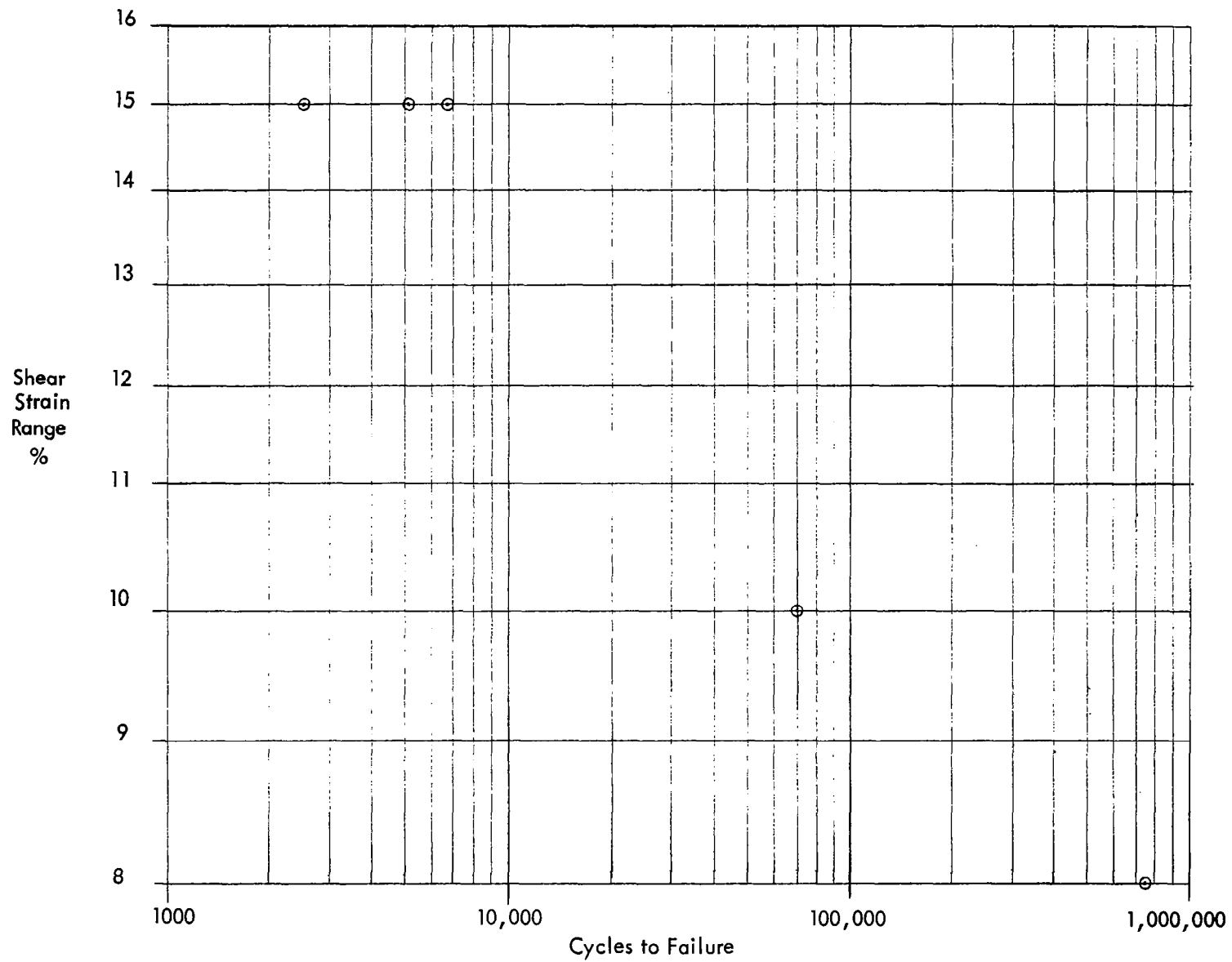| Specimen No.	Strain Range	Average Cycles Per Burst	Average Initial Temperature	Average Final Temperature	Cycles To Failure
392	8%	10,000	90°F	170°F	740,100
338	10%	1,500	84	196	72,000
299	15%	375	82	183	2,550
307	15%	400	82	202	6,705
325	15%	400	82	175	5,100

Figure 52.   Fatigue Data for Nylon 66 at 100 cps

in Section VII B, do not support this observation. Rather, the test results indicate that specific energy absorption is relatively insensitive to frequency. In view of these apparent discrepancies, it appears that further modification of the apparatus and further testing at various frequencies would be of interest.

With regard to the limited fatigue data for nylon 66, the results of Figure 52 indicate a much more significant variation in fatigue life with strain amplitude than for ductile metals. For example, if a relation in the form of Equation (35) were fit to the present data, using total strain rather than plastic strain, the exponent α would be approximately 1/8. In other words, the fatigue life for nylon 66 is approximately inversely proportional to the eighth power of total strain range.

B.   Torus Impact Device

The foregoing concepts and principles were applied in the design, construction and testing of a simple torus device with friction drive, as illustrated in Figure 1. Both quasi-static and impact tests were conducted using 1100-aluminum and nylon 66 working elements. Details of the design and a discussion of the test results are presented in the following sections.

1.   Design and Construction

The test device consists of two concentric tubes which drive one or more torus elements, as shown in Figure 53. The torus elements consist of loops of a ductile metallic or nonmetallic wire which may be in the form of individual rings or one continuous spiral. The individual rings need not be joined at the ends. Drive is accomplished through friction coupling produced from a built-in interference between the torus elements and the concentric tubes. The thickness of the outer tube is tapered at the end, as shown in the sketch, in order to provide for simple assembly. The outer tube is constructed of 6061-T6 aluminum alloy with a 2.50-inch OD and a 0.070-inch thick wall, and the inner
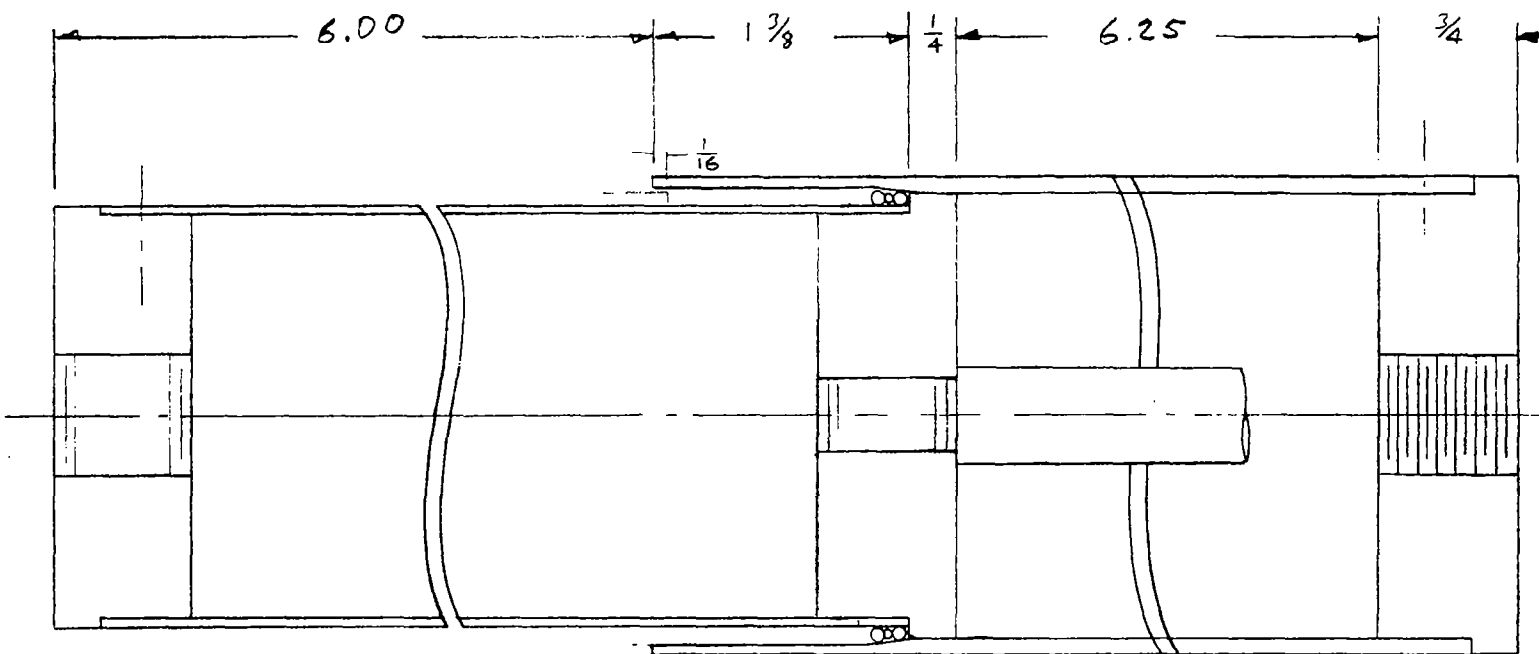
110

Figure 53. Tube Device.

tube is 2024-T3 aluminum alloy with a 2.24-inch OD and a 0.076-inch thick wall.*
Photographs of the actual device are shown in Figure 54.

Interferences were varied by varying the diameters of the wire elements. In the case of the aluminum elements, 0.064-inch diameter wires were slightly reduced in diameter by plastic elongation. It was found that the aluminum elements would roll for only a very narrow range of interferences or wire diameters. A discussion of this behavior will be presented later. The nylon elements rolled for a considerably wider range of interferences. A series of tests was run with nylon wires ground to diameters ranging from 0.064 to 0.069 inch.

Estimates of the resisting forces based on longitudinal deformation only can be determined from the cyclic torsion data in conjunction with the previously developed relationship of Equation (51). Figure 55 shows curves of ω_p^- and $\omega_p^- \Delta \gamma_T$ vs $\Delta \gamma_T$ for aluminum, based on the data of Figure 33. Numerical integration of these results with the values $R = 1.148$ inches and $d = 0.064$ inch yields the design force for a single aluminum element of 49 lbs.

For evaluation of the nylon element, Equation (51) can also be expressed in terms of strain amplitude, γ_{max} to give
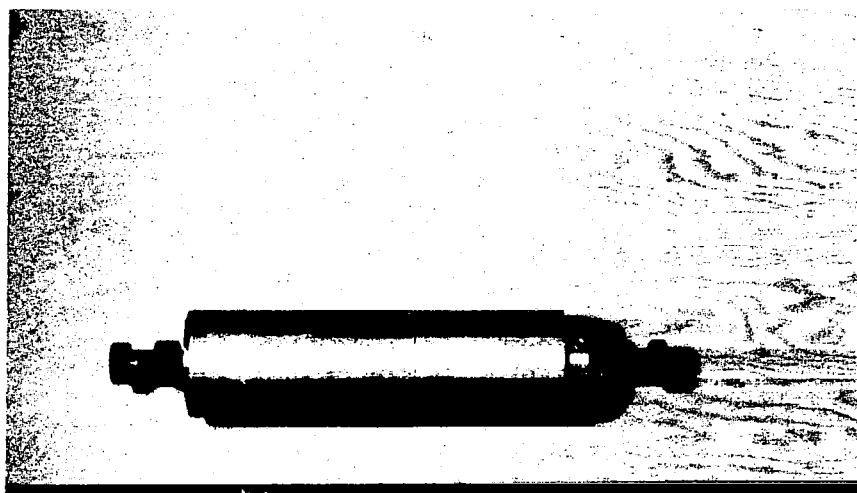
$$F = \frac{\pi}{3} \frac{R^3}{d} \int_{\gamma_{max}=0}^{\frac{\sqrt{3}}{2}\frac{d}{R}} \omega_p^- \, d(\gamma_{max}^2) \quad . \tag{109}$$

This integral is simply the area under the curve of Figure 48. Evaluation of Equation (109)

---

*These dimensions are only nominal. Due to variations in the tube dimensions, the annular width varied about an approximate value of 0.0625 in.
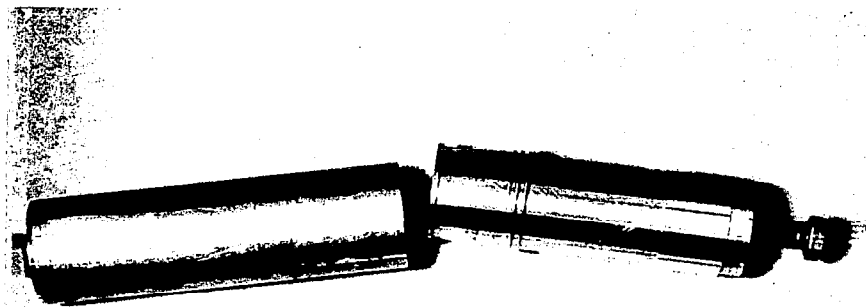
Figure 54. Photographs of Test Device

Figure 55.
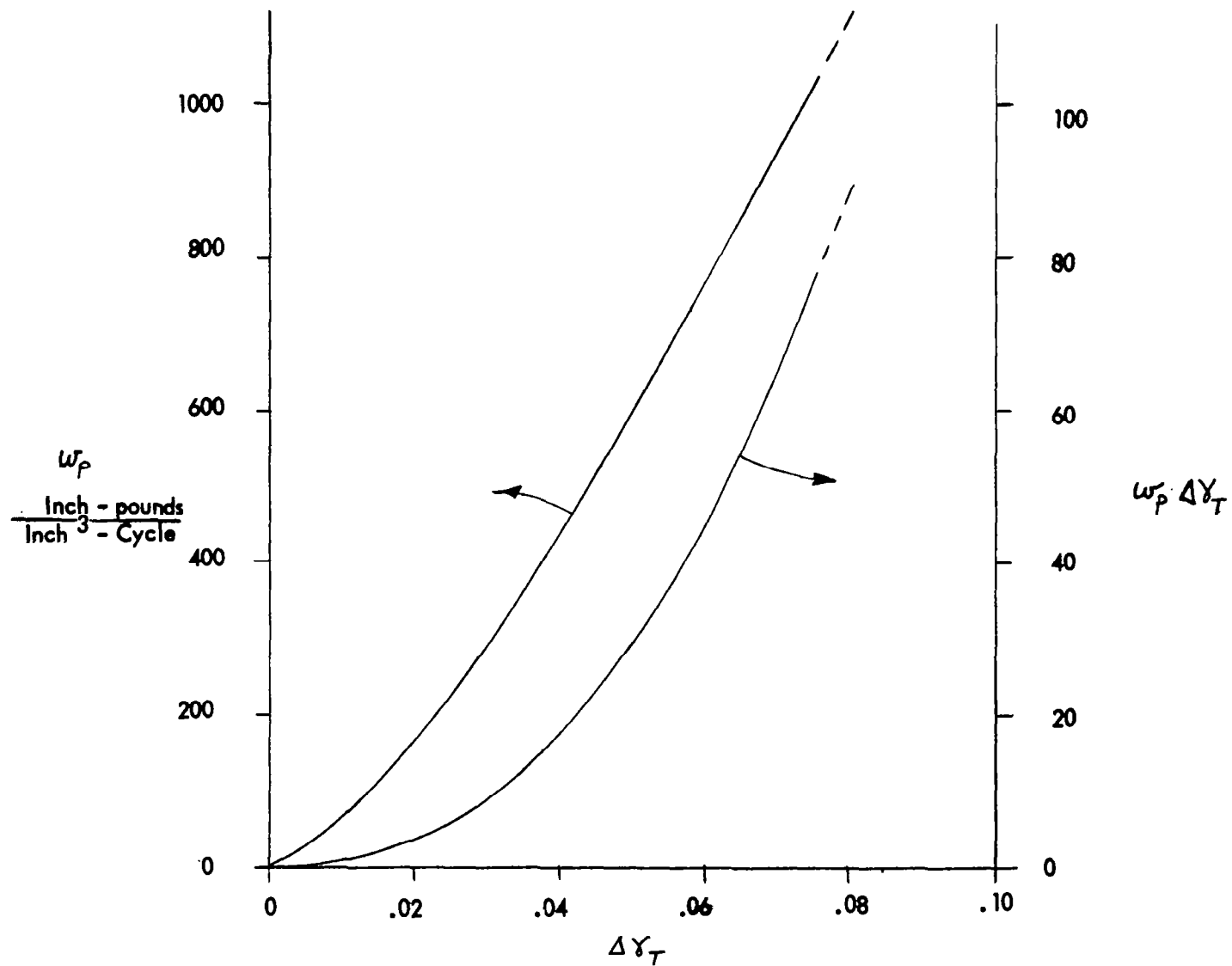
$\underline{W_P \quad \underset{i}{\xi} \quad W_P \Delta \gamma_T \quad \text{vs} \quad \Delta \gamma_T \quad \text{For 1100 Aluminum at 1.5 CPS}}$

113

with these results yields a value of 8.8 lb for a single element of nylon.

The effect of lateral compression on the nylon element was computed using the procedure developed in Section VI B. These results are presented in Figure 56 in terms of F/G_2 vs d, based on an annular width of 0.0625 inch, and will be discussed further in conjunction with the test results.

2.   Test Procedures

Two types of tests were performed with both aluminum and nylon working elements. Quasi-static tests were performed with a Dillon testing machine, and load-stroke curves were determined with the aid of a strain-gage load cell and an oscillograph recorder. The test set-up is shown in Figure 57. Typical load-stroke curves are shown in Figure 58. The strain cycling rate of the working elements was approximately 0.086 cps.

In order to study the performance under impact conditions, drop tests were performed by dropping weights on the device from various heights. Deceleration-time and load-stroke behavior was determined by multiple-exposure photographic records taken with the aid of a strobe-light system. This test-set-up is shown in Figure 59. A typical photographic record is shown in Figure 60.

3.   Test Results

Quasi-static and drop results are shown in Tables 4 and 5 and Figures 61 to 66. Table 4 is a summary of quasi-static and drop results for aluminum working elements. Table 5 is a summary of quasi-static results for nylon working elements. Figure 61 summarizes the nylon drop results in terms of force vs drop height for various wire diameters. A comparison of quasi-static and drop results for the nylon is shown in Figure 62.

114

Figure 56. Effect of Lateral Compression of Nylon Torus Element

Wire Diameter, d (in.)

115
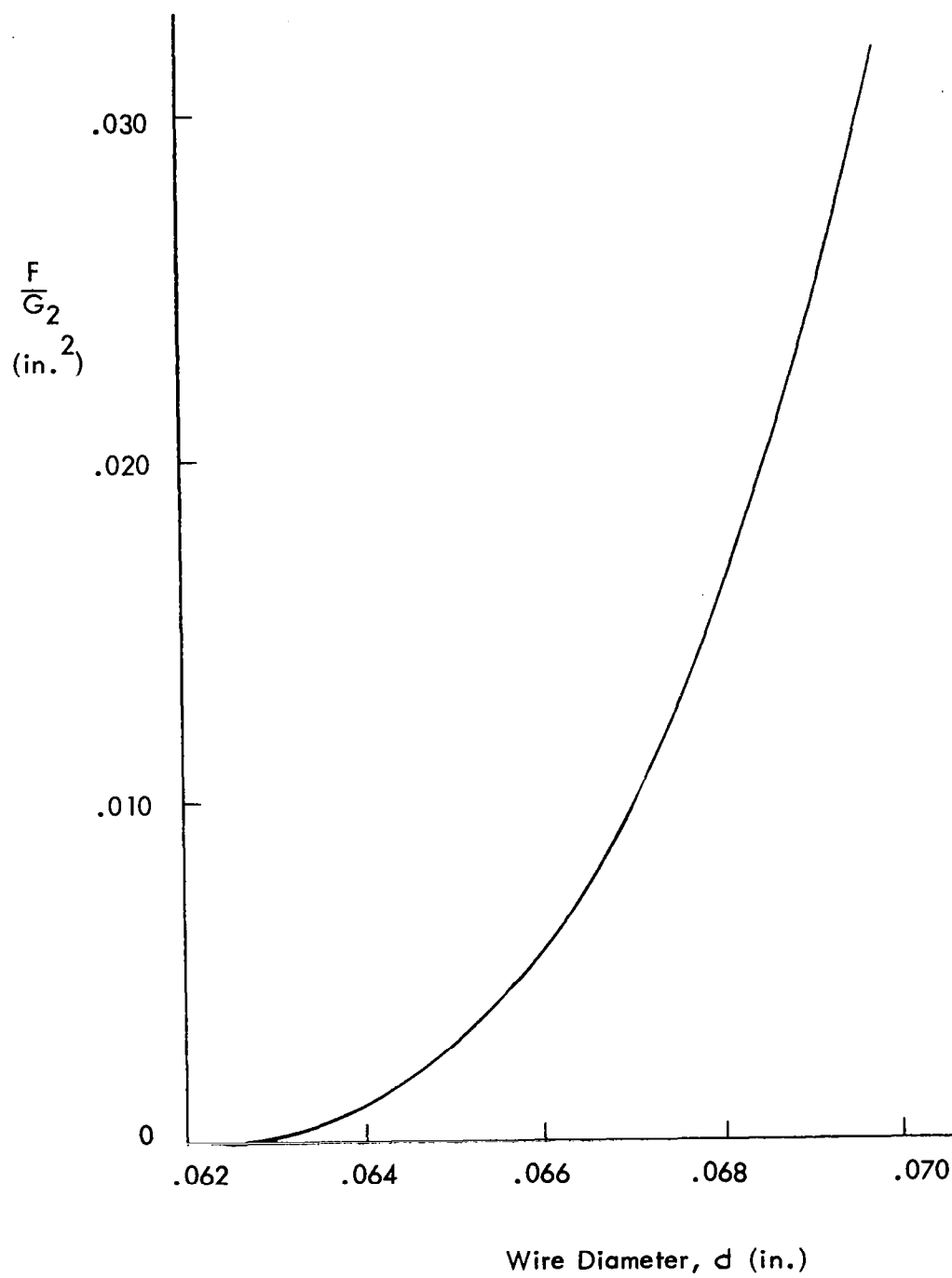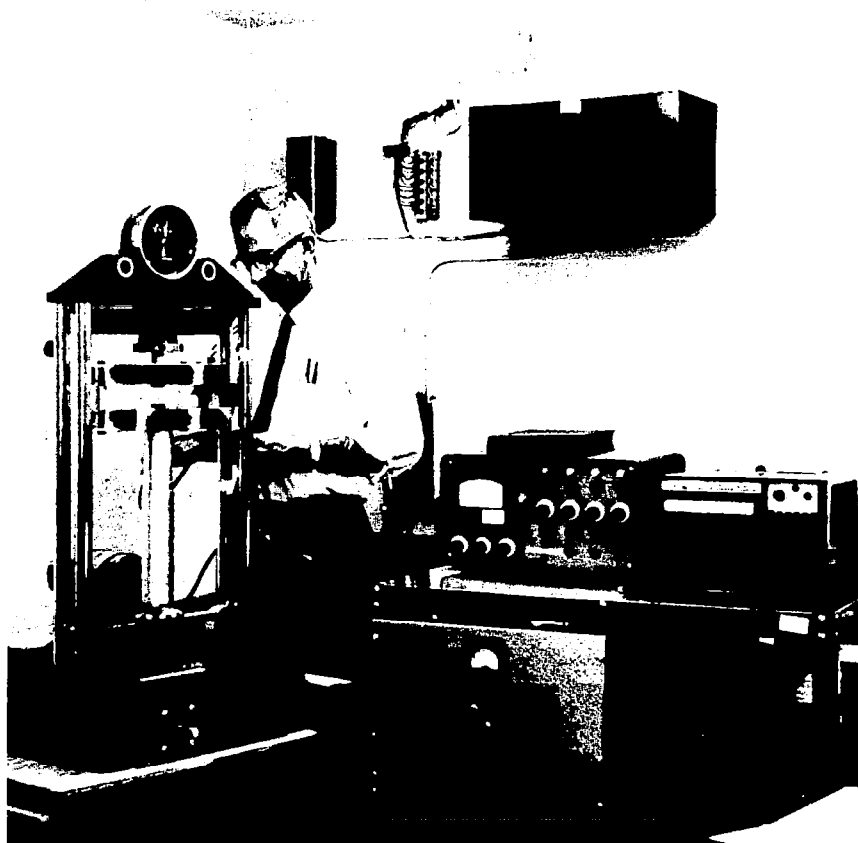
Figure 57.   Torus Device in Dillon Testor

Aluminum Working Element

NYLON TORUS (2 Turns)

1 CYCLE OF TORUS

COMPRESSION

TIME →
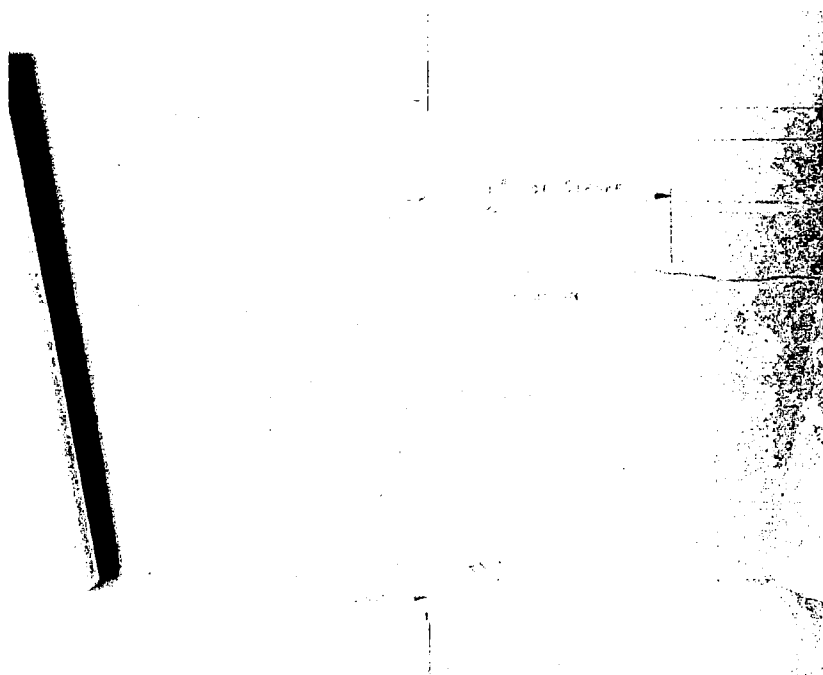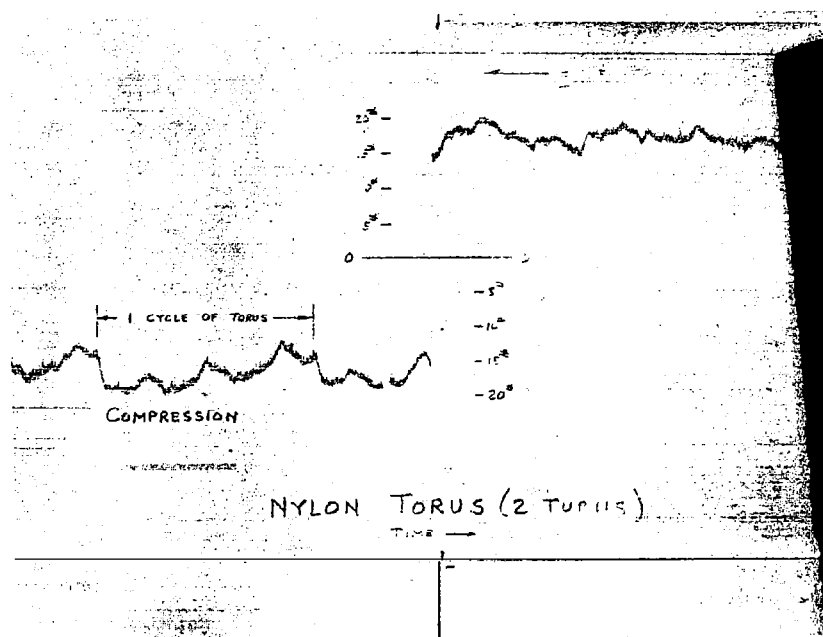
Nylon Working Element

Figure 58. Typical Quasi-Static Load-Stroke Record

117
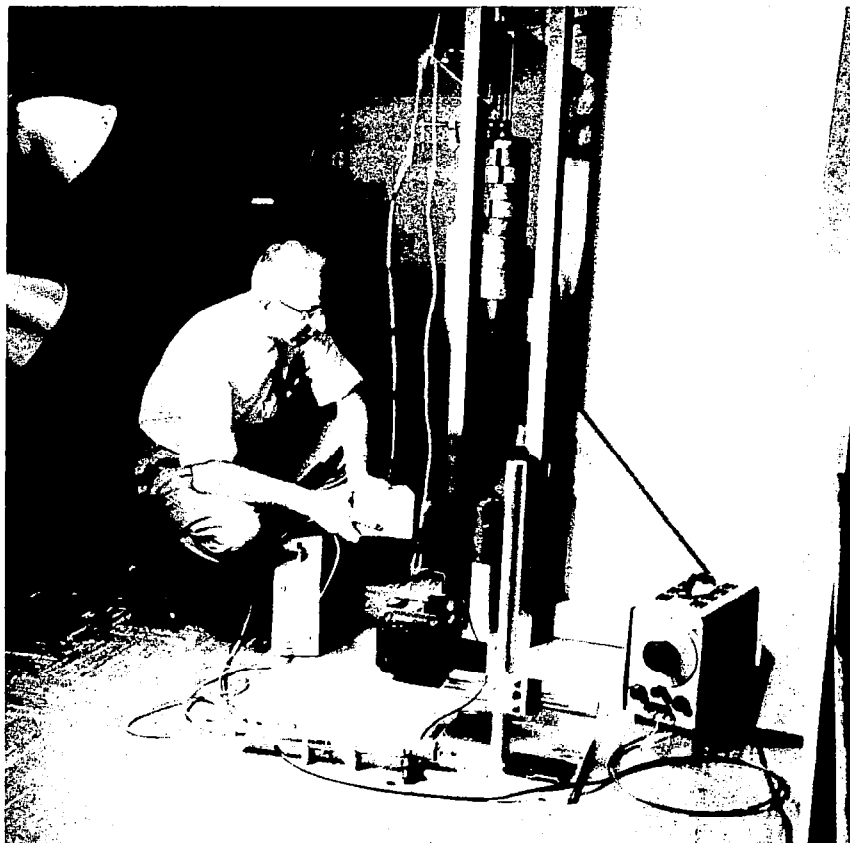
Figure 59.   Drop Test Set-Up.
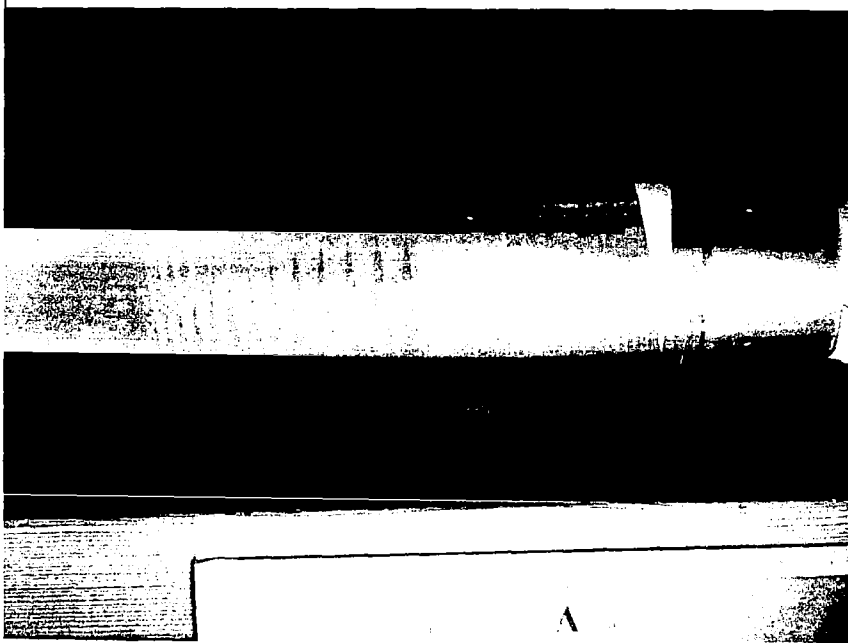
Figure 60. Typical Drop Test Record

FIGURE 61. FORCE VS DROP DISTANCE
FOR NYLON ELEMENTS
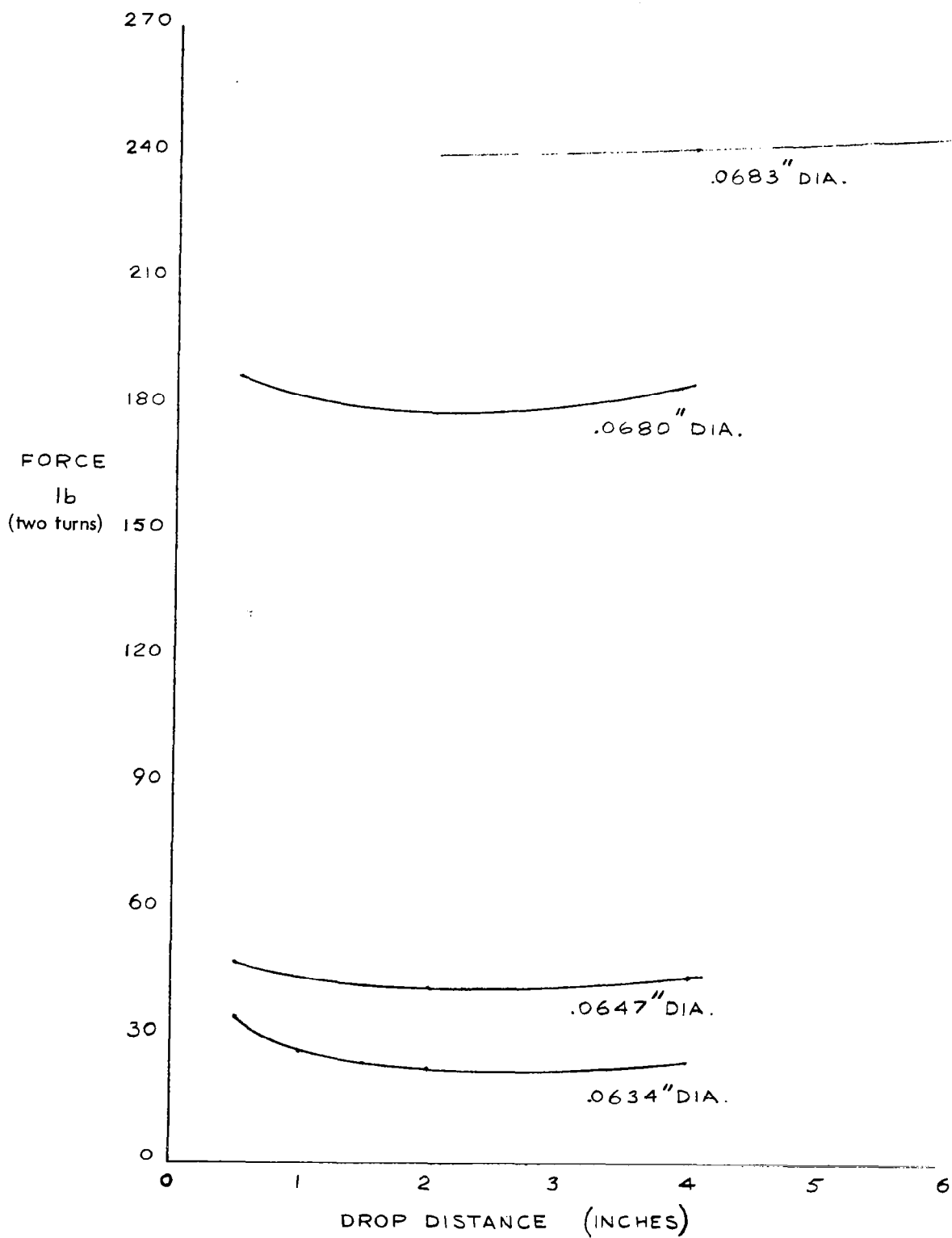
FIGURE 62. COMPARISON OF QUASI-STATIC AND DROP RESULTS FOR NYLON ELEMENTS
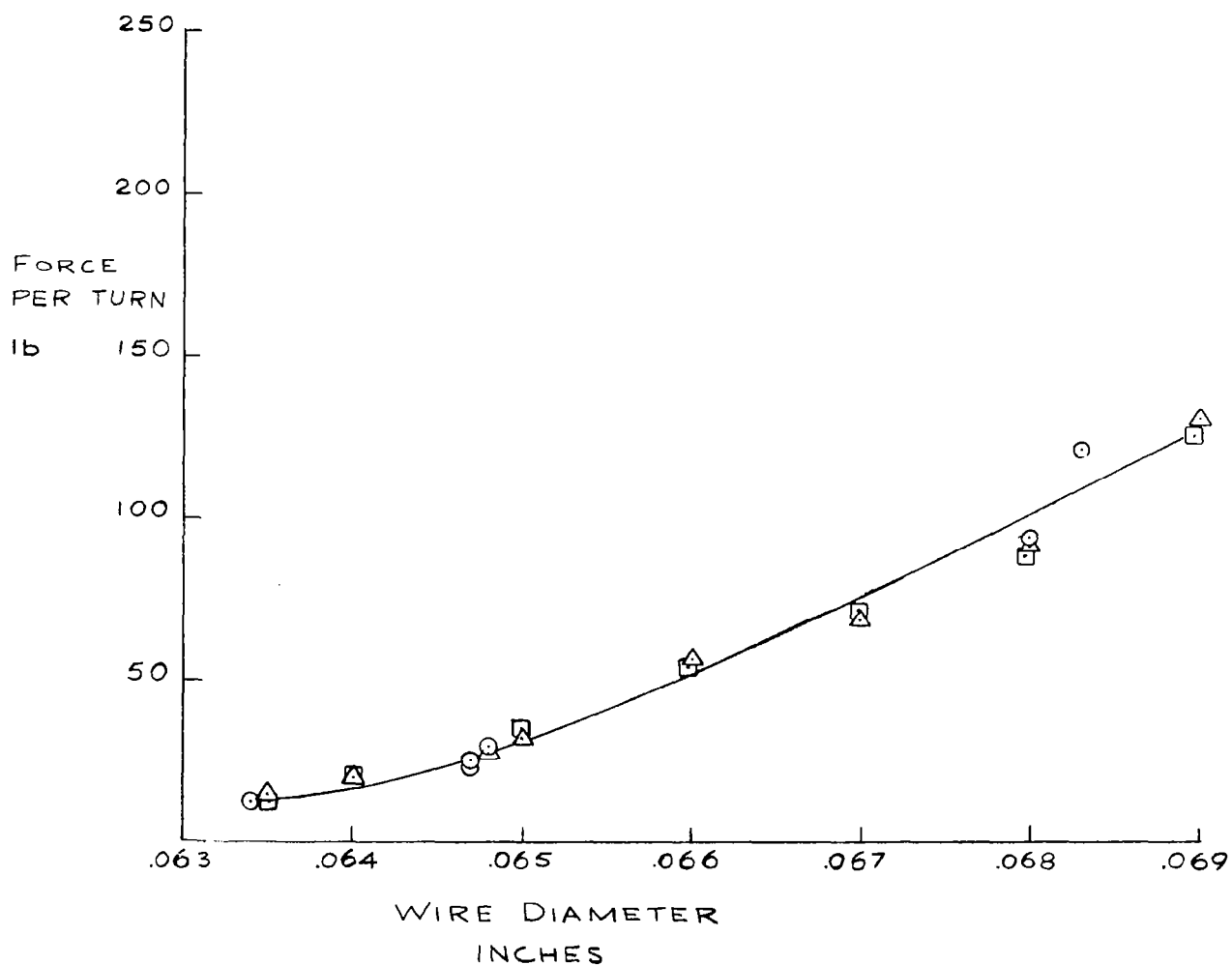
⊙ 4 INCH DROP

△ 2 INCH DROP

⊡ QUASI-STATIC

FIGURE 63. TYPICAL DISPLACEMENT-TIME & VELOCITY-TIME CURVES FOR ALUMINUM

DATA: 1 TURN .0632" DIA. WIRE
2 INCH DROP

FIGURE 64. TYPICAL DISPLACEMENT-TIME & VELOCITY-TIME CURVES
FOR ALUMINUM

DATA: 1 TURN .0633" DIA. WIRE
3 INCH DROP

123

111-10
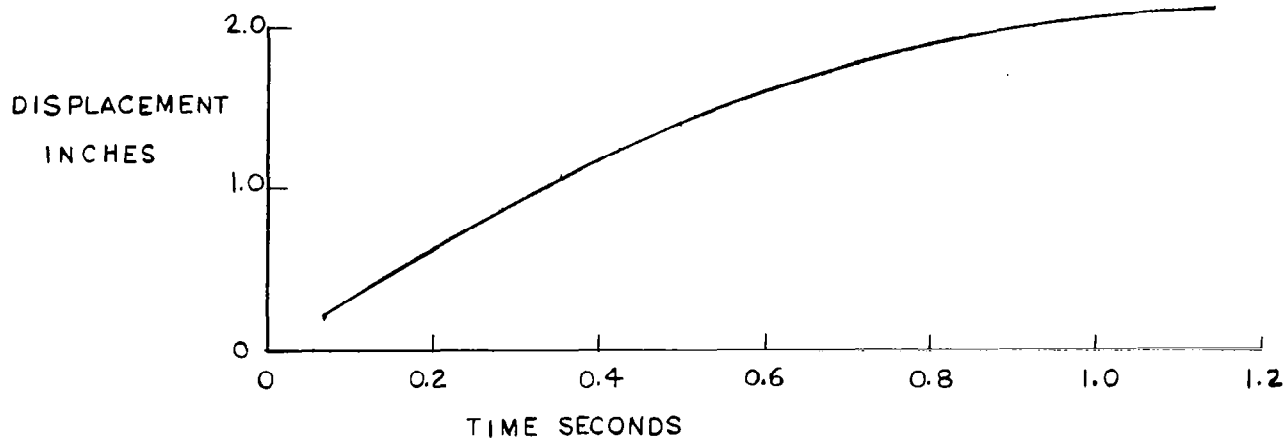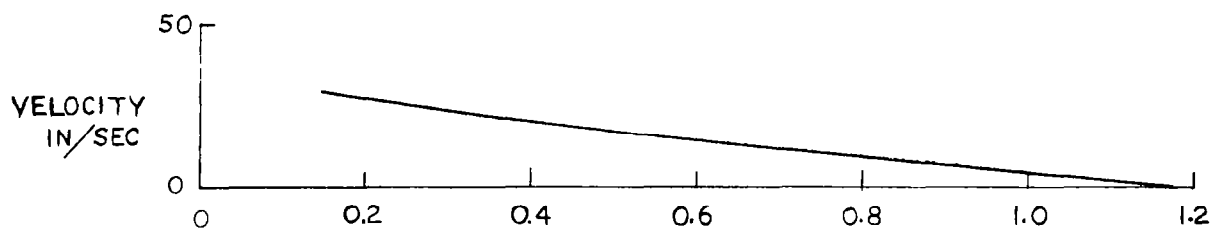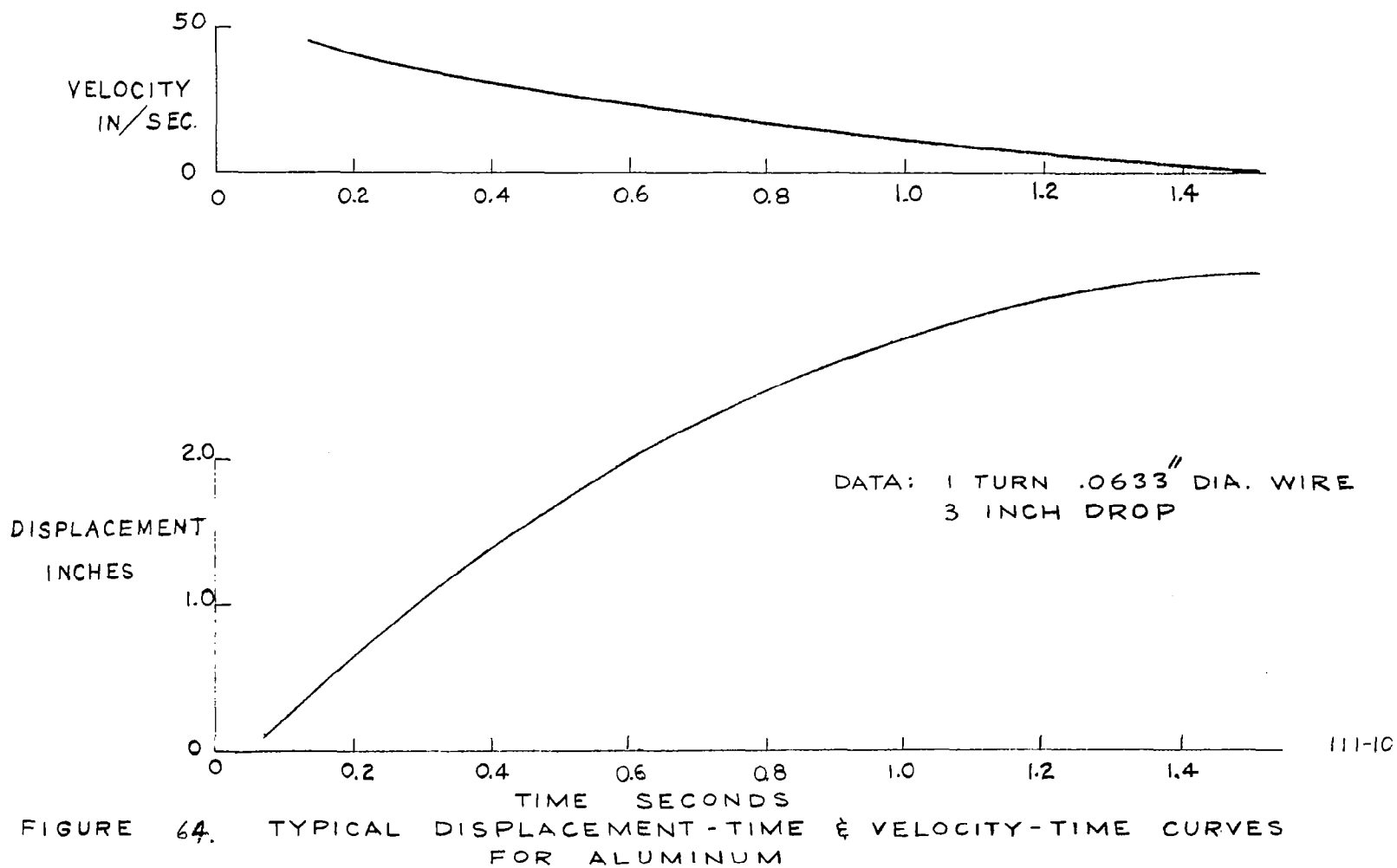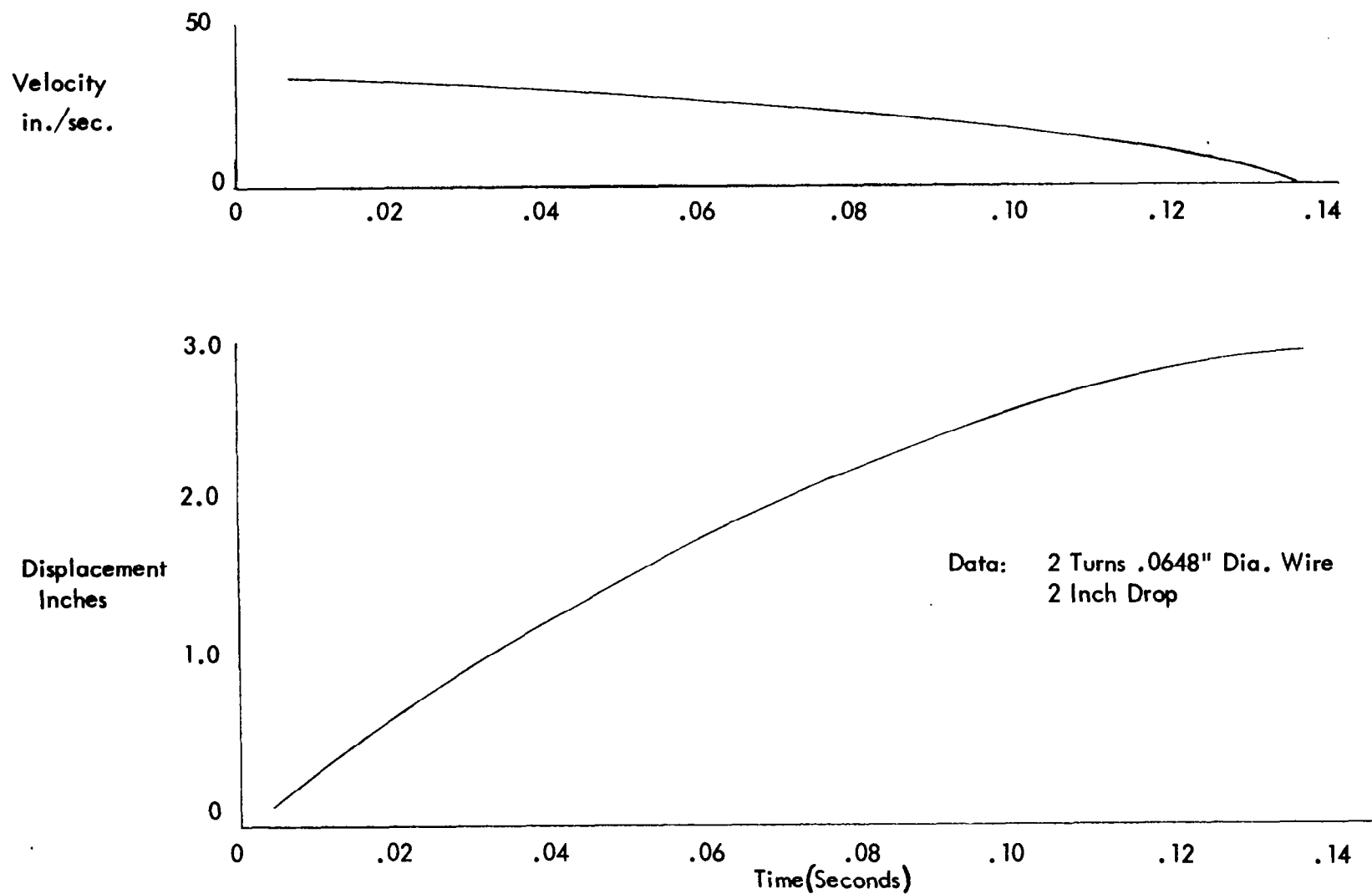
Figure 65.   Typical Displacement – Time & Velocity – Time Curves for Nylon

N-151

Figure 66. <u>Typical Displacement – Time & Velocity – Time</u>
<u>Curves for Nylon Element</u>

Data: 2 Turns .0678" Dia. Wire
        3 Inch Drop
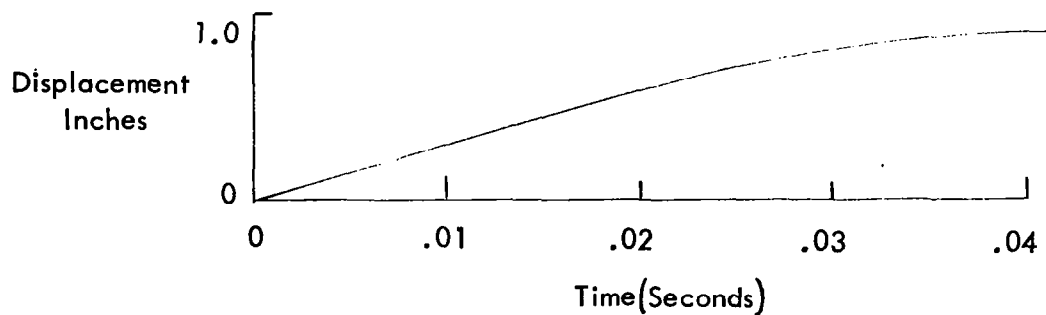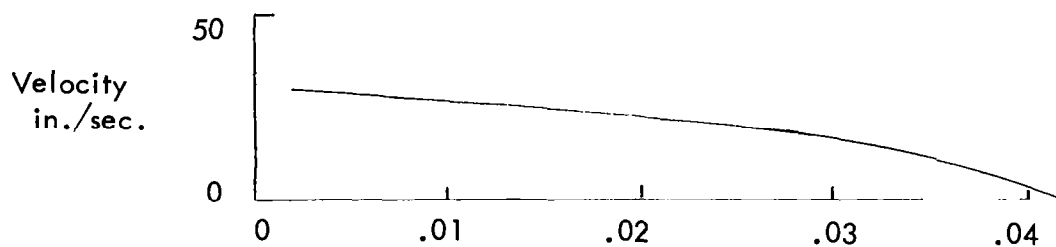
N-152

TABLE 4

Summary of Quasi-Static and Drop Results for Device with Single 0.0632 inch Diameter Aluminum Element

Quasi-Static Results

Type of Measurement	No. of Measurements	Force (lb)		
		High	Low	Average
Tension	5	90.5	73.7	83.9
Compression	8	110.4	79.9	96.4
Tension & Compression	13	110.4	73.7	91.6

Drop Results

Drop Height (in.)	No. of Drops	Force (lb)		
		High	Low	Average
1	3	131	106	117
2	1	-	-	116
3	4	132	113	120
4	1	-	-	115

TABLE 5

Summary of Quasi-Static Results for
Device with Nylon Elements

Wire Diam. (inches)	No. of Turns	No. of Measurements	High	Force per turn (lb)	
				Low	Average
.0634	2	21	14.1	10.6	12.7
.0635	1	10	16.6	10.89	14.8
.0640	2	2	20.6	19.4	20.0
.0648	2	8	32.6	22.8	27.8
.0650	2	4	35.4	28.0	31.8
.0660	2	5	59.8	53.9	56.3
.0670	2	4	71.2	63.0	67.9
.0680	2	4	96.2	88.0	92.3
.0690	2	4	158	101	130.4

All of the drop results are presented in terms of an average force computed from the values of drop height, stroke length, and weight.

Indications of the (gross) variations in force with stroke or time are shown in Figures 63 to 66. These figures show typical stroke-time and velocity-time curves computed from the photographic records. Deviations from linear relations in the velocity-time curves indicate variations in force. These results do not indicate local fluctuations as shown in the quasi-static results of Figure 58, but represent variations in the average force-time behavior.

4.   Discussion of Results

Several features of interest are immediately apparent from the foregoing experimental results:

(i)   The forces for both the aluminum and the nylon working elements are substantially underestimated by consideration of only longitudinal deformation produced from rolling of the torus elements. The design forces previously computed on this basis from the cyclic torsion data are 49 and 8.8 lb per loop of aluminum and nylon, respectively. These forces may be compared with measured quasi-static values ranging from 74 to 110 lb for the 0.0632-inch aluminum element and 11 to 14 lb for the smallest (0.0634-inch) nylon element.

(ii)   Considerable variation exists in the measured forces for elements of equal diameter or, for the same element, under similar testing conditions.

(iii)   The aluminum elements would roll for only a very narrow range of diametral interferences (on the order of 0.001 inch).

(iv)   The nylon elements show a considerable increase in

128

force with increases in wire diameter or interference.

(v)   The aluminum elements exhibit cyclic rate sensitivities comparable to those for unidirectional straining over the frequency range investigated. (Rate sensitivities computed from the differences between the quasi-static and the drop measurements are on the order of 0.04).

(vi)   The nylon elements exhibit almost negligible rate sensitivities over the frequency range investigated.

Items (i) to (iv) above can all be explained in terms of the complex mode of deformation resulting from lateral compression of the torus elements, coupled with variations in interference due to local variations in element and tube dimensions. This complex mode of deformation gives rise to much greater hysteresis than that predicted from longitudinal deformation alone.

The effect of lateral compression of the nylon elements based on the previous viscoelastic analysis is illustrated in Figure 56, which may be compared with the experimental curve of Figure 62. The values of G_2 required to match the theoretical results with the experimental curve range from 17,000 psi for the 0.064 inch element to 5,330 psi for the 0.069 inch element. These values are considerably below those of Table 2, which range from 39,400 to 78,200 psi. Although the results demonstrate the considerable hysteresis effect resulting from the lateral compressive mode of deformation, the appreciable discrepancy between theory and experiment cannot be explained. There is a strain amplitude effect on G_2 which, of course, was not accounted for in the linear viscoelastic analysis. However, there do not appear to be sufficient differences in the strain amplitudes of Table 2 and those occurring from the lateral compression to

explain the discrepancies. Moreover, the changes in G_2 with increasing strain seem to be in the wrong directions. Furthermore, although the theoretical model required some approximations, it is not felt that the errors are as great as indicated by the present discrepancies. Rather, it is believed that the cyclic torsion data and, in particular, the phase lag measurements could be in error.

The lateral compressive effect could be even more pronounced in the case of aluminum, due to the low strain-hardening of the stress-strain curve and the appreciable strain concentrations likely to result at the points of contact. Thus, the narrow range of interferences for which the aluminum elements would roll, as well as the variations in the measured forces, are likely due to the sensitivity of this lateral deformation to changes in interference. For the particular test device, the minimum interference and lateral force required for adequate friction drive were apparently just sufficient to overcome the resulting complex hysteresis. As the interference was increased, the lateral deformation and the hysteresis apparently increased more rapidly than the lateral compressive force, and hence the friction drive became inadequate. Rolling of the nylon elements for the larger interferences can probably be attributed to lower strain-hardening and smaller strain concentrations, and hence a lower rate of increase in hysteresis with interference.

Rate sensitivities for the aluminum were computed from the quasi-static results (0.086 cps) and the drop-test results using Equation (25). Average frequencies during the drop tests ranged from 35 cps for the 1-inch drops to 70 cps for the 4-inch drop. Values of rate sensitivity η (Equation (16)) ranged from 0.036 to 0.042 for the drop data of Table 4. As demonstrated in Section V of this report, room-temperature rate sensitivities

130

of this magnitude should have little effect on load-stroke or deceleration-time behavior of impact devices for normal applications. This is further demonstrated by the velocity-time curves of Figures 63 and 64. The slight deviations from linear behavior indicate small variations in the resisting forces.

The almost negligible rate sensitivity of the nylon in this frequency range is apparent from Figures 61 and 62. It is interesting that a slight increase in force with decrease in frequency is suggested by the drop data at the lower frequency range. This is indicated in Figure 61 in the neighborhood of the 1/2-inch and 1 – inch drops, and is further suggested by the shapes of the velocity-time curves of Figures 65 and 66. In these latter curves the deceleration appears to increase toward the latter part of the stroke. However, the data is currently too limited to draw any firm conclusions.

C.   Rolling Tube Device

Tests were performed to demonstrate the feasibility of the rolling tube device and to check the validity of the previous analysis. A test device was fabricated as shown in the sketch of Figure 67 and the photograph of Figure 68. The tubes are 0.25 inch OD, 0.006 inch wall, annealed 304 Stainless Steel, and 0.25 inch plates were used for rigidity.

Performance curves were determined for the working tubes, based on the results of Figure 21. These are shown in Figures 69 and 70.

Two types of tests were performed. Lateral compressive load-deflection behavior was determined by dead-weight loading of single tubes. Results were determined for a virgin tube, and for tubes plastically deformed after operation in the device. These results are shown in Figure 71, along with predicted values from Figures 69 and 70.

131

Center Driving Plate

Outer Pressure Plates

Spacers

Working Element Tubes

Adjusting Bolts
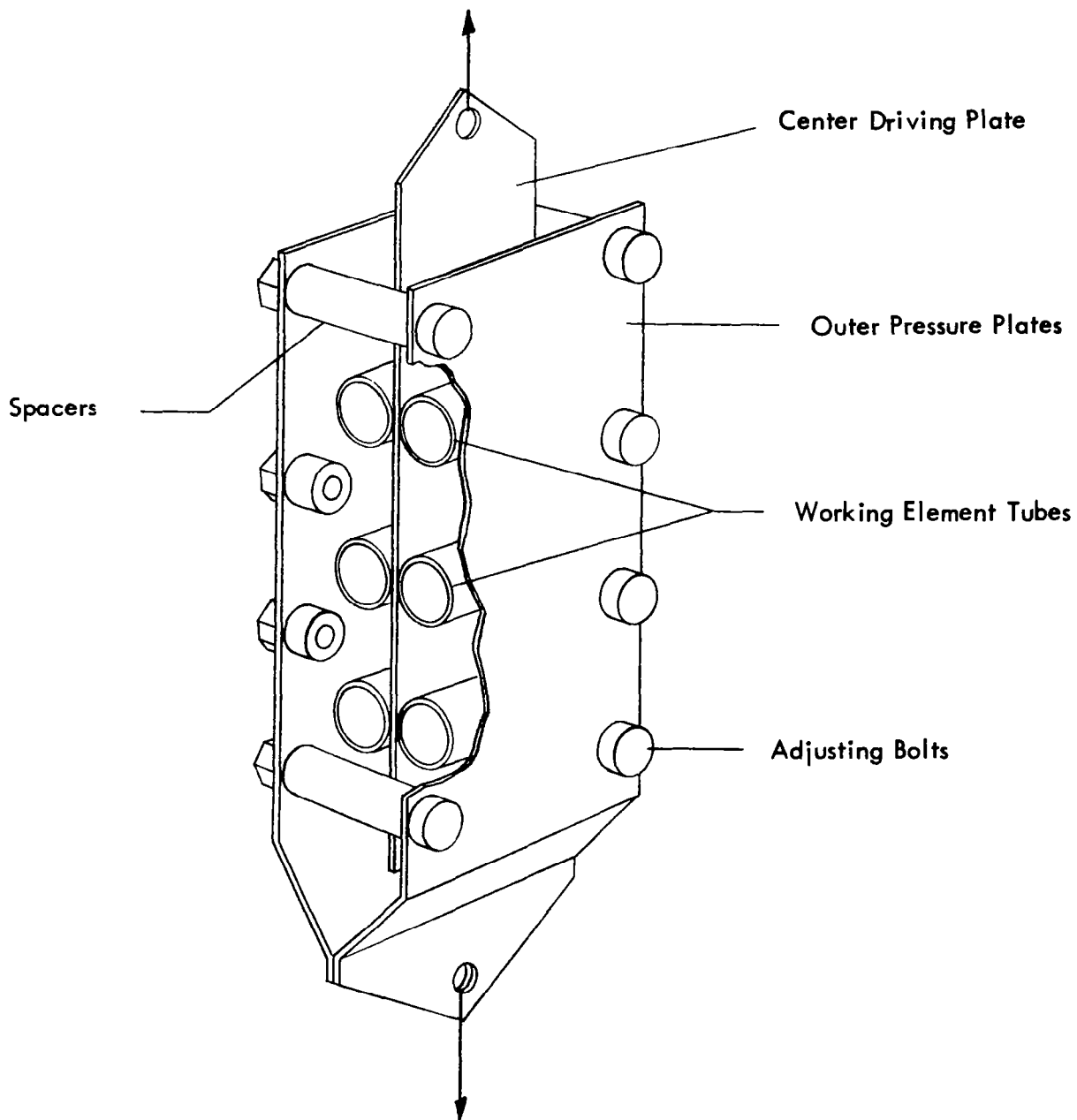
Figure 67. Laboratory Rolling Tube Device

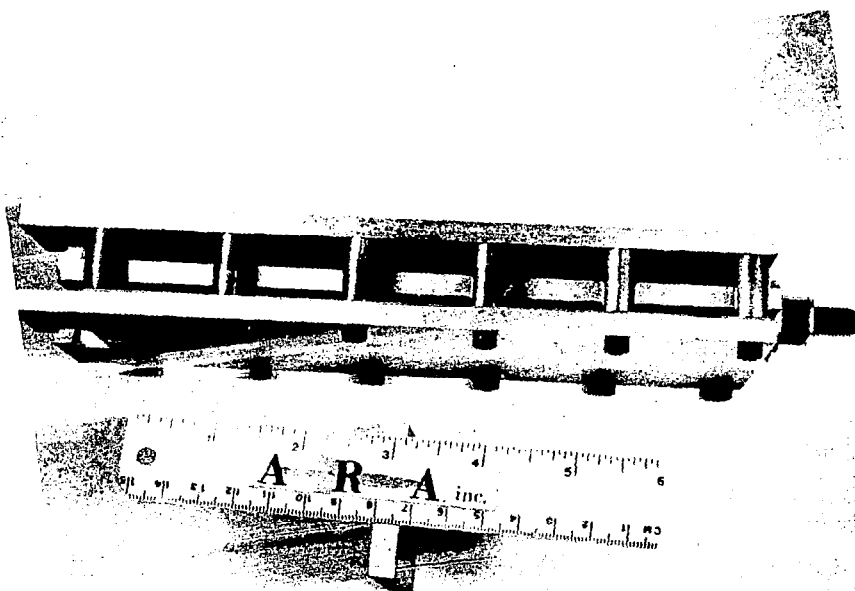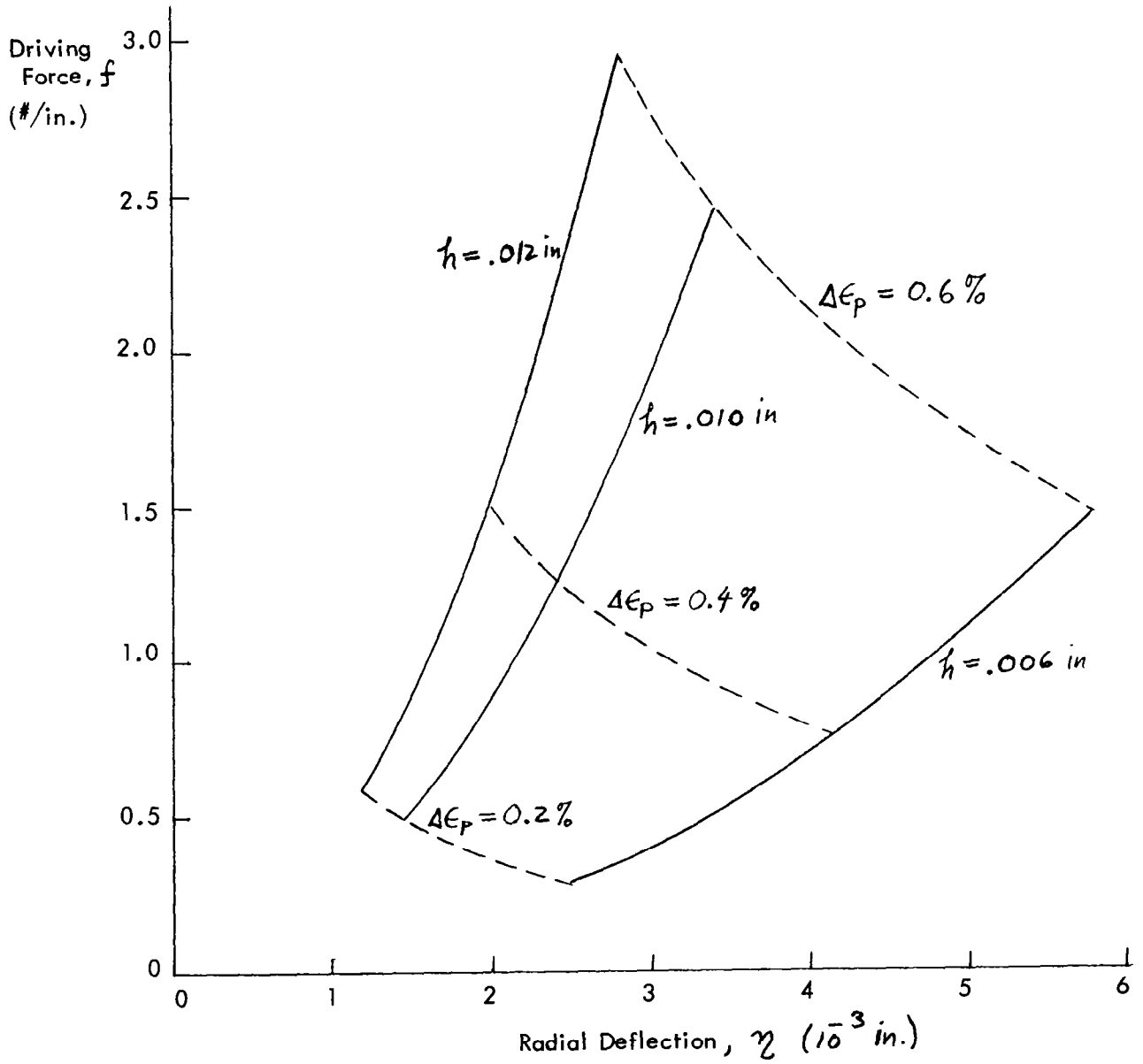Figure 68.   Laboratory Rolling Tube Device

Figure 69.   Driving Force – Lateral Deflection Curves for 0.25 inch OD
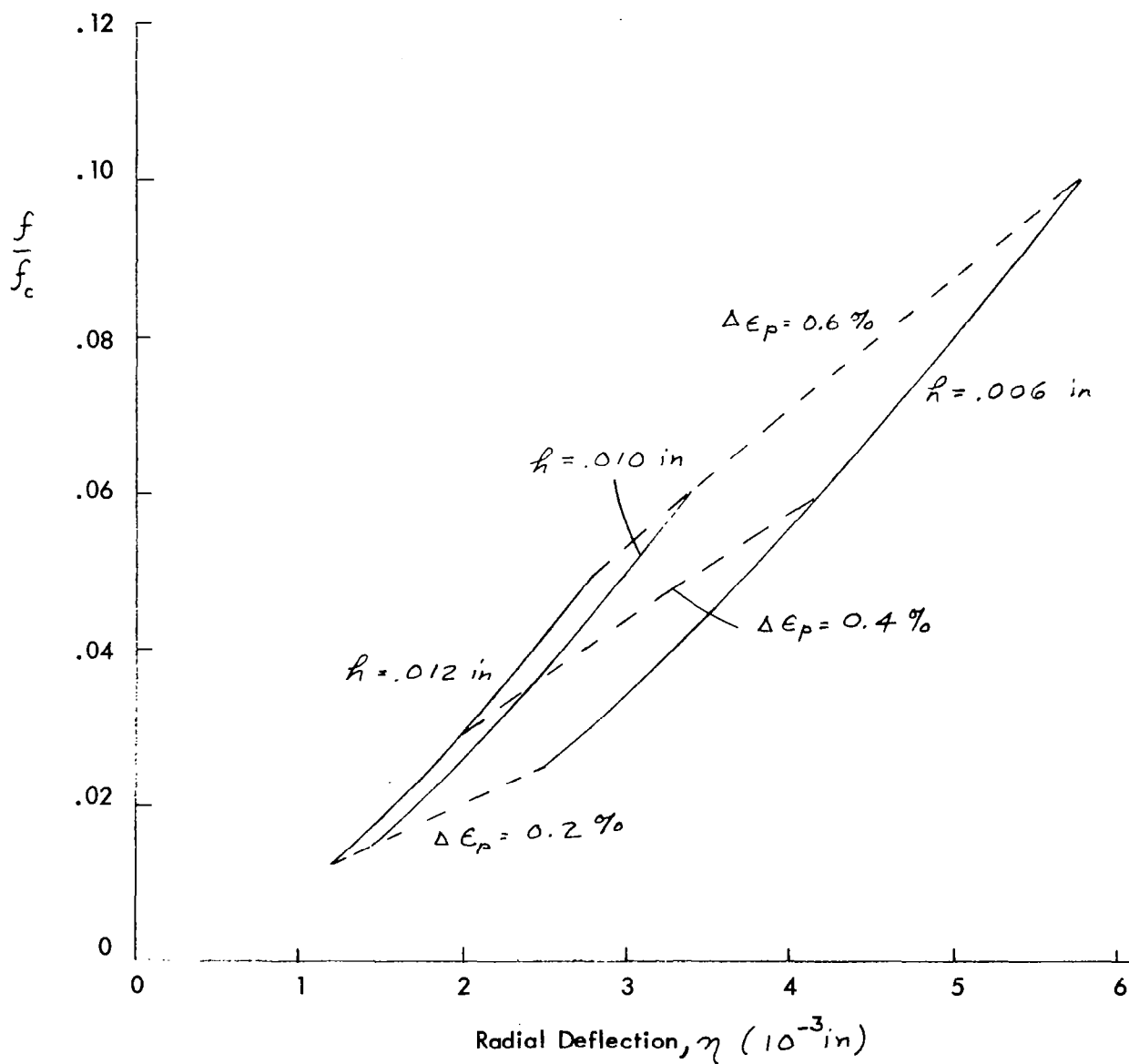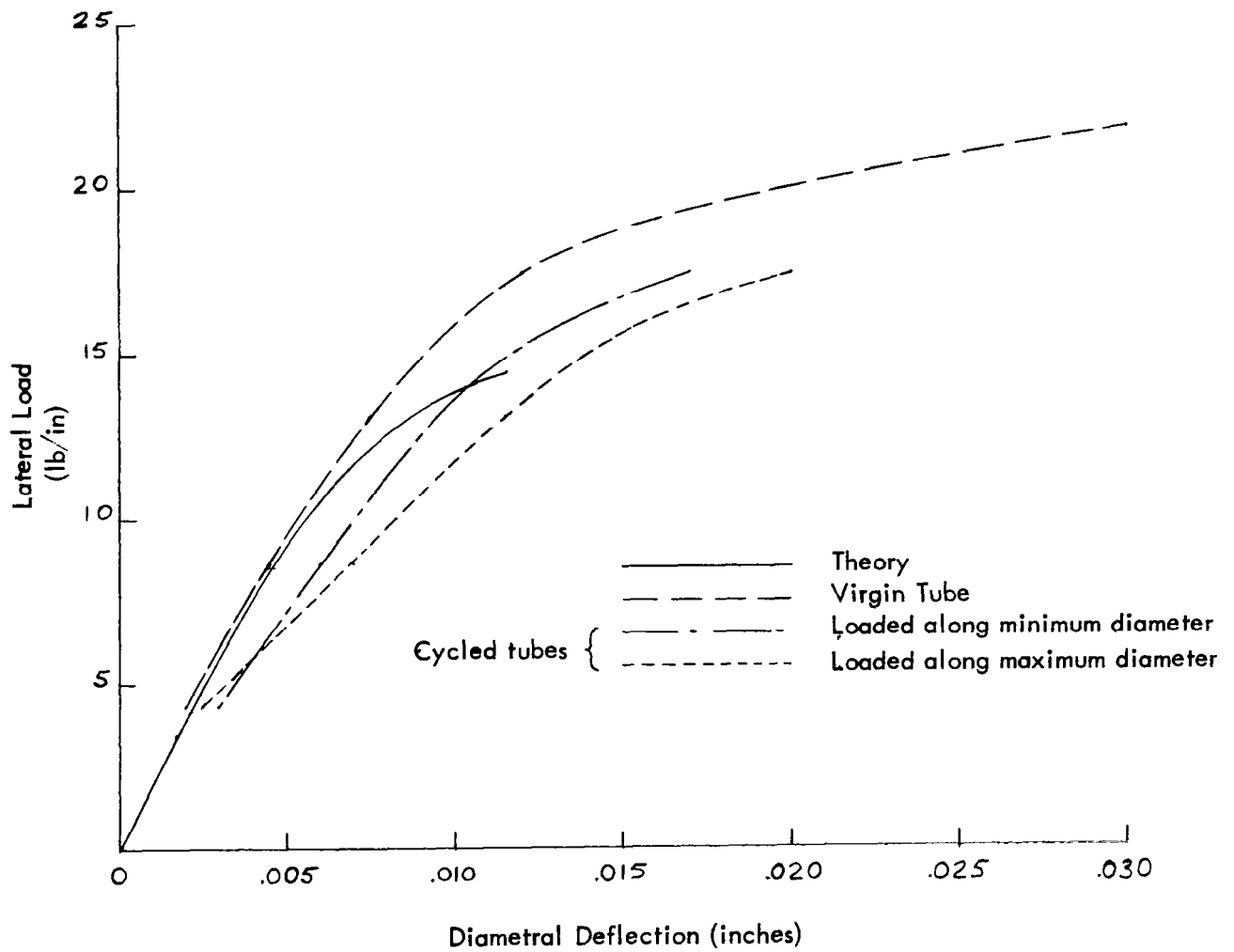302 Stainless Steel Tube

Figure 70.   Driving Force – Compressive Force Ratio vs Lateral
Deflection for 0.25 inch OD 302 stainless Steel Tube

Figure 71. Lateral Load-Deflection Curves for Single Tubes

Theory
Virgin Tube
Cycled tubes { Loaded along minimum diameter
Loaded along maximum diameter

Driving force vs lateral deflection was determined by loading the test device in a Dillon tester. These results are shown in Figure 72, along with the predicted values.

The lateral load-deflection results are in fair agreement with the theoretical values. The considerable scatter in the three test cases apparently is due to differences in geometry as well as changes in flow behavior from cycling. The cycled tubes were loaded in directions of maximum and minimum diameters. The major source of error in the calculated values is expected to be due to incorrect moment-curvature and stress-strain data used in the analysis.

Appreciable disagreement is apparent between the theoretical and experimental driving force vs lateral deflection curves. This error is attributed primarily to incorrect stress-strain values used in the analysis. The errors in the predicted lateral load-deflection curve are much less than those of the driving force curve. This indicates that the moment-curvature data used in the bending analysis was fairly accurate compared with the hysteresis behavior computed from the stress-strain curve. The particular stress-strain curve employed was determined from the results of a bend test on 0.012 inch sheet material, in conjunction with the results of a plastic bending analysis. Moreover, the unidirectional rather than the cyclic stress-strain curve was employed, which could introduce significant error. Insufficient data was available to account for cyclic strain-hardening.

A small error in the stress-strain curve could result in considerable error in the hysteresis loops, particularly at the lower strain ranges. If the stress-strain behavior is largely elastic the size of the hysteresis loop represents a small difference between

Figure 72. Driving Force vs Lateral Deflection
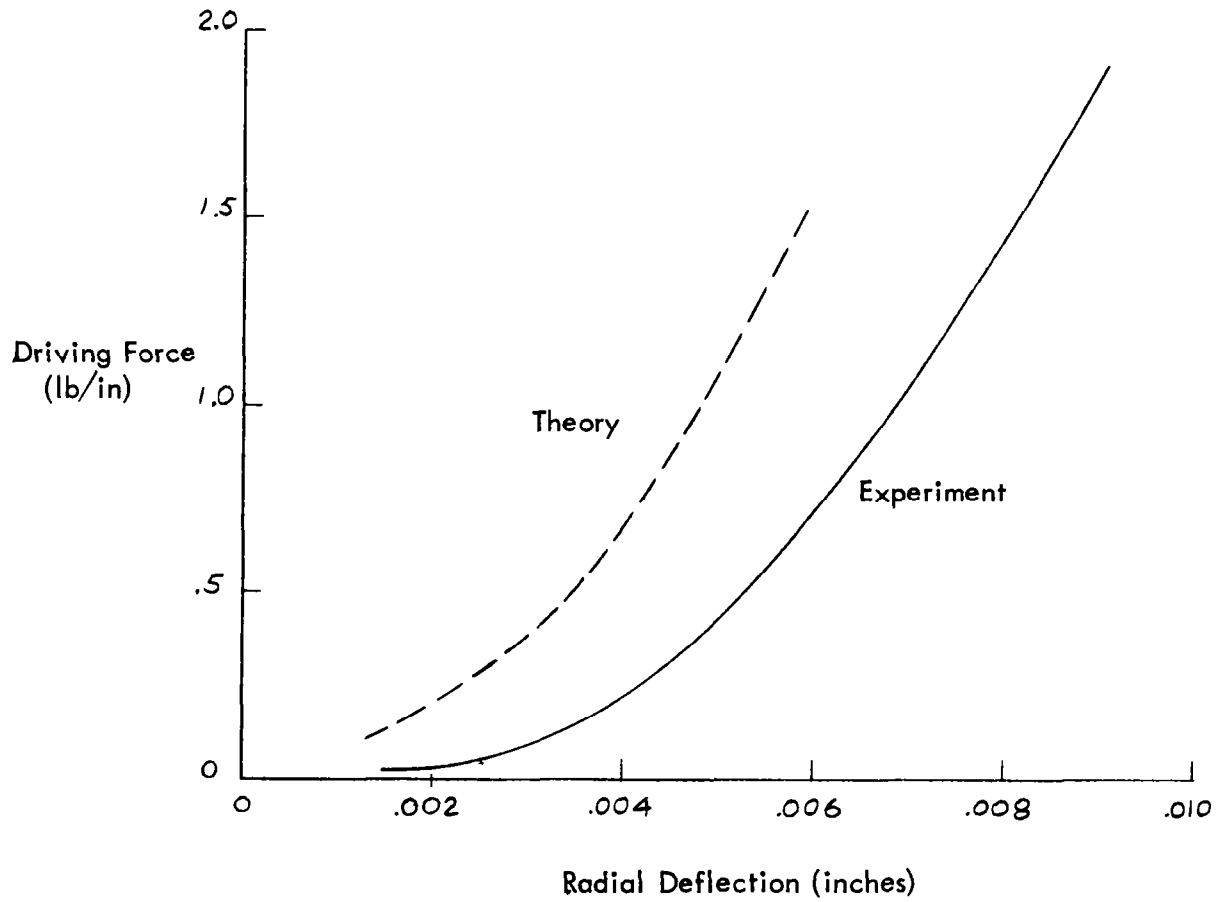
large numbers, so that errors are amplified. This trend is apparent in the curves of Figure 72.

In order to properly evaluate the previous analysis, it would be desirable to employ the results of cyclic bend tests carried out on appropriate sheet material, as well as basic cyclic stress-strain data. An additional check on the stress-strain data and bending theory could be afforded by applying the data to the prediction of the cyclic bending hysteresis behavior.

VII   CONCLUDING REMARKS

Basic concepts and principles of cyclic strain energy devices have been described, and flow and fatigue behavior of materials in relation to these devices has been summarized. Performance capabilities and limitations of cyclic strain energy impact devices have been established for single and multiple-impact applications, based on certain material properties and fundamental design considerations. Analytical methods for predicting the behavior of these devices have been developed, and specific applications to two promising devices have been shown.

An experimental investigation has been conducted which has included a study of materials under rapid cyclic torsion as well as the testing of the "torus" and 'rolling tube' cyclic strain energy devices. Basic cyclic flow and fatigue data has been generated which has confirmed pertinent energy absorption parameters under conditions of rapid cyclic straining. Tests with the torus and rolling tube devices have demonstrated their feasibility and have disclosed certain problem areas related to the construction, performance, and analysis of such devices. Although no attempt was made to optimize the particular laboratory devices tested, the results appear to substantiate that cyclic strain energy

impact devices can be developed which offer enormous SEA efficiencies, capability of multiple use in tension and compression, as well as precise and prescribed load-stroke curves. It also appears that, with appropriate data on material behavior, it should be possible to accurately predict the behavior of these devices.

The results of the cyclic torsion tests with metals as well as the tests with the torus device utilizing 1100-type aluminum elements have shown that both flow and fatigue behavior under rapid cyclic straining conditions can be approximated by low frequency data. Also, rate sensitivity for 1100 aluminum and 347 stainless steel under cyclic straining is the same order of magnitude as for unidirectional straining. Temperature rise with metals can have a significant effect on load-stroke behavior although this will become important only for very high specific energy absorption requiring large strain ranges and few operating cycles. Fatigue behavior for the metals tested in cyclic torsion correlates reasonably well with uniaxial results, using the maximum shear criterion.

The cyclic torsion apparatus proved adequate for studying metals at the high strain ranges and frequencies of interest, although difficulties were encountered with the nylon because phase lag could not be determined with sufficient accuracy. This presented no serious problem with the metals since the elastic strain range can be computed from stress range and elastic modulus. However, the hysteresis behavior of the nylon is dependent directly on phase lag.

There appears to be a descrepancy in the nylon data even at the lower frequencies, based on the results of the torus tests, the cyclic torsion tests, and the analysis of the torus device. It would be of interest to check the viscoelastic analysis of the compressed rolling rod with tests on straight rods of known viscoelastic properties. If successful, this type of test could provide an alternate means for determining loss modulus in nonmetallic

materials under large strain ranges. It would also be instructive to carry such tests to fatigue failure and correlate the results with basic strain fatigue data.

The fatigue data obtained for the nylon, although limited, indicates a much greater sensitivity to strain range than for typical ductile metals. Much more testing at a variety of strain ranges, frequencies, and temperatures is required before low cycle fatigue relations for nonmetals can be obtained analogus to those for metals.

Further cyclic testing of nylon is required to establish the effects of strain range, frequency, temperature, and history on cyclic stress-strain behavior. From the limited test results there appear to be significant history effects and rather severe temperature sensitivity. This could make nylon much less attractive than metals in cyclic strain energy devices requiring precise and repeatable load-stroke curves, particularly under adverse environmental conditions. However, the test data was too limited to be conclusive, particularly from the standpoint of the temperature measurements.

It is interesting that the torus device utilizing nylon working elements exhibited very low rate sensitivity. This could be due to compensating effects of rate on stress range and phase lag with little change in hysteresis.

The analytical and experimental results with the rolling tube device indicate that such a device can be constructed to provide rather precise as well as easily adjusted load-stroke behavior. Further applications of the analytical method with more adequate stress-strain data would be of interest. For this purpose it would be useful to obtain cyclic bending data for thin sheet material, as well as cyclic tension-compression data. It would also be instructive to test such devices to failure in order to correlate fatigue life with predictions of maximum strain range, using established low cycle fatigue relations.

The problem of lateral compressive deformation of metallic elements in friction torus devices warrants further study. It would be of interest to determine the effects of compressive force, diametral interference, surface conditions, etc., on both the load-stroke and fatigue behavior of these devices.

Investigations of cyclic strain energy devices are being continued at ARA, Inc. under two NASA contracts. Although these studies are being directed toward particular applications of energy absorbing systems, the investigations cover some of the basic problem areas enumerated above.

REFERENCES

1. Platus, D. L. and F. A. Marovich, An Invention of Multiple-Impact High Energy Absorbing Devices Utilizing Cyclic Deformation of Metals, ARA Report #9, 18 December 1962.

2. Platus, D. L., A Reduction to Practice of a Multiple-Impact High Energy Absorbing Device Utilizing Cyclic Deformation of a Metal, ARA Report #16, 30 March 1963.

3. Esgar, J. B., Survey of Energy Absorption Devices for Soft Landing of Space Vehicles, NASA TN D-1308, June 1962.

4. Mc Gehee, J. R., A Preliminary Experimental Investigation of an Energy-Absorption Process Employing Frangible Metal Tubing, NASA TN D-1477, October 1962.

5. Whittier, J. S., Rheological Properties of Adhesives Considered for Interface Damping, WADD Technical Report 60-280, June 1960.

6. Tavernelli, J. F. and L. F. Coffin, Jr., "A Compilation and Interpretation of Cyclic Strain Fatigue Tests on Metals," Transactions, American Society for Metals, Vol. 51, 1959, pp. 438-453.

7. "Materials Selector Issue," Materials in Design Engineering, Mid-October, 1962.

8. S. I. Liu, G. Sachs, J. J. Lynch, and E. J. Ripling, "Low Cycle Fatigue of the Aluminum Alloy 24 ST in Direct Stress," Trans. AIME, Vol. 175 (1948B), p. 469.

9. D. S. Dugsdale, "Stress-Strain Cycles of Large Amplitude," Journal of the Mechanics and Physics of Solids, Vol. 7, 1959, pp. 135-142.

10. A. Johansson, "Fatigue of Steels at Constant Strain Amplitude and Elevated Temperatures," Proceedings, Colloqium on Fatigue, Stockholm, 1955.

11. R. W. Bailey, "Usefulness and Role of Repeated Strain Testing as an Aid to Engineering Design and Practice," International Conference on Fatigue of Metals, 1956.

12. L. F. Coffin, Jr., "A Study of the Effects of Cyclic Thermal Stresses in Ductile Metals," Transactions, ASME, Vol. 76, 1954, pp. 931-950.

REFERENCES (Cont'd)

13. Coffin, L. F. Jr. and J. F. Tavernelli, "The Cyclic Straining and Fatigue of Metals," Transactions of the Metallurgical Society of AIME, Vol. 215, October 1959, pp. 794-806.

14. Polakowski, N. H. and A. Palchoudhuri, "Softening of Certain Cold-Worked Metals Under the Action of Fatigue Loads," Am. Soc. for Testing Materials Proc., Vol 54, 1954, pp. 701-716.

15. Broom, T. and R. K. Ham, "The Hardening and Softening of Metals by Cyclic Stressing," Royal Soc. Proc., Series A, No. 1229, Oct. 1957.

16. Smith, R. W. et al., "Fatigue Behavior of Materials Under Strain Cycling in Low and Intermediate Life Range," NASA TN D-1574, April 1963.

17. Lubahn, J. D. and R. P. Felgar, Plasticity and Creep of Metals, John Wiley & Sons, Inc., New York, 1961.

18. Pierce, B. O. and R. M. Foster, A Short Table of Integrals, Fourth Edition, Ginn and Company, Boston, 1956.

19. Manson, S. S., "Behavior of Materials Under Conditions of Thermal Stress," NACA Rep. 1170, 1954. (Supersedes NACA TN 2933, 1953).

20. E. H. Nickell and W. E. Jacobsen, Factor of Safety Considerations for Aerodynamically Heated Structures Subjected to High Cyclic Stresses, ASD-TR-61-508, October 1961.

21. Swindeman, P. W. and D. A. Douglas, "Failure of Structural Metals Subjected to Strain-Cycling Conditions," ASME, Trans., Series D, Vol. 81, June 1959, pp. 203 - 212.

22. Tobolsky, A. V., Properties and Structures of Polymers, John Wiley & Sons, Inc., New York, 1960.

23. Kawaguchi, T., "The Dynamic Mechanical Properties of Nylons," Journ. of Applied Polymer Sci.", Vol II, No. 4, pp. 56-61, 1959.

24. Woodward, A. E. et al, "Investigations of the Dynamic Mechanical Properties of Some Polyamides," Journ. of Polymer Sci., Vol XLIV, pp. 23-34, 1960.

25. Mason, P., "The Viscoelastic Behavior of Rubber in Extension," Journ. of Applied Polymer Sci., Vol, 1, No. 1, pp. 63-69, 1959.

26. Payne, A. R., "The Dynamic Properties of Carbon Black-Loaded Natural Rubber Vulcanizates, Part I," Journ. of Applied Polymer Sci., Vol VI, No. 19 pp. 57-63, 1962.

REFERENCES (Cont'd)

27. Maxwell, B. and C. Guimon, "Dynamic Mechanical Spectra and Limit of Linear Viscoelasticity of High Polymers," *Journ. of Applied Polymer Sci.*, Vol. VI, No. 19, pp. 83-93, 1962.

28. Kurath, S. F., et al, "The Dynamic Mechanical Properties of Hypalon-20 Synthetic Rubber at Small Strains," *Journ. of Applied Polymer Sci.*," Vol. 1, No. 2,pp. 150-157, 1959.

29. Ungar, E. E. and D. K. Hatch, "High-Damping Materials," *Product Engineering*, April 17, 1961.

30. Alleghany Ludlum Steel Corporation, *Stainless Steel Handbook*, Pittsburgh, Pennsylvania, 1951.

31. ARA, Inc. "Research on Energy Absorbing Structures, Part I – Final Report," AFOSR Contract No. AF 49(638)-1144, February 1963.

32. ARA, Inc. "Research on Energy Absorbing Structures, Part II – Final Report," AFOSR Final Scientific Report 64-0154, AF 49(638)-1144, February 1964, Section IV.

33. Alfrey, T., *Mechanical Behavior of High Polymers*, Interscience Publishers, Inc., New York, 1948, pp. 560-562.

34. Roark, R. J., *Formulas for Stress and Strain*, McGraw-Hill, New York, Third Ed., 1954, p. 288

35. Timoshenko, S and J. N. Goodier, *Theory of Elasticity*, 2nd Ed., McGraw-Hill, New York, 1951, pp. 91-95.